ASTROPARTICLE PHYSICS
with
ARGO

July 23, 1996

The ARGO Collaboration

M.Abbrescia, S.Natali, F.Romano
INFN and Dipartimento di Fisica dell'Università di Bari

Kuang Haohuai, Tan Youheng, Meng Le, Jiang Yinlin, Xu Chunxian, He Huilin, He Huihai, Chen Yongzhong, Lee Huidong, Shen Peiruo
IHEP ,Beijing, China

Yu Guangce, Jia Huanyu, Feng Zhenyong
SWJU, Chengdu, China

M.Storini and G. Villoresi
Istituto di Fisica dello Spazio Interplanetrario del CNR, Frascati, Italy

Li Jinyu, Zhang Xueyao, Zhao Xin, Fu Yu
Shangdong Univ.,Jinan, China

Dai Benzhong
Yunnan University, Kunming, Chine

P. Bernardini, F. Cesaroni, P. Creti, G. Mancarella, D. Martello, M. Panareo, P. Pistilli , A. Surdo
INFN and Dipartimento di Fisica dell'Università di Lecce

Guo Hongwei, Cai Dong, Danzengluobu
Tibet University, Lhasa, China

F. Barone, B. Bartoli, E. Calloni, S. Catalanotti, B. D'Ettorre Piazzoli, G. Di Sciascio, A. Grado, M. Iacovacci, C. Marmolino, L. Milano, M. Oliviero
INFN and Dipartimento di Fisica dell'Università di Napoli, Italy

G.Severino
Osservatorio Astronomico di Capodimonte, Napoli, Italy

R. Cardarelli, A. Cavaliere, A. Morselli, P. Padovani, R. Santonico, R. Sparvoli
INFN and Dipartimento di Fisica dell'Università "Tor Vergata" di Roma , Italy

C. Bacci, M. De Vincenzi, N. Iucci, S. Mari, M. Parisi
INFN and Dipartimento di Fisica dell'Università di Roma Tre

C. Stanescu
INFN Sezione ISS Roma

O. Saavedra, S. Vernetto
Istituto di Cosmogeofisica del CNR and INFN, Torino

Contents

1 THE PHYSICS GOALS **4**

1.1 HIGH ENERGY GAMMA RAY ASTRONOMY 4

1.1.1 Introduction 4

1.1.2 Galactic Sources 6

1.1.3 Pulsars: Pulsed emission 6

1.1.4 Pulsar : Unpulsed emission 10

1.1.5 Supernova Remnants 14

1.1.6 Molecular Clouds 15

1.1.7 Diffuse photons along the Galactic plane 20

1.1.8 Extragalactic Sources 23

1.2 GAMMA RAY BURSTS 29

1.3 ANTIPROTON FLUX AT $\sim 1\,TeV$ ENERGY 32

1.4 THE PRIMARY PROTON SPECTRUM BELOW THE 'KNEE' 36

1.5 SUN AND HELIOSPHERE PHYSICS 38

2 THE EXPERIMENTAL SETUP AND ITS PERFORMANCES **48**

2.1 THE RPC SYSTEM 48

2.2 DETECTOR PERFORMANCES 50

2.2.1 Photon primaries 51

2.2.2 Proton primaries 62

2.2.3 γ/p Discrimination 62

2.3 ARGO SENSITIVITY AND PHYSICS PERFORMANCES 66

2.4 GAMMA RAY BURSTS 81

2.5 MEASUREMENT OF THE $\overline{p}/p$ RATIO ABOUT 1 TeV 87

2.6 THE PROTON SPECTRUM IN THE ENERGY RANGE $10 \div 200\,TeV$ . . 94

2.7 SOLAR AND HELIOSPHERE PHYSICS 95

2.7.1 Cosmic Ray Modulations 95

2.7.2 Solar Flares 99

2.7.3 The Monitoring of the IMF 100

3 THE DETECTOR **107**

3.1 INTRODUCTION 107

3.2 DETECTOR LAY–OUT 108

3.3 GAS SYSTEM 112

3.4 HIGH VOLTAGE SYSTEM 114

3.5 THE DAQ SYSTEM 116

3.5.1 Front End Electronics 116

3.5.2 Trigger System and station interconnections. 117

3.5.3 Connection between Trigger and Event Builder 120

3.6 EVENT BUILDER AND STORAGE SYSTEM 120

3.6.1 Specifications 120

3.6.2 Architecture 121

3.7 THE RPC TEST ARRAY 123

3.7.1 Temperature and Pressure Tests 123

3.8 THE SITE AND LOGISTIC. 133

THE ARGO DETECTOR

AND

ITS PHYSICS GOALS

ARGO is a telescope optimized for the detection of small size air showers. The design of the detector is very simple: it consists of a single layer ($\sim 95\%$ of active area) of RPC's (Resistive Plate Counters) covering an area $\sim 10^4\ m^2$ and providing a detailed space-time picture of the shower front. RPC's have been employed successfully both in cosmic ray and accelerator experiments and their extensive use is envisaged for future experiments at SLAC and LHC. Performances, low cost and the opportunity of assembling in a close structure make this device a very attractive alternative to the traditional scintillation counters.

Once operated at high elevation ($> 4000\,m\,a.s.l.$) ARGO could image with high efficiency and sensitivity atmospheric showers initiated by primaries of energies in the range $10\,GeV \div 500\,TeV$. As a result of the different development in atmosphere of photon and proton induced showers at energies below $1\,TeV$, a discrimination against cosmic rays background events is obtained, making ARGO a powerful detector to study cosmic γ-radiation at an energy threshold not far from the present experimental limits of the satellite technology and covering the unexplored range of energies between 50 and 300 GeV. In addition, due to the good angular and energy resolution in defining cosmic ray beams, ARGO could investigate the effect of the geomagnetic, solar and Interplanetary Magnetic Fields on the propagation of cosmic ray at a $10\,GeV$ threshold, in this way providing full complementarity to satellite programs.

We propose to build this detector at the Yanbajing Cosmic Ray Laboratory (Lhasa, Tibet), 4300 m a.s.l., $30^0\,N$ latitude. The Yanbajing Laboratory offers important advantages provided by its unique natural environment. It is only 90 Km far from Lhasa, connected by an asphalt road, and, due to the shielding provided by the Himalayan mountains, benefits of good weather conditions also during the winter. The Laboratory presently hosts the AS-γ experiment carried out by a Chinese-Japanese collaboration which has been successfully running for 5 years. At this site, ARGO will provide a systematic and continuous monitoring of the Northern Hemisphere in the declination band $-10^0 < \delta < 70^0$. It is worthwhile to point out that ARGO will benefit from geographic location to exploit the Crab "standard-candle" as a reference photon beam continuously 'ON' for developing the experimental techniques appropriate to the GeV-TeV γ-ray astronomy.

It has to be stressed that the high elevation of the site provides very important advantages in various aspects of cosmic ray physics. In fact, in addition to the obvious decrease of the threshold energy, crucial for many issues of gamma–ray physics, several other parameters like shower age size fluctuations, time profile, lateral spread, are such to permit the study of the elemental composition around the knee in a very efficient and reliable way. Moreover, the site offers a good opportunity for operations of Cherenkov telescopes, working either in the optical or in the U.V. range. This site is therefore a natural candidate to become the most important center in the world for cosmic ray physics below $10^{17} eV$.

Data gathered with ARGO will allow to face a wide range of fundamental issues. These include:

1) Gamma–astronomy, at a $\sim 100\, GeV$ threshold energy. More than 300 galactic and extragalactic point candidate sources can be monitored, with a sensitivity to unidentified sources better than 10% of the Crab flux.

2) Diffuse Gamma–Rays from the Galactic plane, molecular clouds and SuperNova Remnants (SNR) at energies $\geq 100\, GeV$ never observed so far.

3) Gamma Ray Burst (GRB) physics, by allowing the extension of the satellite measurements over the full GeV/TeV energy range.

4) $\overline{p}/p$ ratio at energies $300\, GeV \div \sim TeV$ not accessible to satellites, with a sensitivity adequate to distinguish between models of local (galactic) $\overline{p}$ production and models accounting for an extragalactic origin.

5) The primary proton spectrum in the $10 \div 200\, TeV$ region, with sensitivity sufficient to detect a possible change of the slope of the energy spectrum.

6) Sun and Heliosphere physics, including cosmic ray modulations at $10\, GeV$ threshold energy, the continuous monitoring of the large scale structure of the interplanetary magnetic field and high energy gamma and neutron flares from the Sun.

Not included in this list are other physics items which require, in order to define the ARGO sensitivity, dedicated calculations. They are under investigation, and results will be presented separately. We mention, for instance,

a) test of cosmic-ray universality looking at the diffuse photon emission from nearby Galaxies;

b) composition studies at the knee by exploiting the shadow of the Sun in charged cosmic ray.

c) photon emission from dark-matter annihilation in the galactic center or in the galactic halo;

Additional objectives come from using ARGO as a traditional EAS array covering the full energy range from 10^{11} to $10^{16}\, eV$. Since ARGO provides a high granularity space–time picture of the shower front, detailed study of shower properties as, for instance, multicore–events, time distributions of EAS particles, multifractal structure of particle densities near the core, can be performed with unprecedented resolution. At an altitude $> 4000\, m\ a.s.l.$ the electron size of the shower produced by primaries energies $10^{15} \div 10^{16}\, eV$ around the 'knee' of cosmic ray spectrum is practically independent of their mass. This fact could be exploited to get information about the composition at the knee by measuring other parameters distinguishing showers developed by primaries of different mass.

Accurate evaluation of the performances of such a device has been carried out for two different sizes:

- **ARGO-3600**, a $60 \times 60\ m^2$ carpet with the capability of realizing the full physics program at a sensitivity level a factor of 2.3 lower than ARGO full size;
- **ARGO**, a $120 \times 120\ m^2$ carpet.

This document is organized as follows:
In Chapter I we briefly review the physics concerning the main objectives of the experiment, pointing out the motivations for building the detector. In Chapter II a general description of the proposed experiment is given and its performances are presented. Chapter III is devoted to a technical description of the RPC's, read-out electronics, data acquisition and event processing. A description of the experimental site and its environment is included.

Chapter 1

THE PHYSICS GOALS

1.1 HIGH ENERGY GAMMA RAY ASTRONOMY

1.1.1 Introduction

The use of high energy gamma-rays is the final step in the utilization of the whole electromagnetic spectrum for investigating the most energetic processes and phenomena in the Universe. Gamma rays come from a variety of astronomical sources which accelerate charged cosmic rays (supernovae, neutron stars, quasars and the cores of active galaxies). They are not deviated by galactic or extragalactic magnetic fields so that their directions bring the information of the production site. Thus the search for cosmic gamma-rays is primarily addressed
a) to the search for cosmic ray sources;
b) to the investigation of the phenomena in the acceleration sites;
c) to the study of the propagation effects throughout the interstellar or intergalactic medium.

The certainty that a consistent number of sources of HE/VHE γ-rays do exist has been recently reached with the operation of the EGRET experiment [1] on board the Compton Gamma-Ray Observatory (CGRO) covering the $30\,MeV$ to $20\,GeV$ energy region, and of ground based telescopes imaging the Cerenkov light of air showers induced by γ-rays in the $0.4 \div 10\,TeV$ energy range [2].

The present experimental results can be summarized as follows
1) the EGRET source catalogue includes 129 sources, 38 of them being within 10^0 of the galactic plane. Six of the in-plane sources have been firmly identified with pulsars and 32 are unidentified sources. The 91 sources with galactic latitude $|b| > 10^0$ include the Large Magellanic Cloud (LMC), 40 sources identified with active galactic nuclei (AGN) with high confidence, 11 sources which may be AGN, and 39 unidentified sources. For comparison, prior to the launch of CGRO only 3 gamma-ray HE sources (two galactic and one extragalactic) have been identified;
2) two galactic (Crab Nebula and PSR1706-44) and two extragalactic (Mrk 421 and Mrk 501) gamma-ray sources have been observed above $400\,GeV$ by Cerenkov telescopes (Whipple,

Themistocle and Cangaroo).

The combination of HE and VHE observations look very promising for the understanding of the radiation mechanisms. In fact production processes in these regimes are expected to be quite different. GeV photons are essentially produced via synchrotron or curvature radiation and, at a minor extent, via inverse Compton scattering. TeV photons are related both to electromagnetic (inverse Compton scattering) or hadronic processes (photoproduction or proton-gas interaction in which the gamma ray production occurs via π^0 decay) which involve the acceleration of the parent particles (electrons or protons) up to very high energies $\geq 10^{14}\ eV$. Moreover, since for VHE γ-rays the problem of the absorption inside the source becomes severe, the site of production could be different from that where GeV photons are produced. Thus, detection of VHE-gamma may either establish direct evidence for the sources of cosmic rays or provide fundamental information on the nature and geometry of the source and on the acceleration mechanism there operating.

It is worth also to mention a) the diffuse γ-ray emission from the galactic plane primarily by the interaction of cosmic ray protons with the interstellar gas, b) the γ-ray emission from nearby supernova remnants and molecular clouds. This diffuse radiation has been observed so far only at energies $< 10\ GeV$. Its detection at higher energies would provide a good opportunity to study the cosmic ray large scale distribution in the galaxy and identify possible cosmic ray sources and regions of enhanced/depleted cosmic ray density.

These arguments are of particular relevance when considered in the context of the extra-galactic scenario. Many AGNs show emission spectra with no apparent energy cutoff up to $\sim 10 GeV$. AGNs, recognized as a potential class of cosmic ray sources beyond $\sim 10^{17} eV$, may well have emission extending into the VHE region. Thus, it seems natural to expect γ-ray emission beyond the energy domain of EGRET. There is a variety of models for gamma-rays production. Leptonic models, mostly involving inverse Compton scattering of lower energy photons to gamma-ray energies by beamed relativistic electrons, could in principle account for observed spectral properties and variability, but have severe difficulties in explaining the TeV emission observed from Mrk421. On the contrary, in the frame of hadronic models based on the acceleration of a proton beam, the extension of the spectrum up to TeV energies is not a problem. This possibility is doubly attractive, either in relation to the search for the sources of highest energy cosmic rays ($> 10^{17}\ eV$) or because of the obvious implications for the extragalactic neutrino astronomy.

A very interesting feature of extragalactic high energy γ-ray astronomy is the opportunity of establishing the distance scale of AGNs in a manner independent of other techniques. In fact, due to the absorption of high energy γ-rays by pair-production interactions with the intergalactic infrared radiation field, the pure γ-ray power law $E^{-\gamma}$ at source becomes $E^{-\gamma}e^{-\tau}$ at Earth, where the γ-ray opacity τ scales linearly with the distance. According to some authors high red-shift quasars should be much closer than their red-shift distances, these red-shifts being largely intrinsic in origin. Thus, astrophysics accelerators could provide chance for a long baseline photon beam to test alternative views to the Big Bang model. The experimental results concerning both galactic and extragalactic sources are briefly reviewed in the following sections and prospects for the detection of $100\, GeV$ gamma rays are discussed.

1.1.2 Galactic Sources

The γ-ray sky observed by COSB and EGRET at galactic latitudes $|b| < 10^0$ exhibits a considerable fine structure in the distribution of the emissivity, some of which is certainly associated with discrete γ-ray sources (fig.1.1). A significant fraction of the observed emission is presumably of diffused origin, due to the interaction of cosmic ray protons with the interstellar gas, yielding π^0 mesons subsequently decaying into two γ-rays, but a substantial fraction of the observed flux, ranging from 8% to 50% according to different estimates [3], could be attributed to a superposition of unresolved point-like sources. From the experimental point of view, the sources can be seen as a significant excess above the cosmic background with a spatial distribution consistent with the point-spread function of the detector. 38 galactic sources are listed in the second EGRET source catalog [4]. Among them, 6 pulsed GeV γ-ray sources are firmly identified, through their timing signatures, with spin-powered pulsars: Crab, Vela, Geminga, PSR1055-52, PSR1706-44, PSR1951+32. Gamma-ray emission from nearby supernova remnants (SNR) or molecular clouds located away from the Galactic plane has been also observed by EGRET. Six unidentified sources have been recently associated to SNRs [5] and GeV photons have been observed from the Ophiucus and Orion clouds [6].

Up to now all reports of pulsed TeV γ-ray emission from (radio) pulsars have been of marginal significance, so that only upper limits to the flux can be reported. On the contrary, unpulsed TeV emission has been observed from two of the previous sources, Crab and PSR1706-44.

The UHE signals from X ray binaries claimed by many experiments in eighties have not been confirmed. The new detectors like CASA, CYGNUS, EAS-TOP and HEGRA have not yet provided compelling evidence for the existence of steady sources of UHE γ's. Limits on the steady flux much lower than the flux originally claimed are now currently accepted - see fig.1.2 [7].

To date, the question concerning the origin of high energy cosmic rays ($> 10^{14}\ eV$) has not yet been answered.

The HE/VHE results concern a large variety of cases which are discussed separately in the following.

1.1.3 Pulsars: Pulsed emission

Only six of the more than 550 known radiopulsars have been detected so far by EGRET as pulsed γ-ray sources. The general properties of these pulsars are summarized in Table 1.1, where τ is the dynamic age $P/2\dot{P}$. The EGRET results are summarized in Table 1.2, where γ is the exponent of the differential γ-ray energy spectrum. The γ-ray luminosity L_γ is derived from the distance of the pulsar and assuming a beaming factor of $1/4\pi.F_\gamma$ is the measured energy flux above 100 MeV. The efficiency η is estimated from the fraction of rotational energy loss $\dot{E} = I\Omega\dot{\Omega}$ ($I = 10^{45}\ g \cdot cm^2$, moment of inertia, Ω=angular velocity) converted into γ-ray luminosity L_γ. The light curves of these γ-ray pulsars are shown in fig.1.3.Very different properties in terms of energy spectra and light curves are found. Details can be found in ref. [8]. Some general features are visible in the previous tables. All detected

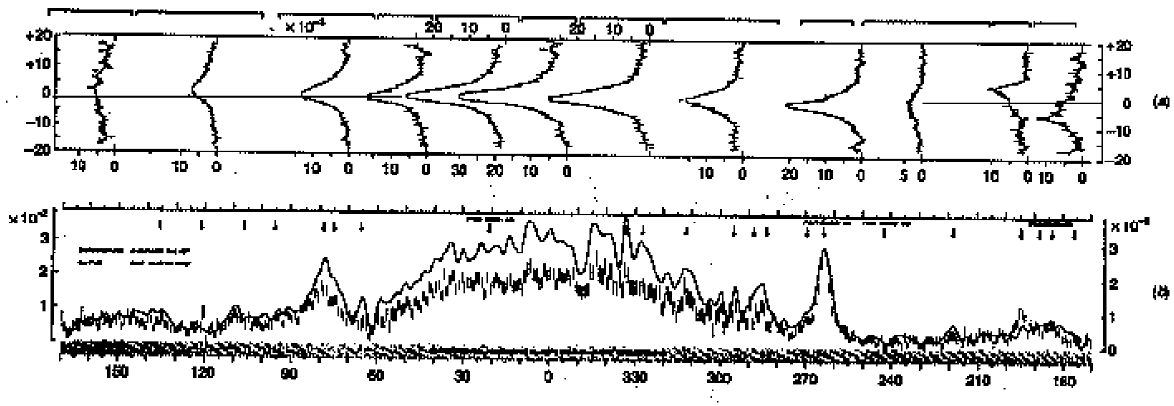

Figure 1.1: The γ–ray galactic plane ($70\,MeV \leq E_{\gamma} \leq 5\,GeV$) as observed by the COSB satellite

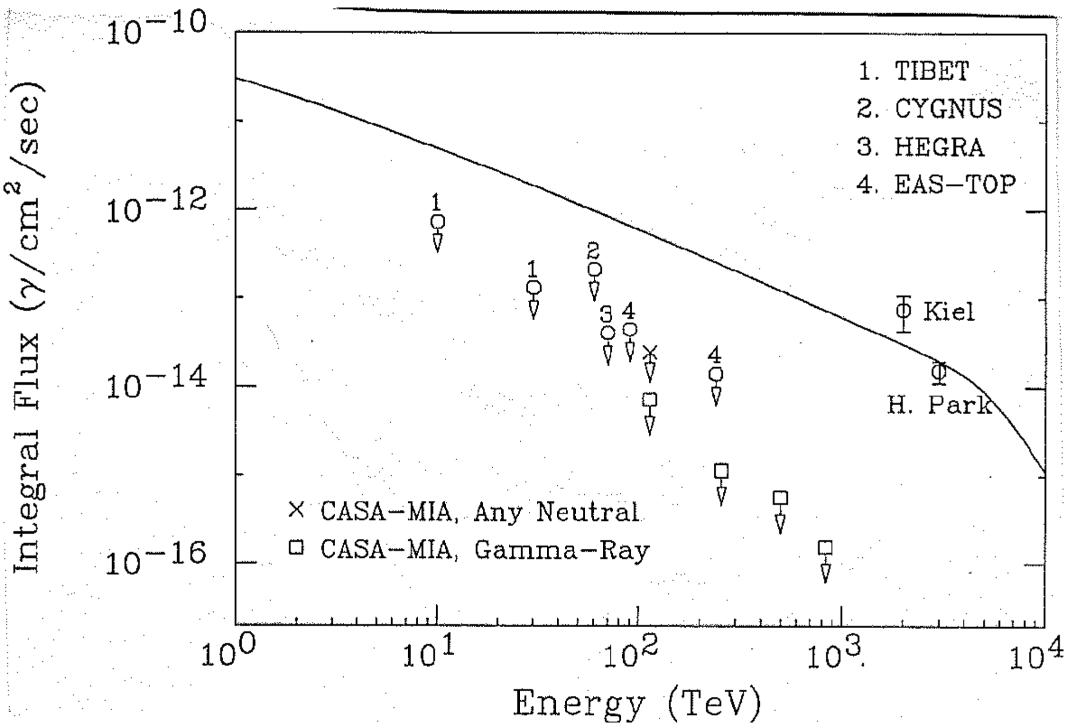

Figure 1.2: Limits on steady flux from Cygnus X–3

Table 1.1: General properties of the 6 Pulsars detected with EGRET

Pulsar	$P(s)$	$\dot{P}(10^{-15}s/s)$	$\tau(yr)$	$B(Gauss)$	Dst (kpc)
Crab	0.033	421	1.3 10^3	3.8 10^{12}	2.0
Vela	0.089	125	1.1 10^4	3.4 10^{12}	0.5
B1704–44	0.102	93	1.7 10^4	3.1 10^{12}	1.8
B1951+32	0.040	5.85	1.1 10^5	4.9 10^{11}	2.5
Geminga	0.237	11	3.4 10^5	1.6 10^{12}	0.25
B1055–52	0.197	5.83	5.3 10^5	1.1 10^{12}	1.5

Table 1.2: Gamma–ray properties of the EGRET Pulsars

Pulsar	$\dot{E}$ $(erg\ s^{-1})$	F_γ $(erg\,cm^{-2}s{-}1)$	$L_\gamma(erg\ s^{-1})$	γ	η
Crab	4.5 10^{38}	1.0 10^{-9}	3.9 10^{34}	2.15	0.00009
Vela	7.0 10^{36}	7.1 10^{-9}	1.7 10^{34}	1.70	0.0024
B1704–44	3.4 10^{36}	8.3 10^{-10}	2.6 10^{34}	1.72	0.0077
B1951+32	3.7 10^{36}	2.4 10^{-10}	1.4 10^{34}	1.74	0.004
Geminga	3.3 10^{34}	3.7 10^{-9}	2.3 10^{33}	1.50	0.0068
B1055–52	3.0 10^{34}	4.2 10^{-10}	9.3 10^{33}	1.18	0.31

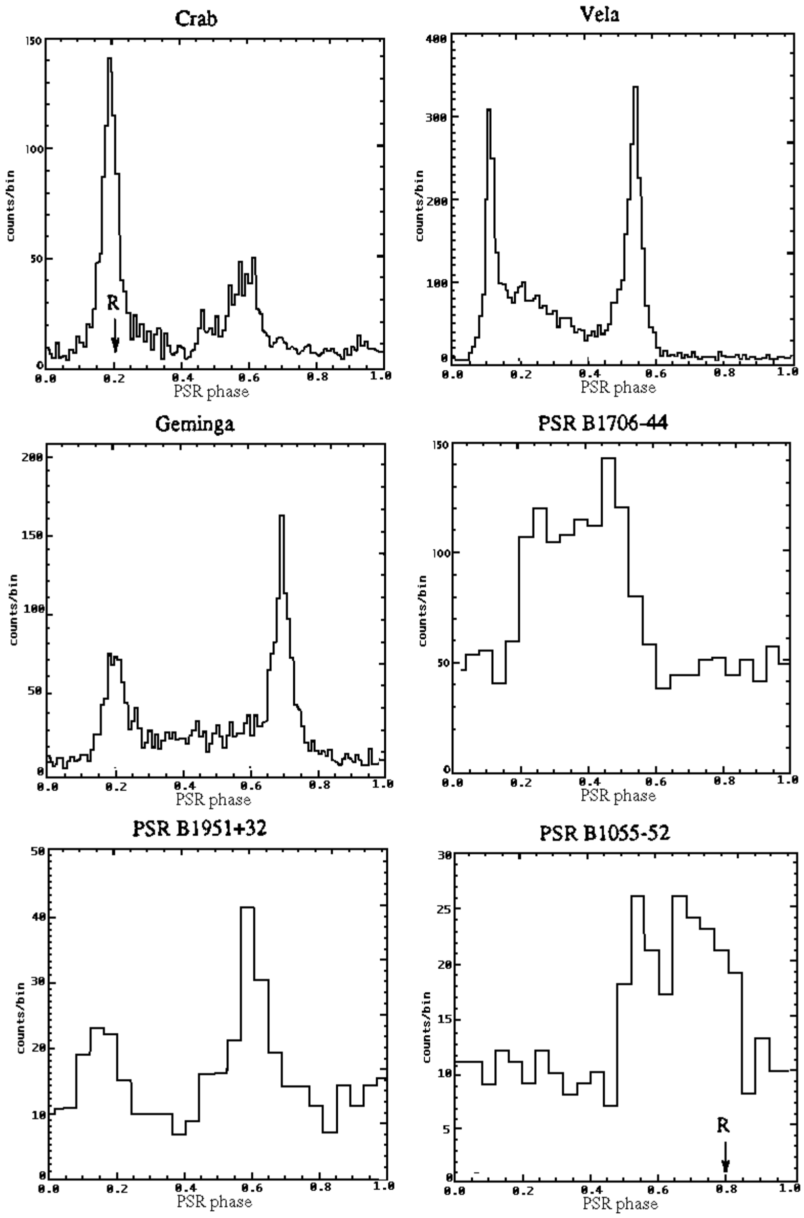

Figure 1.3: Light curves of the six EGRET γ-ray Pulsars

sources are fast, highly magnetized, young nearby pulsars with γ-ray luminosity by far greater than the radio luminosity. As a general trend, we observe that the spectrum hardens and the efficiency increases with the dynamical age.

Pulsed γ-emission of the oldest pulsars is thus characterized by a very flat spectrum. However, no steady pulsed TeV component has been observed by ground based detectors. Also the imaging technique employed by Whipple failed to identify periodic emission from the Crab pulsar and other northern sources. Flux limits for steady pulsed emission at TeV energies from the known γ-ray pulsars are two order of magnitude (at least) lower than the extrapolation of the power spectra found in the GeV range as shown in fig. 1.4. This figure includes also the MeV-pulsar PSR1509-58 not observed by EGRET. Energy spectra can be represented by the form $E^{-\gamma}e^{-(E/E_o)^\alpha}$ where E_o is a cut–off energy and α measures the strength of the cut–off. Acceptable fits are shown in fig.1.4 by dashed lines. It appears that the MeV to GeV spectra cannot extrapolate into the TeV region and that the emission is confined at energies below $100\,GeV$. The evidence of an energy cutoff is already seen in the CGRO (COMPTEL+EGRET) data, with the only exception of PSR1951+32, the more recent pulsar observed by EGRET not included in fig.1.4. As shown in fig.1.5 this pulsar has the smallest observed gamma-ray flux but its energy spectrum extends up to $30\,GeV$ without any apparent cutoff making it a candidate for observation at $100\,GeV$ energy.

Radiation models for the gamma ray emission of pulsars generally fall into two categories: the *"polar cap"* and *"outer gap"* models [9]. In both primary electrons are accelerated to energies above $10^{12}\,eV$ in order to explain the observed γ-ray emission. The models differ in the proposed location of the emission sites involving differences in the radiation and transport processes.

The non-detection of VHE photons, while imposing severe constraints to models with γ-production in sites far from the stellar surface, is entirely consistent with the polar cap model. Then, the observation of "$100\,GeV$ photons" or the determination of upper limits are an important information for a better understanding of the nature of the γ-ray pulsars.

1.1.4 Pulsar : Unpulsed emission

Unpulsed emission from the Crab region has been primarily measured by COS-B up to about $1\,GeV$. Results from EGRET observations are consistent with the COS-B data but extend the energy range up to $10\,GeV$ [10]. The integral unpulsed flux can be fitted by a power law with a spectral index of 1.3 . However above $1\,GeV$ the observed data points appear to be well above the fitted power-law, eventually indicating a hardening of the spectrum above this energy. No continuous source emission however is observed from the direction of the other high energy gamma ray pulsars. For instance, the steady emission from Vela pulsar is quoted by EGRET below 10% of the pulsed emission at $E > 1\,GeV$.

At TeV energies the unpulsed emission emerges as the main component from two of the previous gamma ray pulsars, Crab and PSR1706-44. It is notable that they are associated to supernova remnants. The fluxes above $1TeV$ reported in fig.1.6 come from the observations of

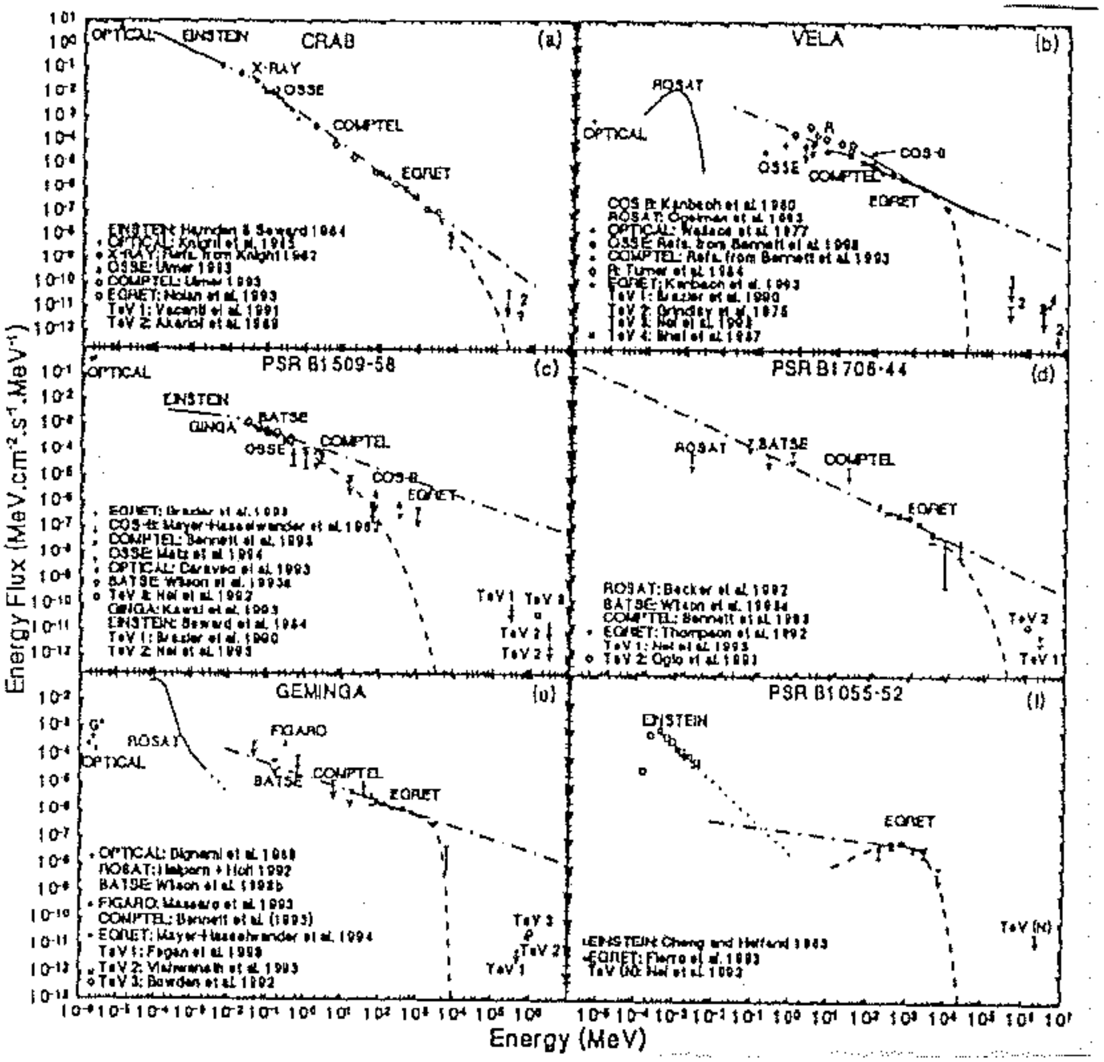

Figure 1.4: Differential energy spectra (optical to TeV) of six CGRO pulsars in panels (a) to (f)

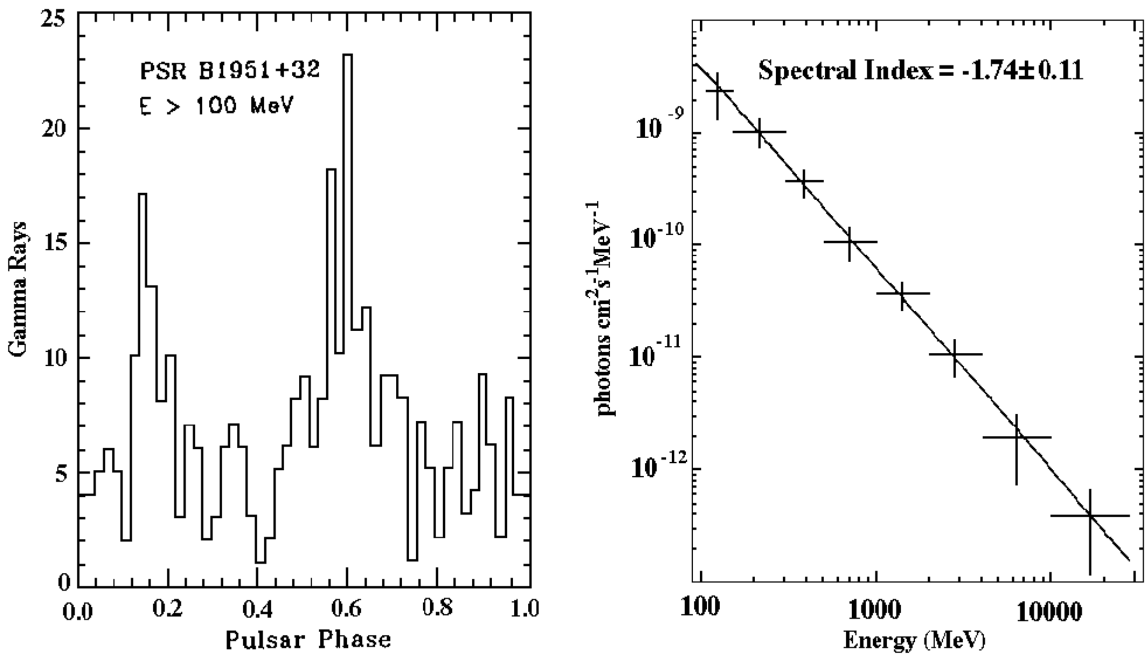

Figure 1.5: Left: Light curve for $E > 100MeV$ within a fixed 1^o radius around PSR1951+32. — Right: Phase averaged energy spectrum of pulsed gammas at $E > 100MeV$ in the two peaks shown in a) after subtracting the background

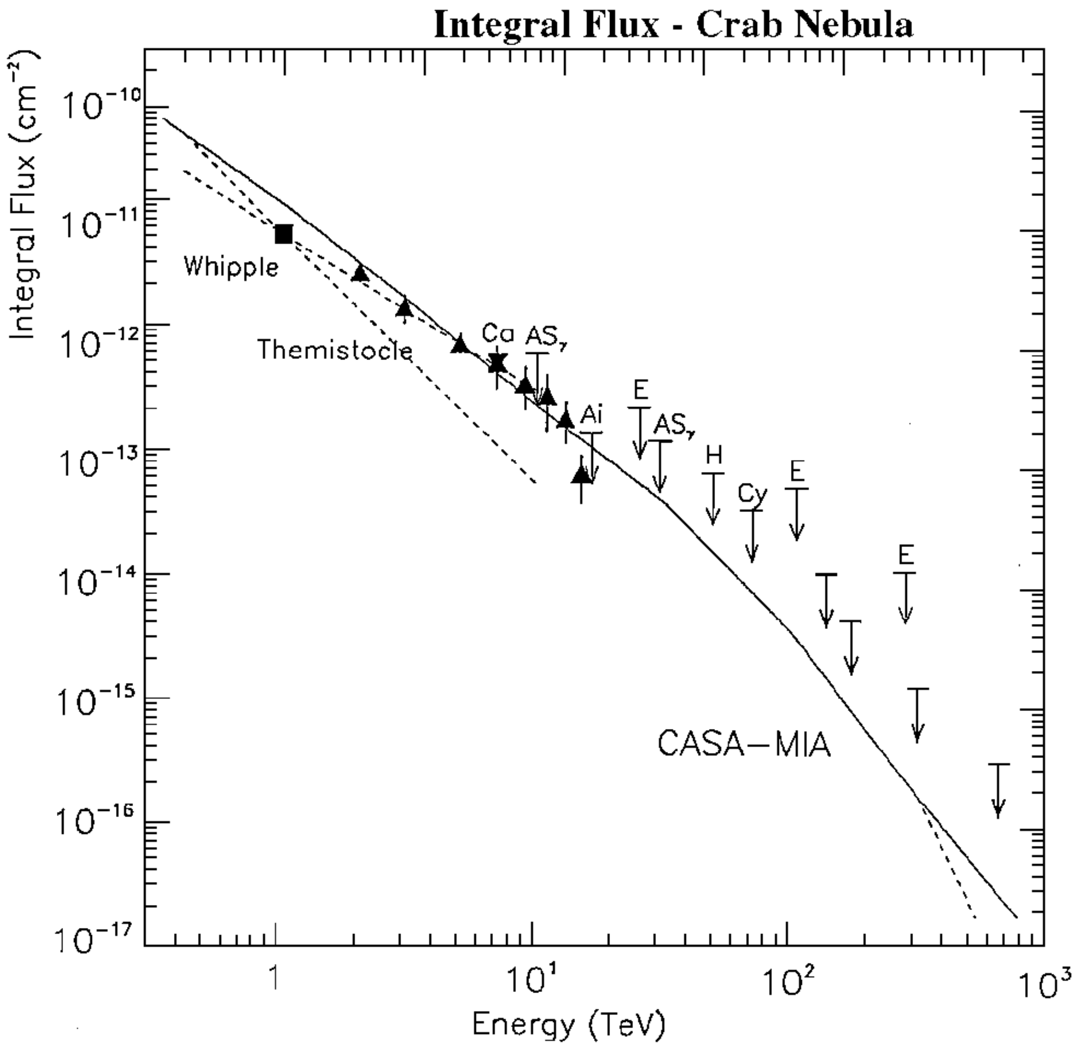

Figure 1.6: Plot of the integral flux of γ-rays from the Crab Nebula. Upper limits are set by air shower experiments.

the atmospheric Cerenkov telescopes (Whipple, Themistocle, Asgat, Hegra, Cangaroo) [11]. The smooth curve in the figure is the model of de Jager and Harding [12]. They are about two orders of magnitude smaller than the extrapolated value from GeV region of the pulsed emission. The spectra quoted by Whipple and Themistocle collaborations (dashed lines) are about a factor of 2 less than the previous determination and differ substantially each other. No data exist from EGRET energies up to the Whipple threshold ($400\,GeV$). Thus, while the Crab remains a well established source of VHE photons extending at least up to $15\,TeV$, the absolute gamma ray intensity, the spectral slope and the shape of the spectrum are not well defined. The measure of these parameters is of fundamental importance to discriminate between different models proposed to explain the unpulsed emission. A firm determination of the unpulsed spectrum of HE/VHE gamma rays from Crab, (and PSR1706-44) will be crucial to clarify the high energy limit of particle acceleration in plerions and to distinguish between the proposed mechanisms.

1.1.5 Supernova Remnants

Shock acceleration in expanding supernova remnants is widely believed to be the mechanism responsible for the origin of cosmic rays with energies up to at least $\sim 10^{14}\,eV$. In fact supernova blast shock seem to be one of the few galactic sources capable of satisfying the energy budget of cosmic rays and naturally providing an energy spectrum compatible with the expectations. Due to an energy-dependent mean escape time from the Galaxy, the spectrum produced in these sites should be somewhat harder than the observed spectrum of cosmic rays. Thus, an integral spectrum below the knee $\sim E^{-\gamma}$, with γ ranging from about 1.1 to 1.4, predicted by all recent estimates for cosmic rays accelerated in SNRs by diffusive shock acceleration. Direct measurements of the cosmic ray spectrum from SNRs are not possible because charged particles are deflected by the interstellar magnetic field over distances ($< 10\,pc$) much shorter than the distances to SNRs (more than $1\,kpc$ from Earth). However, gamma rays from SNRs would be direct evidence that particle acceleration is taking place in these systems. In fact cosmic rays accelerated in a SNR should interact with other nuclei producing π^0 and, finally, high energy gamma rays. This picture is supported by the results of the EGRET collaboration which recently reported the association of six sources of $\geq 100 MeV$ γ-rays with SNRs [5]. The fluxes are near the limits of EGRET's sensitivity and apply to the regime below $100\,GeV$. If SNRs are the source of cosmic rays up to at least $10^{14}\,eV$, then due to the hard spectrum we might expect to see gamma emission at $GeV - TeV$ energies. According to the predictions of Drury at al. [13] and Naito and Takahara [14] the γ-ray flux at energies $> 100\,MeV$ expected from a SNR is

$$F_\gamma(> E) \sim 10^{-10} \cdot A \cdot f_\alpha \left(\frac{E}{1\,TeV}\right)^{-\alpha+1} \quad cm^{-2}s^{-1} \tag{1}$$

with

$$A = \theta \left(\frac{E_{SN}}{10^{51} erg}\right) \left(\frac{d}{1\,kpc}\right)^{-2} \cdot \left(\frac{n}{1\,cm^{-3}}\right)$$

where θ is the fraction of the supernova energy E_{SN} going into production of cosmic rays, d is the distance to the source, n is the ambient density, and $f_\alpha = 0.9 \div 0.2$ depending on the spectral index of the accelerated protons. We note that if SNRs are indeed the source of galactic cosmic rays, then the γ-ray luminosity and spectrum predicted by diffuse shock acceleration theories are tightly constrained by cosmic ray observations and are relatively model independent. According to (1) the luminosity of nearby SNRs should be sufficient for detection by sensitive experiments operating at VHE energies. For SNRs that are expanding into molecular clouds with $n \geq 10^{2 \div 3}\,cm^{-3}$ the detectability may be enhanced by higher density and the more compact emission region. Examples of such SNRs in the Northern Hemisphere are γ Cygni and IC433.

Whipple ($E_{th} = 300\,GeV$), Cygnus ($E_{th} \sim 100 \div 300\,TeV$) and CASA-MIA ($E_{th} = 100\,TeV$) experiments recently report results concerning a number of SNRs including five of the ones observed by EGRET [15]. No evidence for emission is observed. In fig.1.7 the gamma ray spectra according to the Drury et al. predictions (called DAV) for cosmic ray spectra $E^{-\gamma}$, $\gamma = 1.1, 1.2, 1.3, 1.4$, are plotted as a fraction of the predicted integral flux above $10^8\,eV$ and extrapolated to $10^{16} eV$ with no cut off. The flux limits from Cygnus and Whipple experiments are shown. Comparable upper limits are given by CASA-MIA. Provided the shapes of DAV's gamma ray spectra are correct, the normalized flux limits are only marginally consistent with the model extrapolation from spectra $E^{-1.3}$ or harder, indicating steeper spectra as $E^{-1.4}$ or some spectral cut-off at energies below a few hundred GeV. A cosmic ray spectrum steeper than $E^{-1.3}$ would imply that the spectral contribution of the mean escape time from the Galaxy does not exceed $E^{-0.3}$, still compatible with predictions. On the contrary a spectral cut-off could contradict the hypothesis that Galactic cosmic rays below the knee are accelerated predominantly in the shocks of SNRs.

In conclusion, present experimental evidence provides significant constraints on SNR-shock acceleration models of cosmic ray origin. In order to clarify the nature of cosmic ray acceleration in SNRs, observations on a large sample of SNRs at a threshold energy of $100\,GeV$ are needed.

1.1.6 Molecular Clouds

The detection of gamma ray emission from nearby molecular clouds, located away from Galactic plane, can be used to study the cosmic ray density and the properties of the interstellar medium. Enhanced photon production above the background from a localized region is expected to be given by

$$\phi_\gamma \sim A \cdot N(H_I) + 2 \cdot A \cdot N(H_2)$$

where A is the gamma ray emissivity per H atom and $N(H_I)$ and $N(H_2)$ are the column

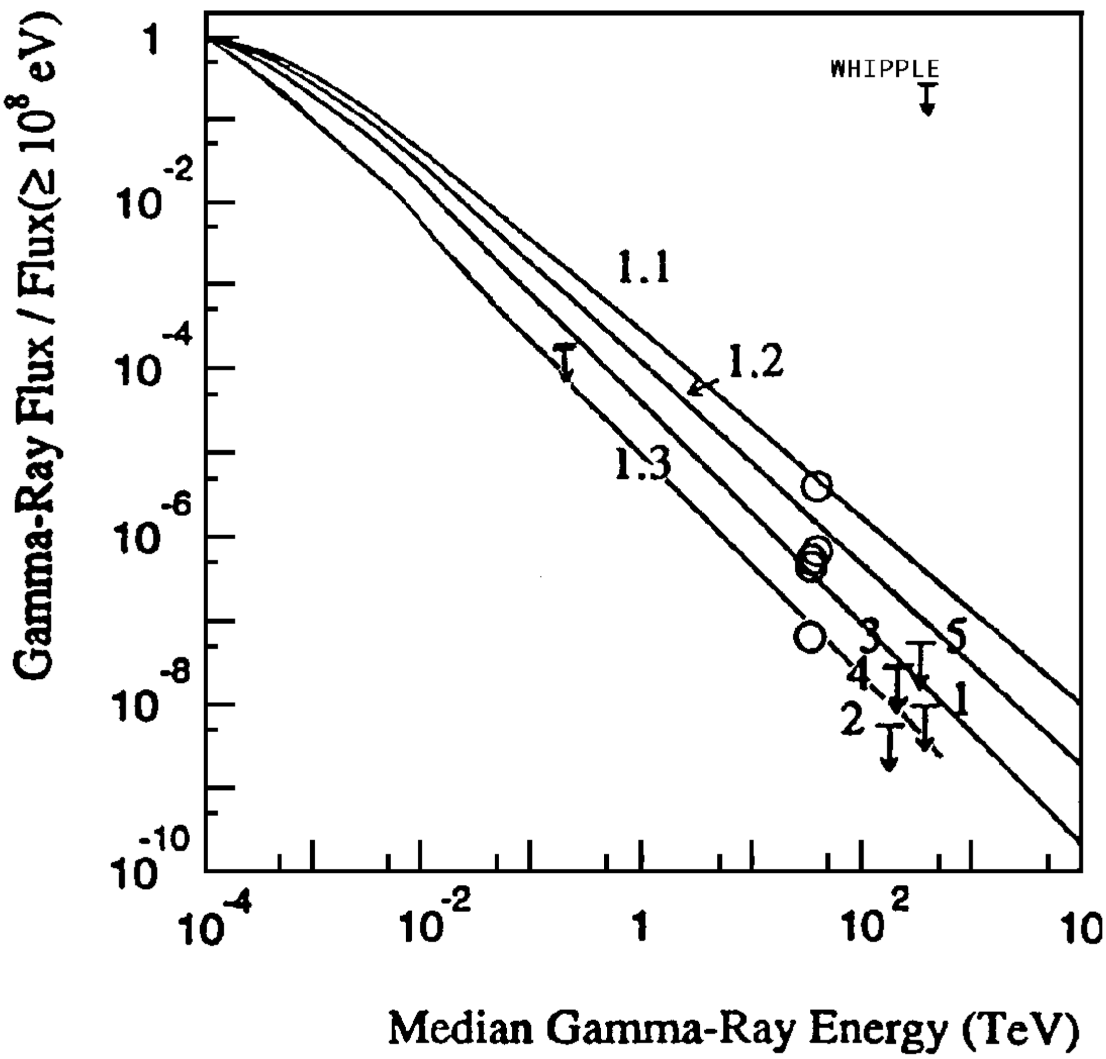

Figure 1.7: The γ ray spectra according to the DAV's predictions with integral cosmic ray spectra $\propto E^{-1.1}, E^{-1.2}, E^{-1.3}$, and $E^{-1.4}$. The Whipple ($300\,GeV$) and Cygnus upper limits are shown.

density of the atomic and molecular hydrogen respectively. If the distribution of interstellar matter within a molecular cloud is known from radio and infrared surveys - providing information, respectively, on H_I and H_2 densities - then the cosmic ray density within the cloud can be determined. Therefore, to the extent that the gamma ray production functions are understood, the energy spectra of cosmic rays at distances as far as 1 kpc of the Sun can be measured.

The gamma ray emission is primarily due to cosmic ray electron and proton interactions with matter (electron bremsstrahlung and nucleon-nucleon interaction) and, to a lesser extent, from electron interaction with low energy photons. However, as for diffuse γ-ray production in the Galactic plane, the interaction of proton cosmic rays with interstellar gas remains the principal process contributing to the photon production above few GeV. Thus, high energy photons ($> 100 GeV$) provide a direct evidence of high energy (TeV) protons and can be used to search for cosmic ray sources embedded in clouds of gas and dust. The existence of these sources is expected because molecular clouds are usually observed as the sites of significant stellar activity and abundant massive star formation.

Molecular clouds which are well suited for these analysis include those which are nearby, within about 1 kpc, have masses greater than a few times $10^3\ M_\odot$, and subtend a large area, several tens of square degrees on the sky. Among these (listed in table 1.3 taken from reference [16]) the Orion and Ophiucus complexes, well out of the Galactic plane, were detected by COS-B and, recently, by EGRET [6] at $100\,MeV$ threshold energy up to $10GeV$. No evidence for variations of the cosmic-ray density is found in Orion, even if three regions in the EGRET maps are observed where the γ-ray intensity marginally ($< 3.5\sigma$) exceeds the model expectations. Two of these excesses have a counterpart in the first EGRET catalog, eventually indicating the presence of discrete sources. The observed γ-ray flux from the regions of more intense emission may exceed $8 \cdot 10^{-5} cm^{-2} s^{-1} sr^{-1}$ while the isotropic emission (extragalactic + CR interactions with ionized gas + inverse Compton contribution) is of the order of $2 \cdot 10^{-5} cm^{-2} s^{-1} sr^{-1}$. Since the spectral index in the energy range $100\,MeV \div 10GeV$ is about 2.1, an extrapolation to the $100\,GeV$ region provides an integral flux greater than $3 \cdot 10^{-8}\, photons \cdot cm^{-2} s^{-1} sr^{-1}$ detectable by ARGO.

The maps of gamma ray intensities, $E > 100\,MeV$, from the Ophiucus region for different viewing periods are shown in fig. 1.8. Regions with intensities greater than 10^{-4} photons $cm^{-2}\ s^{-1} sr^{-1}$ are shown in white. Two point sources are found, one of them identified with a quasar. The other source ($\Phi_\gamma(> 100\ Mev) \sim 1.1 \cdot 10^{-7}\ photons \cdot cm^{-2} s^{-1}$) has not yet been identified at other wavelengths. The integral γ–ray emissivity from Ophiucus region is found to be higher than that from Orion cloud , suggesting that the local cosmic ray proton density varies by at least 30% over the $\sim 600\,pc$ distance between Orion and Ophiucus. The partition of this difference between variations in cosmic ray electron and proton densities is not clear. On the contrary observations in the $100\,GeV$ energy region are free from similar uncertainties, since at these energies the photon emissivity is essentially related to the proton flux.

Table 1.3: Molecular Clouds within 1 kiloparsec of Sun

Region	l_{min}	l_{max}	b_{min}	b_{max}	v (km/s)	D (pc)	M $(10^5 M_{\odot})$	z (pc)	σ (pc)
Aquila Rift	18.5	34	−6	10	8	200	1.5	9	15
Aquila Rift	34	44	−4	4	8	200	1.5	9	15
Cloud A	44	49.5	−4	2	27	500	0.4	−7	14
Cloud B	44	54	−4	5	7	300	0.4	0	11
Cloud C	50	55	−1	3.5	24	500	0.3	5	12
Vul Rift	54	63	−3	5	10	400	0.8	5	12
Cyg Rift	63	86.5	−4	4	7	700	8.6	−4	24
Cyg OB7	87	99	−3	8	−1	800	7.5	41	52
Lindblad Ring	100	164	−4	10	1	300	1.6	22	28
"−12 km/s"	102	161	−4	10	−12	800	8.7	44	59
Cepheus	100	120	11	22	−5	450	1.9	131	133
Taurus	163	178	−22	−9.5	5	140	0.3	−37	38
Per OB2	154	162.5	−25	−7	5	350	1.3	−84	92
Per OB2	163	171	−9	−6	−3	350	1.3	−84	92
Mon OB1	197.5	205	−1	4	7	800	1.6	17	22
Orion A	208.5	218	−21	−14.5	5	500	1.6	−163	164
Orion B	202.5	208	−21	−6	5	500	1.7	−129	132
Mon R2	210	218	−14	−10	7	830	1.2	−182	183
Vela Sheet	272	279	−3	8	0	425	0.8	9	19
Cham	295	305	−20	−12	4	215	0.1	−60	60
Coalsack	300	307	−4	3	−4	175	0.04	−2	5
G317-4	315	320	−6	−2	−6	170	0.03	−11	11
Lupus	333	346	4	22	5	170	0.3	32	35
ρ Oph	350	2	13	24	3	165	0.3	35	39
ρ Oph	356	5	3	12.5	3	165	0.3	35	39
R CrA	357	4	−22	−14	6	150	0.03	−55	55
See ref. [16] for more details about this table									

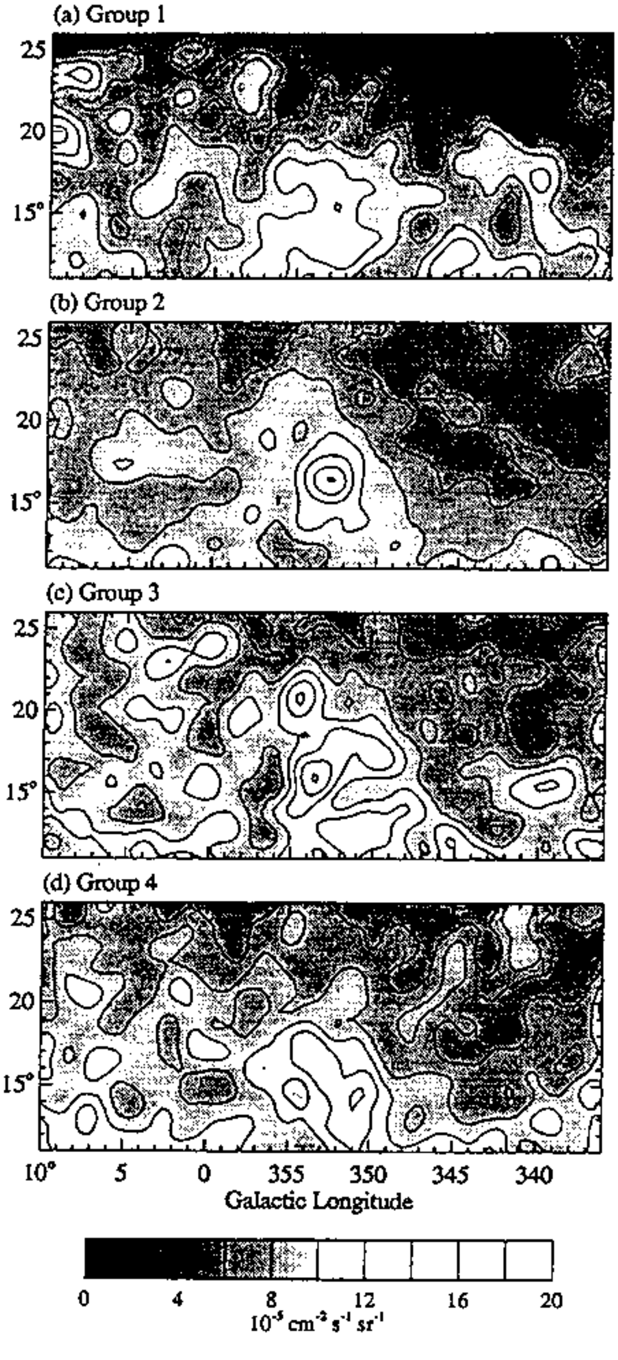

Figure 1.8: Intensities of gamma-ray emission, $E > 100\ MeV$ from the Ophiucus region for four groups of viewing periods. Regions with intensities greater than 10^{-4} photons $cm^-2\, s^{-1} sr^{-1}$ are shown in white.

1.1.7 Diffuse photons along the Galactic plane

Observations from satellite experiments SAS-II and COSB resulted in detailed maps of the Galactic γ-ray emission at energies $70\,MeV < E_\gamma < 5\,GeV$. The principal emission mechanisms for producing the diffuse gamma radiation in the Galaxy are, as previously mentioned, a) decay of π^0 produced in collision of cosmic ray protons with the interstellar gas, b) bremsstrahlung and inverse Compton of high energy electrons. However, at high energies the π^0 decay is by far the most important production mechanism for γ-rays. As a result, the photon flux is directly proportional to the linear matter density $[\rho \cdot R]$ (ρ = density, R = distance) and to the primary cosmic ray flux ϕ_{CR}, $\phi_\gamma \propto \phi_{CR} \cdot [\rho\, R]$. The column density of atomic and molecular hydrogen in the galactic plane can be reasonably inferred from radio-surveys of the Galaxy in the $21-cm$ line of atomic hydrogen and from millimeter surveys of the molecular emission lines of carbon monoxide (CO). The high energy γ-radiation, thus, can be regarded as a tracer of the distribution of high energy protons and nuclei in the Galaxy.

The measurement of the energy spectrum of diffuse γ rays above $100\,GeV$ is of great importance for discriminating acceleration and propagation sites and for understanding the cause of the 'knee' of cosmic ray spectrum. The COS-B experiment observed a difference in the spectral index of 0.4 at $5\,GeV$ γ-rays between the inner Galaxy ($|l| < 50^0$) and the outer Galaxy ($|l - 180^0| < 90^0$). The outer Galaxy seems to show a spectral index smaller by 0.4, which might be an important indication for the increase of the cosmic ray lifetime in the galactic halo [17]. At higher energies the experimental information is very poor. It consists of upper limits provided by the VEGA detector, loaded onto a cargo airplane, at $20\,GeV$ threshold energy and by the Whipple Telescope above $500 GeV$ [18]. In fig.1.9 the upper limit of the integrated intensities are shown. These results cannot provide any constraint to models. At energies $> 100\,TeV$ information comes from old data and, more recently, from CASA-MIA and EAS-TOP experiments [19], which give limits on I_γ/I_{CR} of $8 \cdot 10^{-5}$ ($|b| < 10^0$) and $2 \cdot 10^{-3}$ ($|b| < 2^0$) respectively. Data from CASA-MIA experiment could imply a maximum decrease of about 0.3 in spectral slope but they refer to energy greater than $100\,TeV$ and do not in any way restrict the general picture of the diffuse γ-ray production in the Galaxy. If the difference of ~ 0.4 in the power spectrum is correct the γ-ray integral intensity of the outer Galaxy become of the order of $2 \cdot 10^{-8}\, cm^{-2} s^{-1} rad^{-1}$ at a $100\,GeV$ energy threshold providing a good opportunity of detection by ARGO.

In fact, as shown in the next Chapter, the sensitivity of ARGO at $\sim 100\,GeV$ energy is largely sufficient to detect photon fluxes foreseen by the extrapolation of the COS-B low energy data. Finally, we note that the observation of γ-ray emission from extended sources - as the Galactic plane and molecular clouds - demands for detectors both sensitive to low energy photons and with large angular acceptance, requirements not easily fulfilled by Cerenkov telescopes.

The strong excess ($\sim 2-3$) seen in the direction of the Galactic centre by EGRET turns out to be of particular interest [20]. It is only seen at energies above $300\,MeV$ with a considerable flux $\sim 3 \cdot 10^{-7}\, cm^{-2}\, s^{-1}$. The dimension of the emission region should not

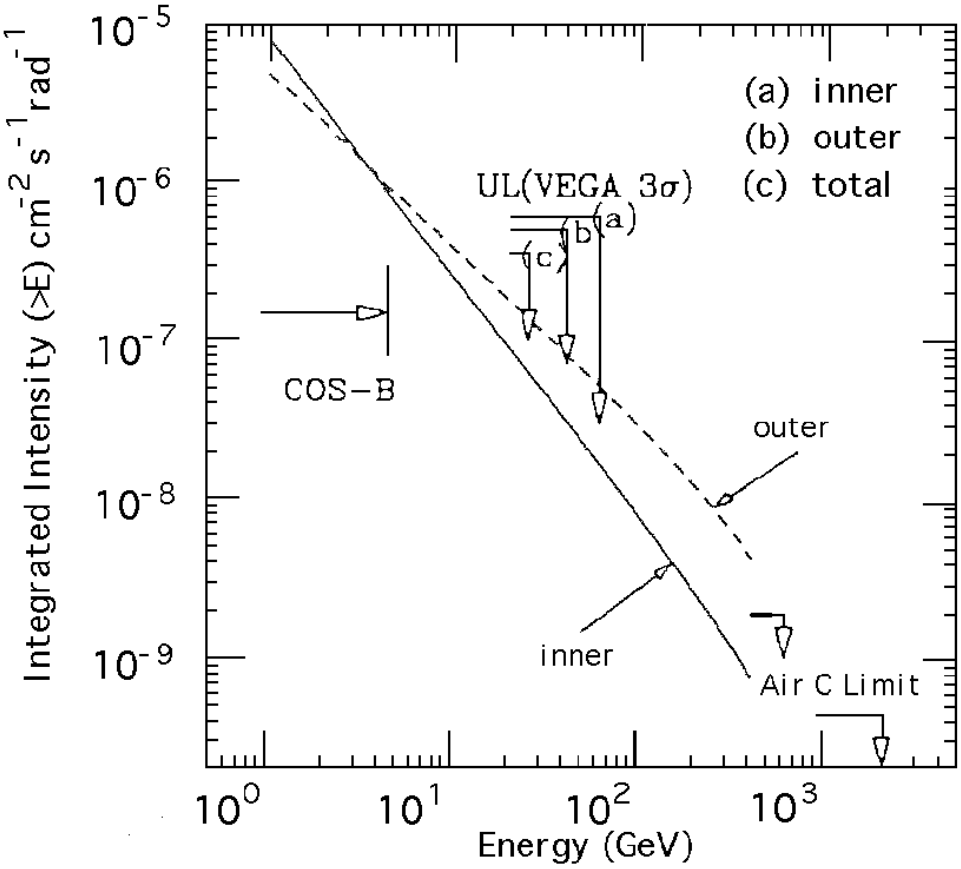

Figure 1.9: Upper limits of the integrated intensity of the galactic diffuse gamma–rays obtained by the VEGA experiment (for inner galaxy (a), for outer galaxy (b) and (c) for the total region) and by the Whipple Cherenkov telescope. The energy range observed by COS–B and its data extrapolation are also shown.

exceed $100\,pc$, eventually indicating a single compact source. A careful study of possible time variability and of the spectrum of the observed excess may help to solve this intriguing finding. At the site of Yanbaijing the Galactic centre is observed at a zenith angle of 60^0. Detection should possible only in the case of a spectrum extending deeply in the TeV region. Dedicated calculations are needed in order to asses the ARGO capability of observing γ-emission from the Galactic center. These results are not included in this document.

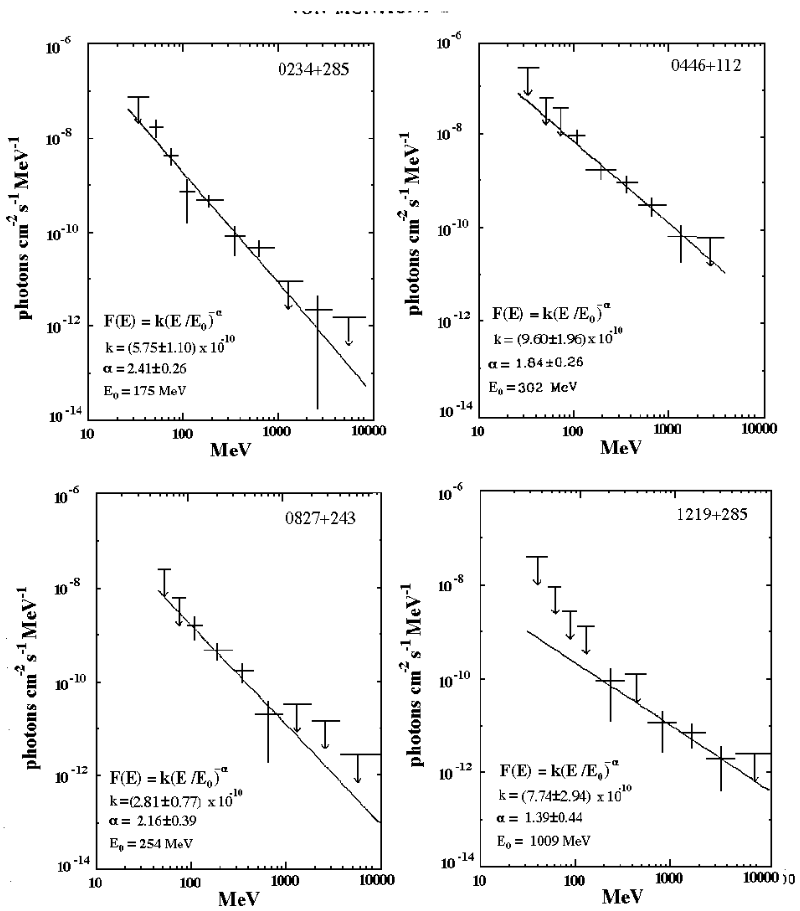

Figure 1.10: Differential photon spectra and the best fit power law for some AGNs observed by EGRET

1.1.8 Extragalactic Sources

One of the most important results of the EGRET detector has been the discovery that many active galactic nuclei (AGN) are strong γ-ray emitters with spectra extending to GeV energies. The 91 sources with $|b| > 10^0$ listed in the second catalog [4] include 40 AGN's identified with high confidence and 11 AGN's marginally detected. The energy spectrum of a few of them is shown in fig. 1.10. A short list summarizing the detection significances, flux values and errors, spectral index and redshifts can be found in ref. [21] and ref. [22] (44 AGN's detected with significance $> 4\sigma$). Common properties of these detections are the following:

1) all sources are core-dominated radio-loud objects with flat radio spectrum ($S_\nu \sim \nu^{-\alpha_r}$,

$\alpha_r \leq 0.5$). They are members of the blazar class of AGN's containing BL Lac objects, highly polarized ($> 3\%$) quasars (HPQ) and optically violently variable quasars (OVV);

2) the photon spectrum up to $10GeV$ is well represented by a power law $\frac{dN}{dE} \propto E^{-\gamma}$ with spectral indices ranging from 1.5 to 3.0. There is no evidence for a break in the energy spectrum. The luminosity above 100 MeV can be as high as 10^{49} erg/s (assuming isotropic emission), and in many cases is larger than the luminosity emitted in the rest of the electromagnetic spectrum. A correlation is found between the γ-ray flux above $100MeV$ $[\phi_\gamma(> 100MeV)]$ and the $5GHz$ radio flux Fr; the limiting sensitivity of EGRET, $\phi_\gamma \sim 10^{-7}cm^{-2}s^{-1}$, corresponds to about $Fr > 0.5\,Jy$;

3) the sources for which the redshift is known are distributed over a wide range of z values from 0.03 to 2.23 . The distribution in z of the H.E. γ-ray sources is found to be quite similar to the distribution in z of the flat spectrum radiobright quasars. No significant correlation of γ with z is observed;

4) many of the sources exhibit variability in the gamma-ray band on timescales from days to months indicating that the emission region is extremely compact.

In the simplest, unified picture of the AGN phenomena, blazars are those extragalactic radiosources whose jets are closely aligned with our line of sight. Since the observation of a strong and variable γ-ray luminosity implies that this emission is collimated or beamed, the natural conclusion is that GeV photons are associated in some way with the relativistic jets of blazars. This conclusion is reinforced by the fact that many active galaxies relatively close to Earth, such as radio-galaxies, Seyfert galaxies and radio-quiet AGNs, have not been detected in high-energy gamma rays [21].

The origin of the AGN γ-ray emission is currently the subject of much theoretical debate (see ref. [21] for an excellent summary). Many 'leptonic' and 'hadronic' models have been proposed which differ as regards the nature of the accelerated particles, the nature of the target and the site of production. Obviously, the extension of the spectrum up to TeV energies is more naturally predicted by hadronic models. A total of 35 AGNs, 15 detected at GeV energies by EGRET, have been included in the observing program of the Whipple experiment [23]. However, only two BL Lac sources - Mrk421 and Mrk501 - have been detected at an energy threshold of $300GeV$ with fluxes $\sim 1/3$ and $\sim 1/14$ of the Crab flux, respectively. This small detection rate makes it clear that γ-ray emission from blazars may extend well above $100\,GeV$, but this might not be a general property of these sources. After the original detection at TeV energies, Mrk421 has been monitored for about 90 nights. Observations on 1994 May 14 and 15 showed an increase in flux above the 'quiescent' 1993-1994 flux by a factor of 10, rising to this level within a period of 5 days. At this high level, Mrk421 was brighter at TeV energies than the Crab Nebula. This strong TeV outburst is reminiscent of the behavior seen for the strongest GeV EGRET sources – but not observed for Mrk421. This suggests that also in the VHE regime we can expect the same degree of variability as observed at GeV energies. Mrk501, at the same distance as Mrk421, is not included in the second EGRET catalog. A 2σ upper limit of about $10^{-7}cm^{-2}s^{-1}$ is provided in the first catalog. A spectral index $\gamma < 2.1$ can be deduced from these observations. Thus, in case of flat spectral slopes, we can expect observable fluxes above $100\,GeV$ also from sources non detected by EGRET.

The detection at $300\,GeV$ threshold of only two sources among the ones detected by EGRET has not a simple and straightforward explanation. Any reasonable conclusion is restricted by the fact that the AGNs detected by EGRET are time variable while the observation times of Whipple span typically from 1 to $2 \div 3$ hours. Apart from this problematic aspect, these results suggest that the spectrum of many sources could steepen between $10GeV$ and $300\,GeV$. Three possible origins of the steepening have been envisaged:

1) a steepening of the emitted spectrum in the rest-frame of the source;

2) absorption of the gamma rays in the ambient field close to the production site;

3) absorption of the gamma rays *'en route'* due to pair production on background infrared photons.

The observation of the cut-off in the gamma-ray spectrum of AGNs may be used to differentiate between emission models. Moreover, since these models imply a variety of relations between the emissions in different wavelength bands, simultaneous observations over the full range from radio to TeV energies are needed [24] (see fig.1.11). In addition to spectral considerations, the γ-ray time variability and its connection to the variability in the other wavebands will be important in evaluating the models.Thus, the operation of a sensitive and high duty-cycle detector in the $100\,GeV$ region could be crucial to clarify the present situation.

Are the AGNs the sources of extragalactic cosmic rays ?

The γ-ray intensities, spectral slopes, and detection of TeV photons from blazars suggest the presence of an extraordinary source of extremely energetic parent particles with spectra even slightly harder than the observed spectrum of ultra-high energy cosmic rays. For instance, in the PIC (proton-initiated cascade) model of Mannheim and Biermann [25] protons are accelerated by diffusive-shock acceleration up to $\gamma_p \sim 10^{10} \div 10^{11}$. Radiogalaxy hot spots and blazar jets have been suggested as sources of the highest energy cosmic rays [26]. A recent analysis [27] finds that the events with energy $> 4 \cdot 10^{19}\,eV$ are concentrated around the direction of the supergalactic plane where a large number of nearby powerful radio-galaxies are located. The distance of these sources does not exceed $100\;Mpc$ - preventing the absorption of ultrahigh energy cosmic rays on the microwave background field - so that γ-rays associated with such sources should not suffer any appreciable attenuation up to energies of $\sim 10^{13}\,eV$. Two radiogalaxies (Cyg A and M87) among the ones suggested in ref. [27] as specific candidate sources of $> 10^{18}\;eV$ cosmic rays have been observed by EGRET which provides only a $2\,\sigma$ flux limit $\phi_\gamma(> 100\;MeV) < 1.7 \cdot 10^{-7} cm^{-2}s^{-1}$ and $0.5 \cdot 10^{-7} cm^{-2}s^{-1}$ respectively. Also for Cen A EGRET provides only an upper limit of $1.5 \cdot 10^{-7} photons/cm^2 \cdot s$

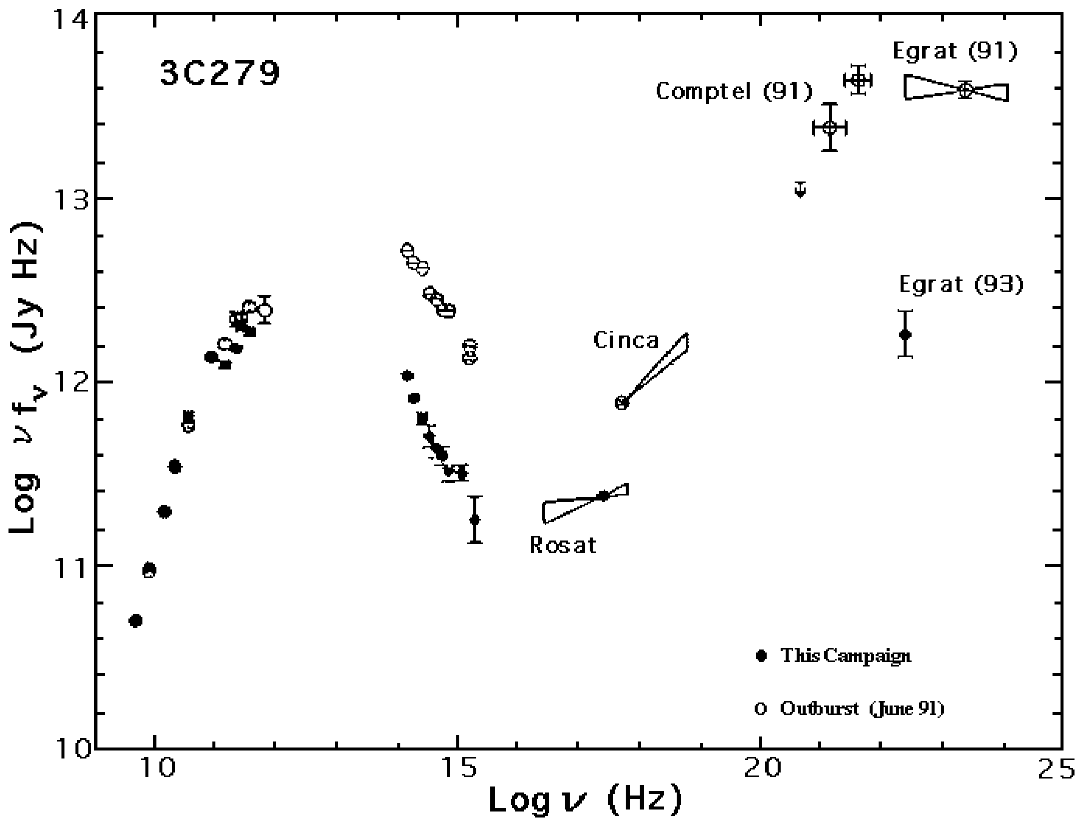

Figure 1.11: Radio to γ ray energy distribution of 3C279.

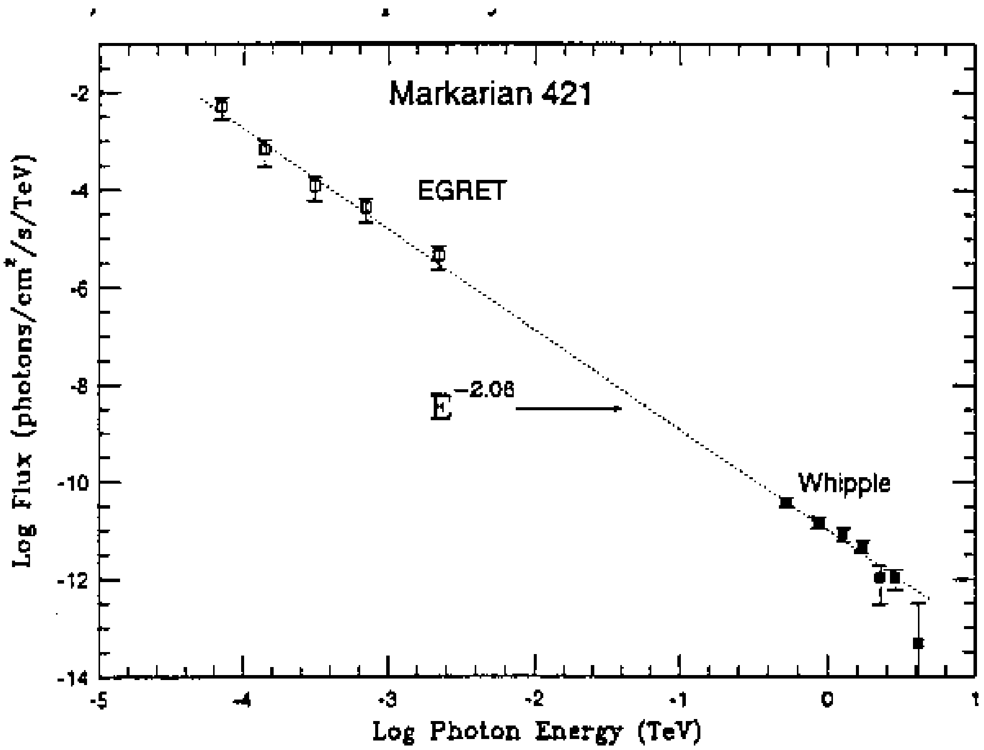

Figure 1.12: Differential Energy spectrum from the EGRET and Whipple observations of Mrk 421

at 100 MeV threshold. As discussed for Mrk501, these results do not exclude the possibility of observing VHE photons from these galaxies.

May the AGNs provide a long base-line photon beam ?

The absorption of γ-rays due to the interactions on the background photons may be used to measure the Hubble constant H_o in an original way [28]. We recall that the high energy tail of γ-ray spectrum would be absorbed in the $\sim$ 100 $GeV \div 10\,TeV$ region by the intergalactic photon field in the infrared region. The optical depth for γ-rays is then roughly given by $\tau \sim n_{IR}\sigma_{\gamma\gamma}d$ where n_{IR} is the infrared radiation field density, $\sigma_{\gamma\gamma}$ the cross section for $\gamma - \gamma$ absorption and d the distance obtained from the redshift and from H_0. The drop of the spectrum of Mrk421 (z=0.031) at energies above 1 TeV, see fig. 1.12, has been interpreted as due to absorption and used to determine an upper limit to the density n_{IR} assuming a standard value of H_o. In fig.1.13 the expected optical depths for sources at different redshifts are shown [29]. It is clear that if we know n_{IR} independently we can

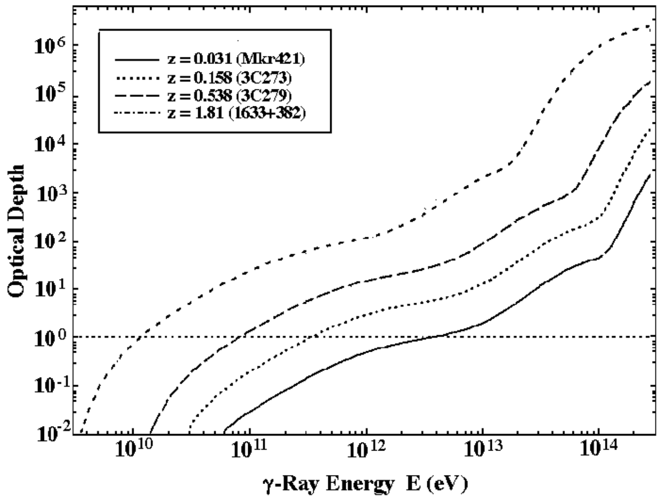

Figure 1.13: Optical depth as function of γ ray energy for different red shifts

determine τ (and therefore H_0) by comparing the cut off of various sources at different z. The DIRBE experiment on COBE and other satellite missions [30] are expected to yield a clear determination of n_{IR} in the near future.

On the other hand several sources are expected in the field of view of ARGO in the $100\,GeV \div TeV$ energy region. The study of the energy sources turns out to be of great importance to understand the absorption mechanism and, therefore, to obtain information on H_0 at significant redshifts.

Table 1.4: Some features of the three most intense bursts detected by COMPTEL during the first 22 months of operation

Date	Duration of the emission	Spectral index	$\Phi_\gamma(> 1MeV)$ $cm^{-2}s^{-1}$
910503	9 s	2.06 ± 0.27	0.61
"	12 s	"	"
910814	33 s	2.27 ± 0.26	0.53
930131	0.3 s	1.8 ± 0.4	9.37
"	0.1 s	"	"

1.2 GAMMA RAY BURSTS

Typical GRBs consist of brief ($10^{-2} \div 10^{2}\,sec$) flashes of photons in the energy range between a few keV and a few tens of MeV with associated fluences $\sim 10^{-6} \div 10^{-3}\,erg/cm^2$. This phenomenon represents one of the deepest mystery of the astrophysics since the problem of their origin is still unsolved. No one knows how they are produced or where they originate. The most recent all-sky survey carried out by the BATSE detector on board CGRO provided intriguing results which can be summarized in the following points [31]:

(1) GRBs are detected by BATSE ($20\,keV \div 2\,MeV$) at a rate of about one per day. This correspond to a full sky rate, at the BATSE sensitivity ($\sim 10^{-7}\,erg/cm^2$), of $\sim 800 \div 1000$ bursts per year;

(2) no quiescent counterpart in the optical, infrared, radio or X-ray range has been identified for any of the gamma-ray bursts;

(3) the distribution of GRBs is isotropic with no evidence for structure but radially non-homogeneous, possibly indicating an edge to the distribution;

(4) the time profiles show an enormous diversity in overall shape, pulse structure and duration, so there is no typical burst light curve;

(5) energy spectra can be highly variable with the time, and have their peak power at energies $> 100\,keV$. At energy less than a few hundred KeV, photon spectra can be approximated by an exponentially truncated power law $E^{-\alpha} \cdot e^{-E/E_o}$, while the higher energy component extending far beyond $1\,MeV$ may usually be described by a simple power law.

Bursts in the MeV region, as detected by COMPTEL on CGRO, exhibit a non-thermal, power law energy spectrum with a differential index in the range $-1.6 \div -2.8$, and integral fluxes ranging from 0.1 to 10 photons $(> 1\,MeV)/cm^2\,sec$. In Table 1.4 some features of the three most intense bursts detected by COMPTEL during the first 22 months of operation are summarized. GRBs 910503 and 930131 consist of two pulses separated by 36 s 0.8 s respectively. Of great relevance is the detection by EGRET of a few events showing emission extending with unbroken power law up to several GeV and lasting more than the low energy gamma emission. The EGRET observations of GRB's are reported in Table 1.5. All events

Table 1.5: EGRET observations of GRBs

Date	Maximum Energy (GeV)	Duration of high energy emission	Spectral Index
910503	10	84 s	2.2
910601	0.31	200 s	3.7
930131	1.2	100 s	2.0
940217	18	1.5 h	2.6
940301	0.16	30 s	2.5

have also been observed by BATSE and by COMPTEL. In three of them delayed GeV photons have been recorded. The unusual event of Feb'94, whose time evolution is shown in fig. 1.14, includes the detection of an $18\,GeV$ photon that arrived about 80 minutes after the original burst. A detailed analysis of these events can be found in ref. [32]; relevant features can be summarized as follows:

a) the high energy bursts detected by EGRET ($30\,MeV \div 20\,GeV$) are among the brightest bursts detected by BATSE however their low energy features are similar to many other bursts;

b) high energy emission is observed to last longer than at lower energies (compare for instance Table 1.4 and Table 1.5). The delayed emission of GBR 940217 was not seen at all by BATSE or by the detector on board the Ulysses spacecraft cfr. fig.1.14;

c) the high energy emission is the dominant part of the energy produced following the initial spike of intensity, and is a significant part of the energy produced in the spike;

d) it is not clear if delayed high energy emission accompanies all bursts. EGRET has had some exposure to over 150 BATSE bursts, but the effective area at high energy is rather low ($1000 \div 1500\,cm^2$) and depending on the burst direction, so that the photon flux could have been under the detection threshold;

e) the energy spectra in the overall MeV/GeV range follow a simple power law with no change in spectral index and no evidence of any energy cutoff.

Since the spectral indices are harder and the fluxes more than one order of magnitude higher that Crab Nebula, if the GRB spectrum extends up to about $50\,GeV$, a γ-ray flux could be visible to the ARGO detector.

A large variety of models and emission mechanisms has been proposed [33]. Three possibilities have been originally proposed: GRBs are produced in the solar system (e.g. in the Oort's cloud), or have a galactic or an extragalactic origin. According to these different hypothesis, the amount of energy required to explain their luminosity would range between $\sim 10^{28}\,erg$ up to $\sim 10^{51}\,erg$. However, the recent results of BATSE, mainly the isotropic distribution, rule out distant sources confined to the Galactic disk or nearby sources in the Galaxy leaving only two viable possibilities: either the burst sources are at cosmological distances or they form a very large galactic halo population. The cosmological model is at

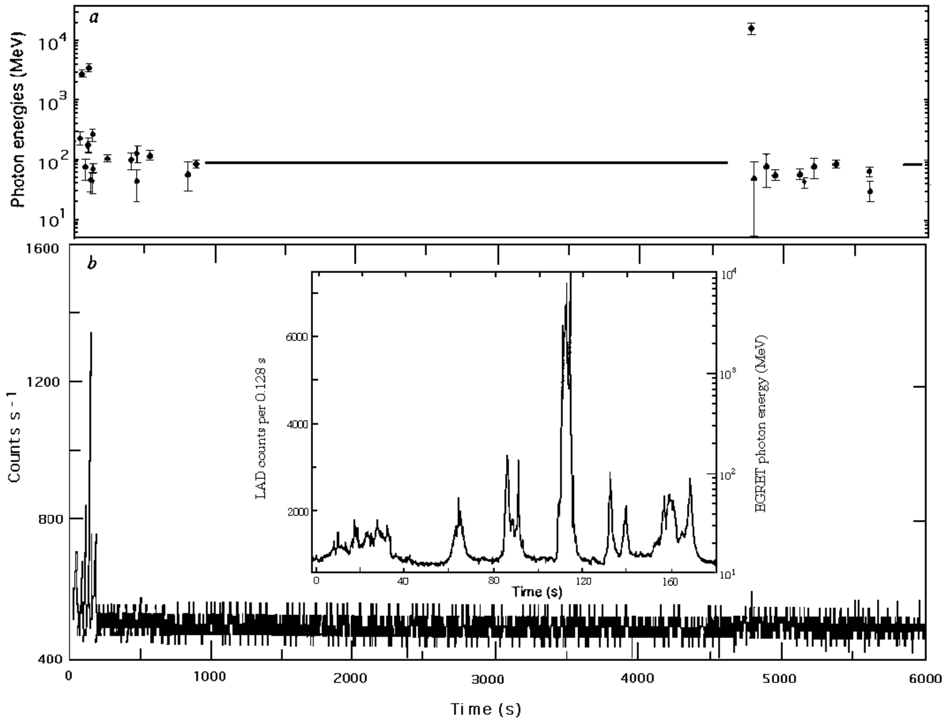

Figure 1.14: GRB 940217 : photon energies observed by EGRET as a function of time. The horizontal line indicates the periods where no data is available (a). Count rates ($25 \div 150 keV$) of the Ulysses satellite are also shown (b). The inset, expanded plot of the first 200 s as observed by BATSE, shows the arrival times and energies of the EGRET photons

the moment the most favoured, requiring a source luminosity of about $10^{51}\ erg$ in gamma rays. Such a large energy production together with the morphology of the time profiles can be provided, given conventional physics, by gravitational interaction occurring near the compact objects. Generation of γ-ray bursts during neutron star binary coalescence seems to be the most promising mechanism. It is based on a population (binary neutron stars) and a process (orbit decay leading to merger) for which we have direct evidence in our own Galaxy. Since the released energy is about $10^{54}\ erg$, energy to be converted in photons should be only $\sim 10^{-4} \div 10^{-3}$ of the total. If the red shift limits are of order unity then the total number of spiral galaxies within the sampled volume is of the order 10^{9}. The BATSE rate $\sim 10^{3}\ bursts/year$ thus implies one event per host galaxy every $10^{6}\ yrs$ in agreement with the estimates of $10^{-5\pm1} yr^{-1}$ mergers in the Galaxy based on galactic binary pulsars [34].

The neutron star merger model has a natural $z_{cut} \sim 2.5$ in agreement with the BATSE observation corresponding to a maximal redshift 2 ± 1 of bursts longer than $2\,sec$. In this scenario the brightest γ ray bursts should be accompanied by a gravitational pulse detectable at a rate of about once per year by devices with strain sensitivity greater than $10^{-21.4} h_0$ [$h_0 = H_o/100$, the Hubble constant in units of $100\ Km\ s^{-1}\ Mpc^{-1}$]. In the frame of this model, a neutrino burst could accompanies the photon burst. Present limits on the ν to γ flux ratio are greater than theoretical predictions. Future operation of the SuperKamiokande detector could reach a sensitivity not far from these predictions [36]. A coincident event within millisecond to seconds observed by gravitational wave, neutrino and photon detectors could be of great importance to provide information on the geometry and energy generation mechanism [35].

Observations of GRBs at energies of hundreds GeV, or more, would help determine whether or not the bursts are distributed cosmologically providing powerful constraints on the burster distance scale. In fact, photons $> 100\,GeV$ may be attenuated on cosmological distance scales by pair production off the intergalactic IR field. As shown in fig. 1.13 the detection of TeV photons should imply an upper limit $z \sim 0.1$[37].

Therefore the detection of high energy photons could suggest that GRB sources do not lie at cosmological distances ($z < 1$). Thus, a ground based detector with HE-VHE γ-ray sensitivity and a large solid angle aperture has the potential to provide a distance scale to the GRBs.

Based on BATSE statistics, more than 70 events per years will occur in the field of view of ARGO. According to EGRET statistics, a fraction $5 \div 10\%$ of them should have a high energy tail. However the possibility that high energy gamma rays are present in all bursts cannot be discounted. Very strong bursts like GRB 930131 could be detected by ARGO with high statistical significance above the background if the energy spectrum extends up to $25\ GeV$, as shown in the next Chapter.

1.3 ANTIPROTON FLUX AT $\sim 1\,TeV$ ENERGY

An important physics item that can be investigated by ARGO is the $\overline{p}$ content of the cosmic rays in the TeV energy region. Antiprotons are present in the cosmic rays flux. Fluxes

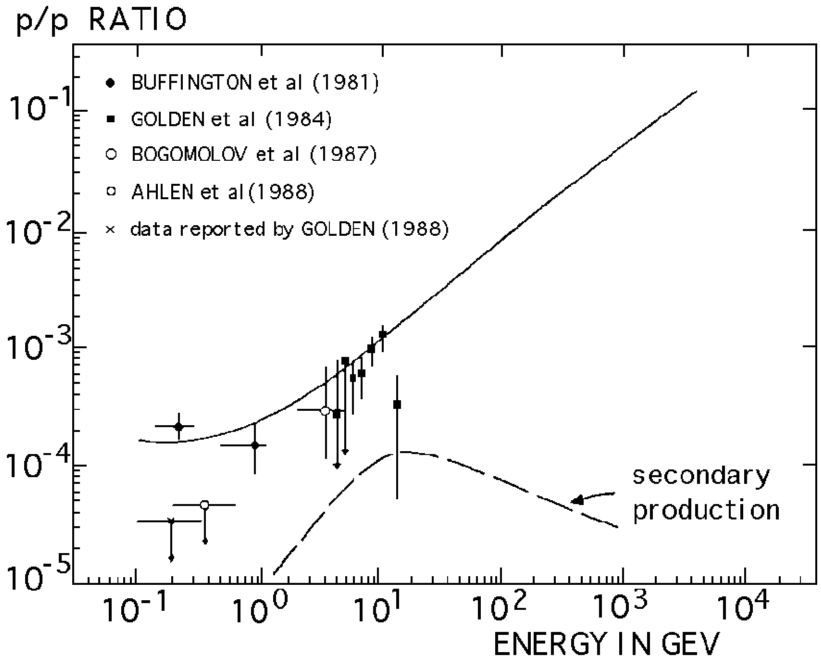

Figure 1.15: $\bar{p}/p$ ratio as a function of proton energy. Continuous line represents the prediction of Stecker and Wolfendale extragalactic model, dashed line the prediction of antiproton secondary production.

measured at energies $< 1\,GeV$ appear in agreement with predictions based on models of local production. Conflicting results are found at higher energies, and the rate measured in the $1 \div 10\,GeV$ energy range by some satellite and balloon experiments seems too large than that expected by proton interactions within the Galaxy. In the frame of theories in which matter and antimatter are created in separate regions of survivable size, Stecker and Wolfendale have suggested an extragalactic contribution to $\overline{p}$ flux [38]. On the assumption that the Universe is baryon symmetric and that higher energy cosmic rays are of extragalactic origin, these authors have shown that the ratio $\overline{p}/p$ should increase with energy to as much as 1% at $500\,GeV$ and more at higher energies. An estimate of its energy dependence is shown in fig.1.15 together with the experimental results. The effect of the galactic wind, not taken into account in that computation, may change substantially the prediction in the GeV energy region while does not practically affect the TeV region. A measurement in the TeV region should therefore permit to separate the two hypothesis of the galactic or extragalactic origin of these antiprotons.

Significant measurements of $\overline{p}$ in TeV region by means of satellite or balloon experiments are practically impossible due to the low flux and to the insufficient magnetic power achievable with a bending magnet necessary for the charge identification. An experiment like ARGO detecting extensive air showers with an excellent resolution on the primary direction ($\sigma_\theta < 0.4^0$) can measure the $\overline{p}$ content of the cosmic rays making use of the Earth's magnetic field in conjunction with a collimation by the Moon.

This method, described in detail in ref. [39], can be briefly summarized in the following:

a) the shadow of the Moon due to the absorption of the cosmic ray appears as an hole in the flux displaced with respect to the Moon direction by the effect of the Earth's magnetic field;

b) the magnitude of this displacement, obviously depending on the primary charge, turns out to be $\sim 1.7^0$ for protons at $1\,TeV$. Therefore, the good angular resolution of ARGO allows to have a good separation between the two holes due to p and $\overline{p}$ as discussed in Chapter 2.

It has to be stressed that the existing array operating at Yanbajing has already observed [40] the shift of the Moon shadow in the 10 TeV energy region, fig. 1.16. The displacement of 0.15^0 from the Moon's position is consistent with the expectation. However the high energy cut and the insufficient angular resolution ($\sim 0.87^0$) do not permit in this case a clear separation between the two shadows (proton and antiprotons) and therefore a significant limit on the antiproton flux cannot be obtained.

An upper limit on the $\overline{p}/p$ ratio of about 22% has been obtained by the same experiment looking at the Sun shadow [41]. This approach, however, suffers of the large instability of the interplanetary magnetic field heavily affecting the interpretation of the results. On the contrary, ARGO can exploit the geomagnetic field looking at the Moon shadow. The Earth's field is very stable with short time variations barely exceeding 3% over periods of a few hours only. In this respect, the ARGO detection of the Moon shadow resembles the ARTEMIS project [39] addressed to the same measurement by means of a Cerenkov telescope operating in the UV range. It has to be remarked that the Cerenkov approach involves a fully dedicated experiment always looking in the direction of the Moon while ARGO measures the $\overline{p}$ content simultaneously to all the other physics items discussed in this proposal.

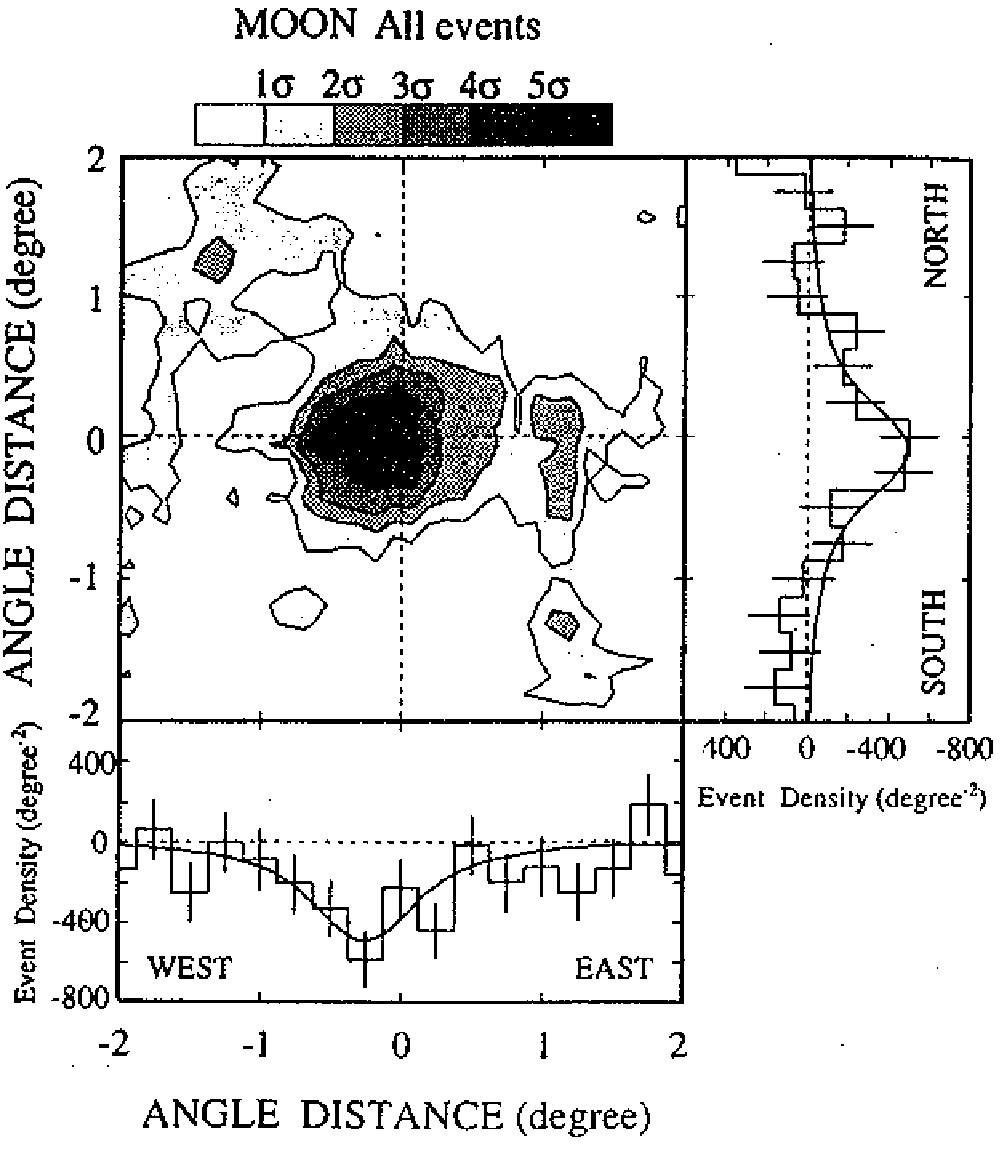

Figure 1.16: Arrival directions of all events in the area of $4^o \times 4^o$ centered on the Moon as measured by the AS_γ (Tibet) collaboration

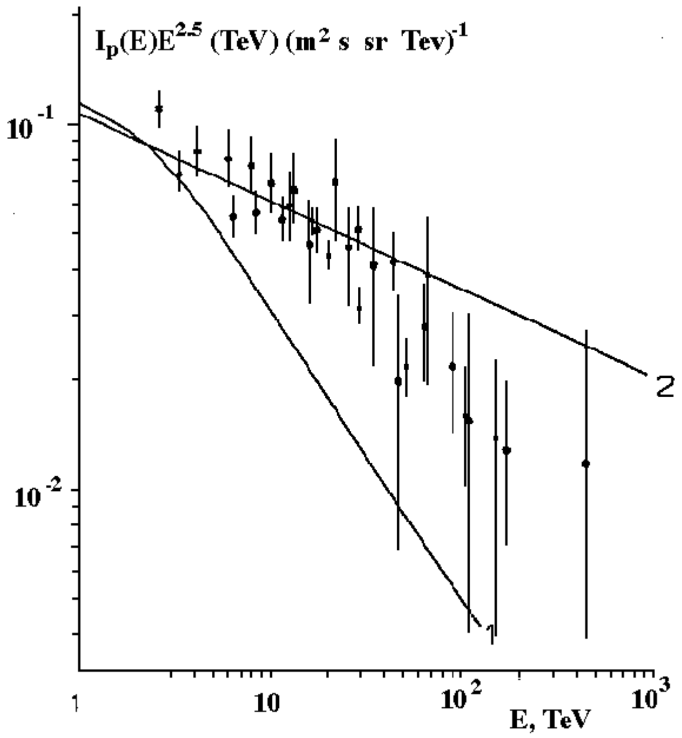

Figure 1.17: Energy spectrum of primary protons (see text).

1.4 THE PRIMARY PROTON SPECTRUM BELOW THE 'KNEE'

The problem of the behaviour of the power index of the primary proton energy spectrum received in direct measurements has been widely discussed in recent years. A summary of the experimental evidence is given in fig. 1.17 (from ref. [42]). Data are from different recent balloon and satellite experiments,curve 1 is a fit to Proton satellite results and curve 2 is the currently accepted spectrum obtained by extrapolating low energy data below 1 TeV to the air shower data above 100 TeV.According to JACEE data [43] the best fit to the proton requires two different slopes $\gamma_p = 2.64 \pm 0.12$ at $E_p < 40 TeV$ and $\gamma_p = 3.22 \pm 0.26$ at $E_p > 40\,TeV$. However,after addition of data from antarctic flights,the JACEE collaboration suggests a spectrum following a unique power law with $\gamma_p = 2.79 \pm 0.05$ [44]. Data from other experiments provide slopes with values between $\gamma_p = 2.75$ (curve 2) and $\gamma_p = 3.32$ (curve 1). According to these curves,the integral proton flux $I(> 5TeV)$ is affected by an uncertainty of about a factor of two. Since the air shower data may give information only on the all particle spectrum,this uncertainty reflects directly on the α/p ratio.

In the 'standard model' of cosmic ray origin and propagation in the Galaxy both shock acceleration at the supernova blast shock and deconfinement effects should be dependent on the particle rigidity. Since the heavier nuclei spectra do not exhibit any spectral cut-off at corresponding energies, the decline in the proton flux could be due to a change in the nature of the source or imply a different propagation history (the parameters derived from nuclei - that is primary/secondary ratios - may not be valid for protons).

From an experimental perspective these measurements at energies $10 \div 100\,TeV$ are in a region of transition between the feasibility of direct measurements and indirect air shower measurement at higher energies. Direct measurements suffer of lack of statistics (only 30 protons $> 20\,TeV$ have been observed in 12 flights by JACEE !), calibration problems in deriving the energy from ionization calorimeters or emulsion chambers and, finally, normalization problems in comparing data from different flights or experiments.

Concerning indirect methods,the measurement of the muon energy spectrum can be used to constraint the primary proton spectrum.As the muon energy spectrum is related to the energy per nucleon and primary protons contribute essentially to the all-nucleon spectrum,any significant change of γ_p above about 1 TeV must be distinctly seen in the muon energy spectrum. Results concerning the muon energy spectrum lead to the conclusion that the primary nucleon spectrum is characterized by $\gamma \sim 2.7$, suggesting a primary proton spectrum as given by curve 2 of fig.1.17. Thus,there exists a serious contradiction also between muon data and satellite results taken as a whole [42].

The energy region below 100 TeV is only marginally accessible to current air shower arrays. In the array operating at Mt. Chacaltaya (BASJE Collaboration) the 100% triggering efficiency is reached at energies above $60\,TeV$ [44] because of a too large detection spacing ($15\,m$), so that a measure of the proton spectrum in not attainable. For similar reasons the full efficiency of the AS-γ array at Yanbajing is reached at energies above $100 TeV$, preventing any sensitive analysis of the proton spectrum below this energy.

On the contrary, ARGO detector can attain the full efficiency near the vertical at proton energies $> 5\,TeV$ in such a way providing a detailed and unbiased measurement of the electromagnetic component of proton-induced air showers in the range $10\,TeV \div 200\,TeV$.

1.5 SUN AND HELIOSPHERE PHYSICS

The ARGO detector realizes an unique device for studying and monitoring from the Earth the whole system: Sun, interplanetary medium and geomagnetic field. The possibility of measuring with a rather good resolution both the energy of single primary particles above 10 GeV and their asymptotic directions of incidence outside the geomagnetic field, is not operating in any other ground-based instrument. Moreover, the ARGO detector covers a large energy interval of primary cosmic ray particles, partially overlapping at lower energies to that studied by the world-wide neutron monitor network and extending up to the TeV region with relatively high statistics. In figure 1.18 we show the asymptotic directions of the cosmic rays, with different primary rigidity, incident on each telescope at Nagoya (Japan), which is in a geomagnetic position similar to the Yanbajing laboratory. We notice again the great importance of measuring at the same time energy and arrival direction of cosmic ray particles to obtain detailed information on tridimensional aspects of the cosmic ray modulation in space. Studies which can be faced with ARGO are briefly summarized in the following:

1. Magnetic field of the outer atmosphere of the Sun. Observations of the sun shadow at high energies (> 200 GeV), i.e. for particles with large gyroradius, allow one to study the general structure of outer magnetic field of the Sun and its time evolution on short (27-days) and long term (22-year heliomagnetic cycle). Measurements made during periods of solar magnetic field inversion and solar activity minima will be of great interest. Recently, the Tibet AS–γ collaboration [45] reported a yearly time variation of

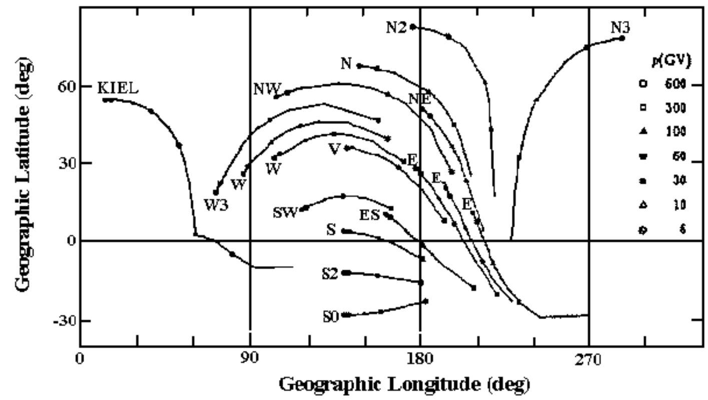

Figure 1.18: Asymptotic directions in the geomagnetic field of cosmic rays with different rigidity p at Nagoya (Japan).

the position of the Sun shadow from 1990 (maximum solar activity) to 1993 (decreasing phase) see fig.1.19. ARGO due to the lower threshold energy and higher statistics is expected to operate on a smaller time scale.

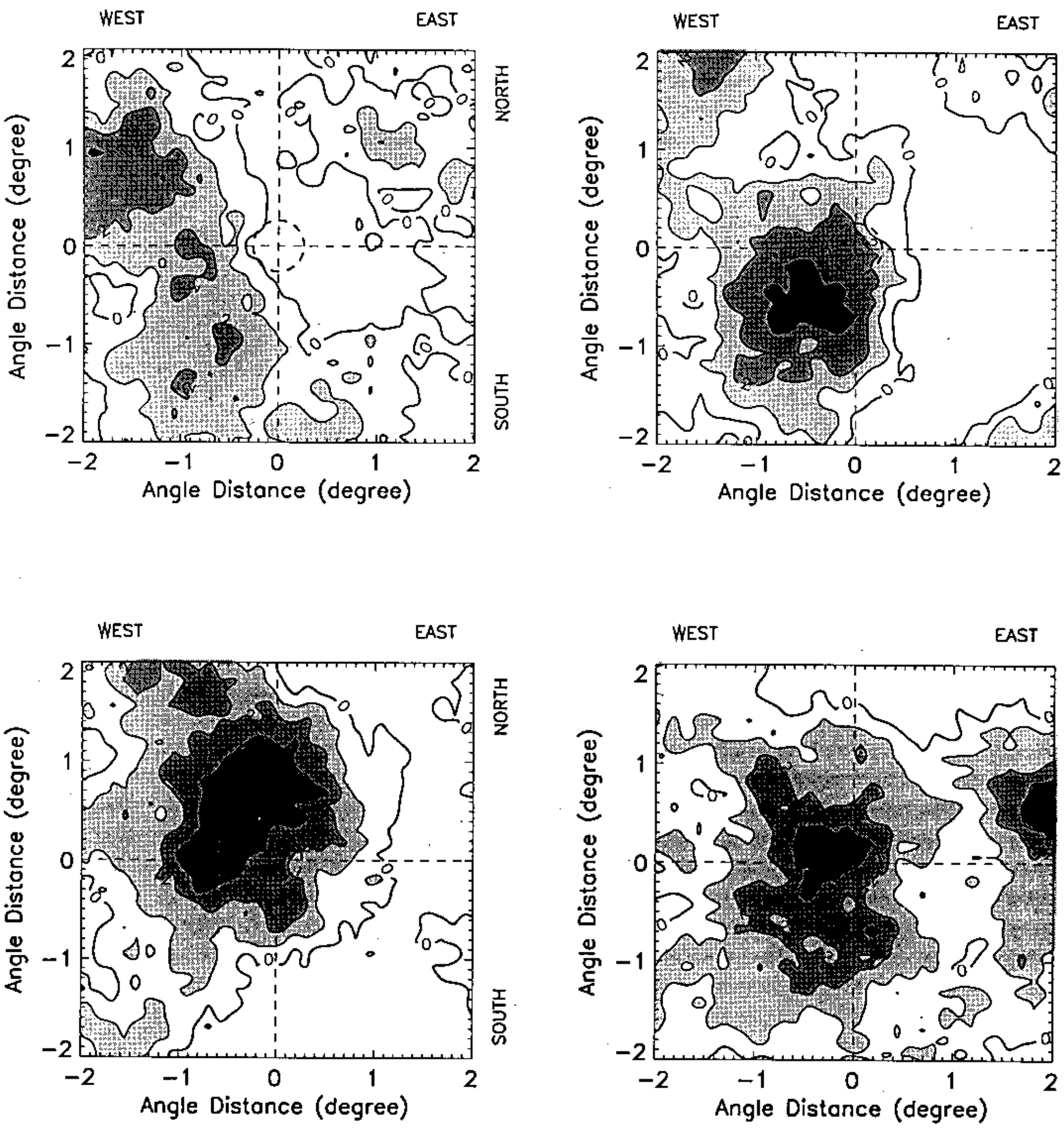

Figure 1.19: Sun shadow as seen by the As–γ collaboration (Tibet) in different years. Clockwise from up–left, from 1990 to 1993.

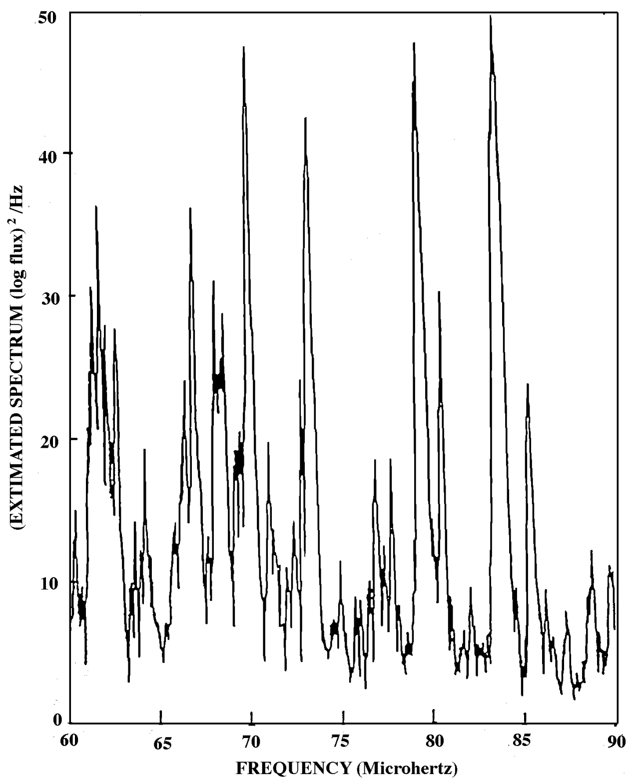

Figure 1.20: Logarithm of the flux of 38-53 keV electrons measured by Ulysses.

2. Solar Oscillations. Recent analyses on time fluctuations of particle-flux data from the spacecraft Ulysses [56] has revealed a sharp-line spectrum, fig. 1.20. The frequencies, reported between 1 and 140 μHz, are consistent with those estimated (but not yet confirmed) for gravity-mode oscillations of the Sun. From 1000 to 4000 μHz, the spectrum lines closely match the frequencies of most of the low-degree pressure modes that we know to be present. This is such a surprise that there is scepticism about their interpretation as a signature of solar oscillations [57]. If the measurements are confirmed, knowledge of the frequencies of a few g-modes will enormously enhance the ability to probe the interior of the Sun providing insight into issues ranging from the mixing of helium in the solar core to the solar neutrino problem. Solar wind research will be revolutionized as well if it turns out that much of the variability in the solar wind originates with oscillatory and non-oscillatory motions at the solar surface. On the other hand the only plausible mechanism advanced to explain the experimental results suggests that the particle flux oscillations are caused by variations of the solar and

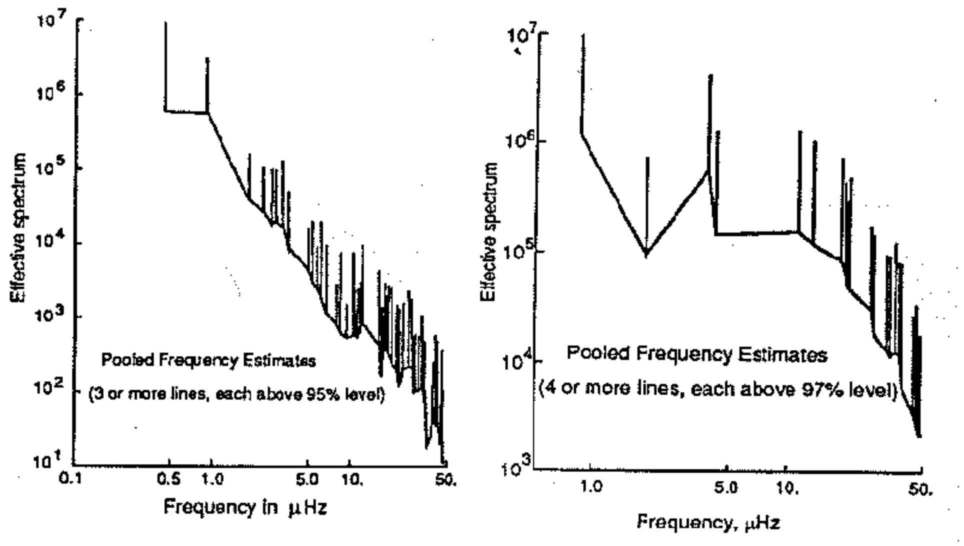

Figure 1.21: Power spectrum of particle flux variations (left), Ulysses data, and the IMF line spectrum (right)

Interplanetary Magnetic Fields (IMF). This interpretation is supported by the presence of many coincident lines in the power spectra of particle flux variations and IMF data (see fig. 1.21). Thus it is likely that the solar p and g modes are propagated into the interplanetary medium as fluctuations in the IMF. These fluctuations my have major implications for several important topics in the interplanetary physics as, for instance, the access of the galactic cosmic ray particles to the heliosphere and their propagation. Therefore, in principle, it would be possible, with the ARGO detector, to observe such variations of the solar and interplanetary magnetic fields both in the cosmic ray flux and in the sun shadow. Obviously, the achievable rate of observations with the cosmic ray flux makes this measure more suitable to look for the solar oscillations and, with ARGO–3600 configuration, we can hope to reach, as upper limit, frequencies of 10 μHz or more, i.e. the tail of solar g-modes towards the longest periods.

3. Moon shadow.The study of the Moon shadow and of its variations, also at relatively low energies, allows to analyze the external structure of magnetosphere as modified by the interaction with the solar wind, see fig.1.22. A day–night difference could be examined to search for any effect of the solar wind magnetic field beyond but not far the bowshock front in the day side of the Earth[58].

4. Solar Gamma and Neutron flares. Solar flares producing γ–rays with energy above $10 GeV$ and, therefore above the threshold of ARGO, are very exceptional (2-3 in a solar cycle).

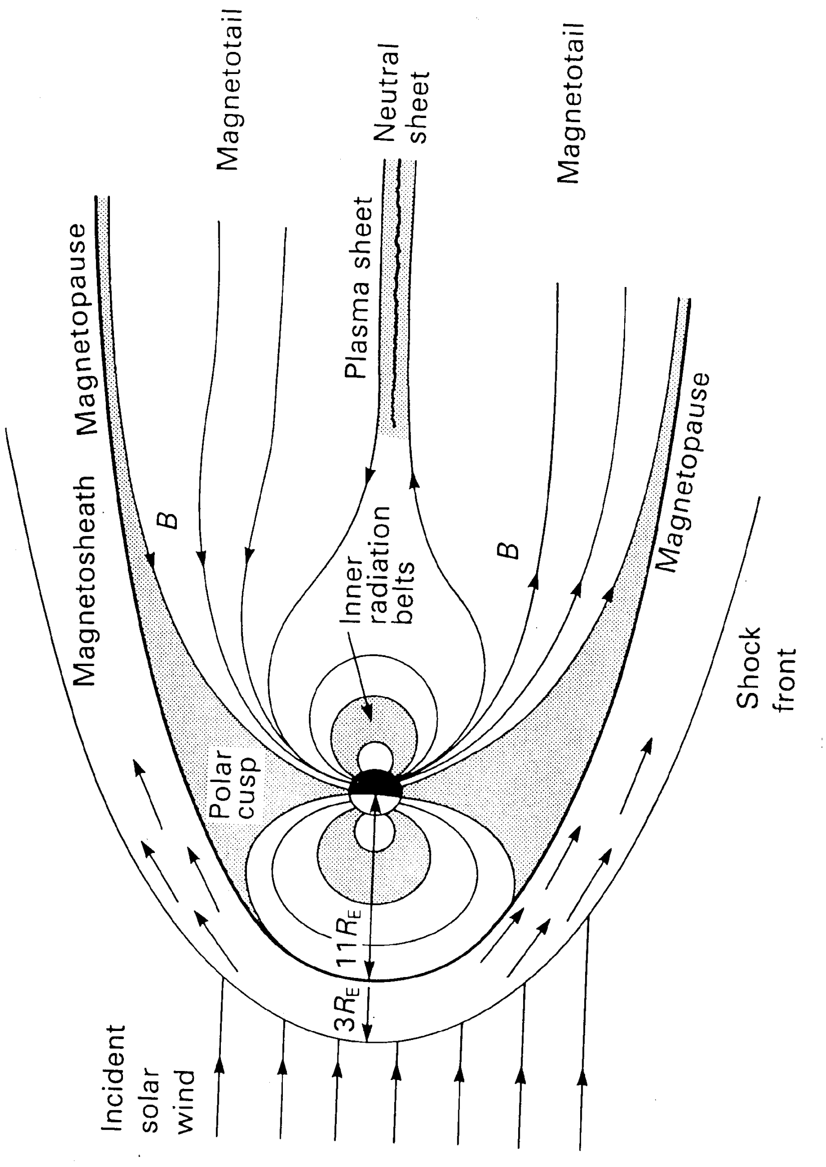

Figure 1.22: Effect of the solar wind on the Magneto–sphere structure. The distance of the Moon is about 60 R_E (R_E=Earth Radius)

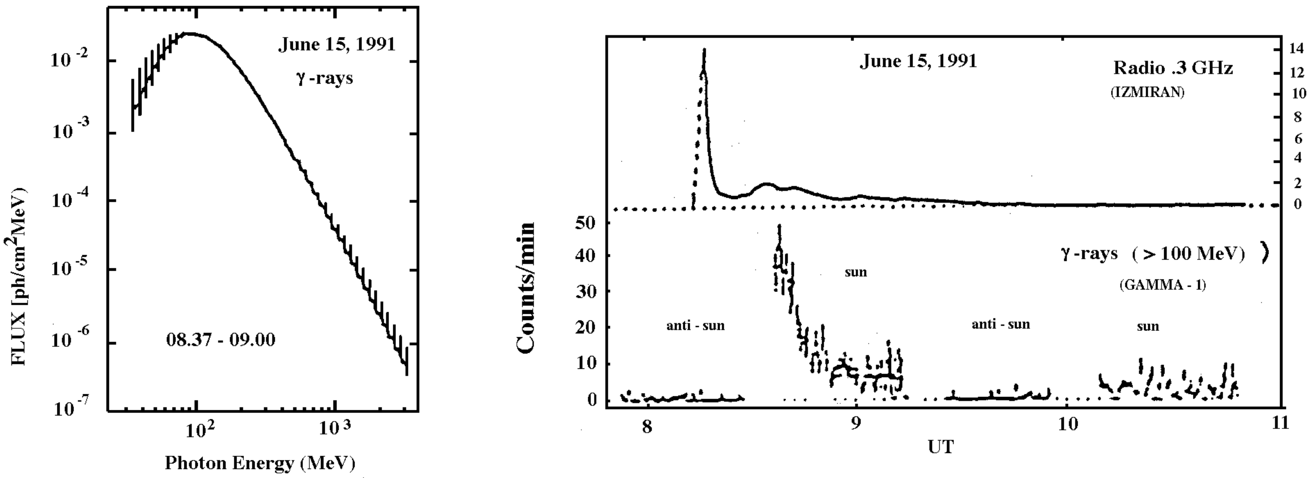

Figure 1.23: The Solar γ–flare on June 15, 1991: the γ–ray energy spectrum observed by the Gamma-1 satellite (left) and the γ–ray time profile (right)

In fig.1.23 the time profile of the gamma flare detected by the Gamma-1 satellite on 1991 June, 15 is shown. In the same figure also the gamma ray spectrum is reported, extending at least up to 5 GeV without any spectral cut-off. During this event, solar neutrons, coming directly from the flare site, have been probably observed at the Alma-Ata standard neutron monitor at 3000 m altitude. Several solar neutron events have been detected by ground-based neutron monitor measuring the nucleon cascade produced at the top of the atmosphere by the incoming high-energy ($> 200\,MeV$) neutron [53]. Neutrons together with X and γ-rays, are produced in the nuclear interactions at the time the particles are accelerated in the solar atmosphere. Thus, their arrival times relative to the X- and γ-rays onset times provide information on their energy, their spectrum at the flare site and hence the proton spectrum. We notice that the 1991 June 4 observation of Akeno Giant Air Shower Array provides evidence also for the possible detection of neutrons with energies above 10 GeV [54]. The opportunity of studying the time evolution of these very large flares could allow to define the different phases of acceleration and trapping of particles. These events can be observed when the sun is high enough in the sky. However, it has to be noticed that not dedicated satellites are operating in this energy range. On the contrary ARGO could provide a daily monitoring of the Sun.

5. Interplanetary perturbations and their evolution during Sun–Earth transit time. Since the ARGO is able to define both the energy and the arrival direction of particles, it is possible to obtain the space distribution of cosmic rays as a function of the en-

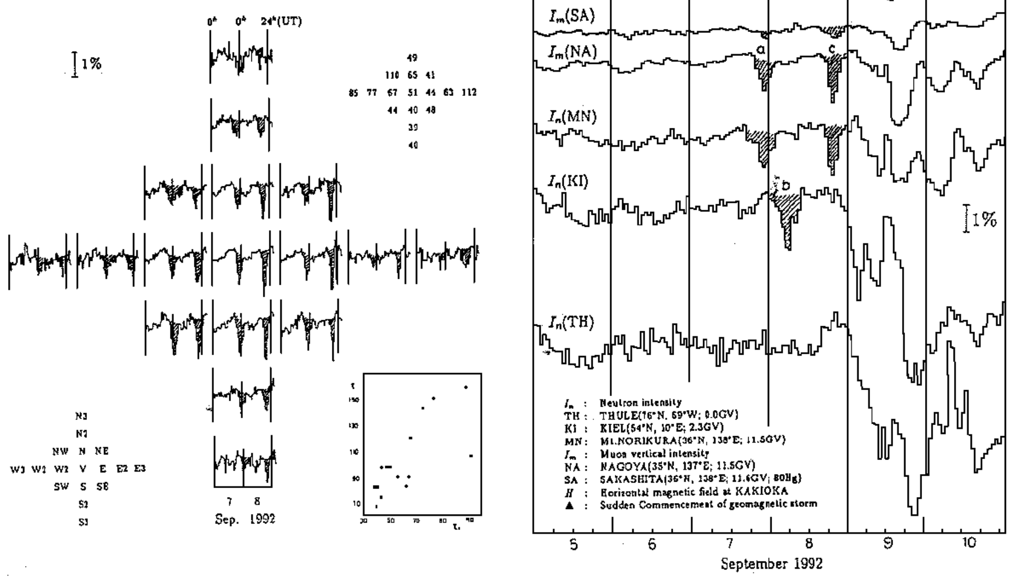

Figure 1.24: Left: The precursory decreases observed with the 17–directional muon telescopes at Nagoya on September 7 and 8, 1992 — Right: Precursory decreases, shaded areas, of the large Forbush decrease on September, 9 1992 as seen at different stations.

ergy outside of the magnetosphere. This particle distribution is affected by individual strong interplanetary perturbations produced by energetic solar activity phenomena (high speed streams, shocks, flare ejecta, magnetic clouds....). The analysis of ARGO data in the 10-100 GeV energy range will allow a detailed study, at the moment not feasible, of the time- space evolution of these perturbations during their transit from the Sun to the Earth orbit. Then it will be possible to improve the monitoring of the interplanetary medium for predicting (one day in advance) the arrival to the earth of those perturbations producing the greatest geomagnetic storms and possible dangerous effects on technical and biological systems [47]. We report in figure 1.24 an example [46] of the effects connected with the traveling of strong interplanetary perturbations through the heliosphere on the cosmic ray intensities registered at different neutron and muon monitors. In particular, several precursory decreases (1.5 % at neutron stations) are present before the main large Forbush decrease (5 %); the precursory decreases observed by the Nagoya muon telescope and allocated according to the geometrical configuration of the telescopes are also shown. The measurements of the ARGO detector could be useful for modelling in more detail the interaction of cosmic ray particles with interplanetary disturbances [55].

6. Long-term time variations of the cosmic ray intensity inside the heliosphere. The heliosphere is embedded in the interstellar medium. The modulation of cosmic rays as a function of position, energy and time in the heliosphere is a complex combination of outward convection by the solar wind, inward diffusion due to the scattering off magnetic field irregularities, adiabatic cooling, gradient, and heliospheric neutral sheet drifts. Hence, three-dimensional aspects of cosmic ray propagation are relevant. It is well known that the cosmic ray flux varies in antiphase with the general solar activity; the upper energy cutoff of this long-term modulation, not yet well determined, should be about 150 GeV. Temporal changes in the solar activity level cause temporal variations in the galactic cosmic ray propagation conditions from the boundary of the heliosphere to the measuring point. The study of cosmic ray intensity, at all energies, combined with solar and interplanetary magnetic field measurements, can provide information on the time-space variation of the global heliospheric structure [48].

7. Cosmic ray anisotropy. The study of daily variations of the cosmic ray intensity, measured by ground-based detectors, can give information on the anisotropy of the cosmic ray distribution in space. Solar and sidereal daily variations are observed in the data records at different energies. Figure 1.25 [49] shows the annual vectors of the three harmonics of the solar diurnal variations at Nagoya, Misato and Sakashita detectors (see Table 2.6) during about 20 years. A dependence of these harmonics on the magnetic polarity state of the heliosphere is emerging. The observed phases shift toward earlier hours during the positive polarity periods (1970's and 1990's) than those during the negative ones (1980's). Due to its high statistics, well defined asymptotic directions and energies of the detected particles, the ARGO supplies major advantages as compared with those of the large shallow and underground detectors. On the other hand, at lower energies (10-50 GeV for primary cosmic rays) ARGO may give also the further possibility to estimate the radial gradients of the cosmic ray density in the heliosphere by measuring the component of the anisotropy perpendicular to ecliptic plane. We notice that, in stationary conditions, an anisotropy perpendicular to the ecliptic plane arises from the vector product $Bx\nabla n$, being B, the interplanetary magnetic field and ∇n, the heliocentric radial density gradient. At highest energies (about 1 TeV), the study of the cosmic ray sidereal time variation can provide information on the cosmic ray anisotropy outside of the heliosphere [50]

8. Power spectrum of cosmic rays. In the past a relation between the power spectrum of cosmic ray flux and that of the magnetic field fluctuations has been proposed in literature [51]. Recently, power spectra analysis have been applied to cosmic ray time variations of underground stations (Matsushiro and Sakashita, see Table 2.6) and air shower experiment at Mt. Norikura (Japan, 2700 m, 12 TeV median energy) [52] with the aim to get information on the fluctuations of the interstellar and interplanetary magnetic field. The power spectra, computed for the three stations, are reported in figure 1.26. A different behaviour of the Sakashita spectrum in comparison with those of Matsushiro and Mt. Norikura (single power-law index and evidence also for sharp spikes of semi-diurnal and tri-diurnal variations) comes out. Hence, the authors conclude that

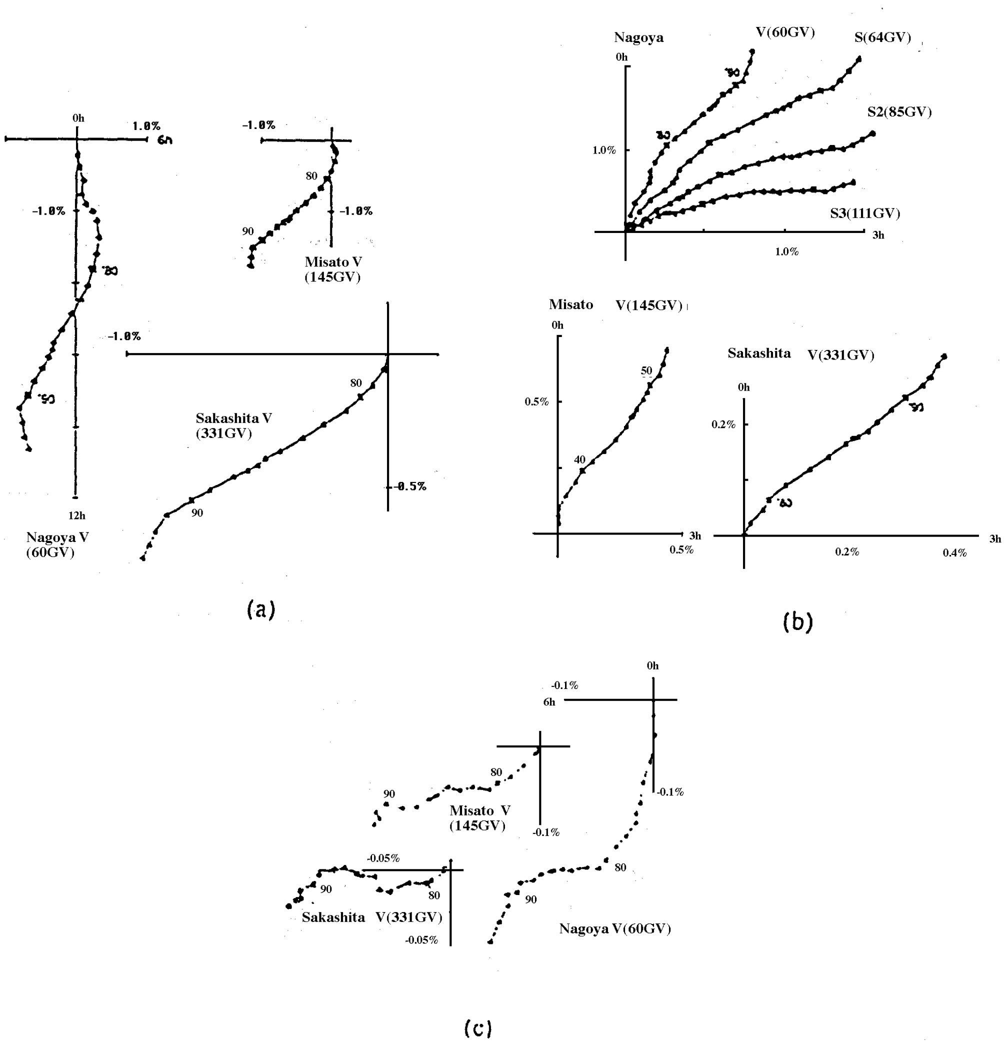

Figure 1.25: Harmonic dials of (a) solar diurnal, (b) semidiurnal and (c) tri–diurnal variation observed by the Nagoya, Misato, and Sakishita experiments. The mean rigidity is shown.

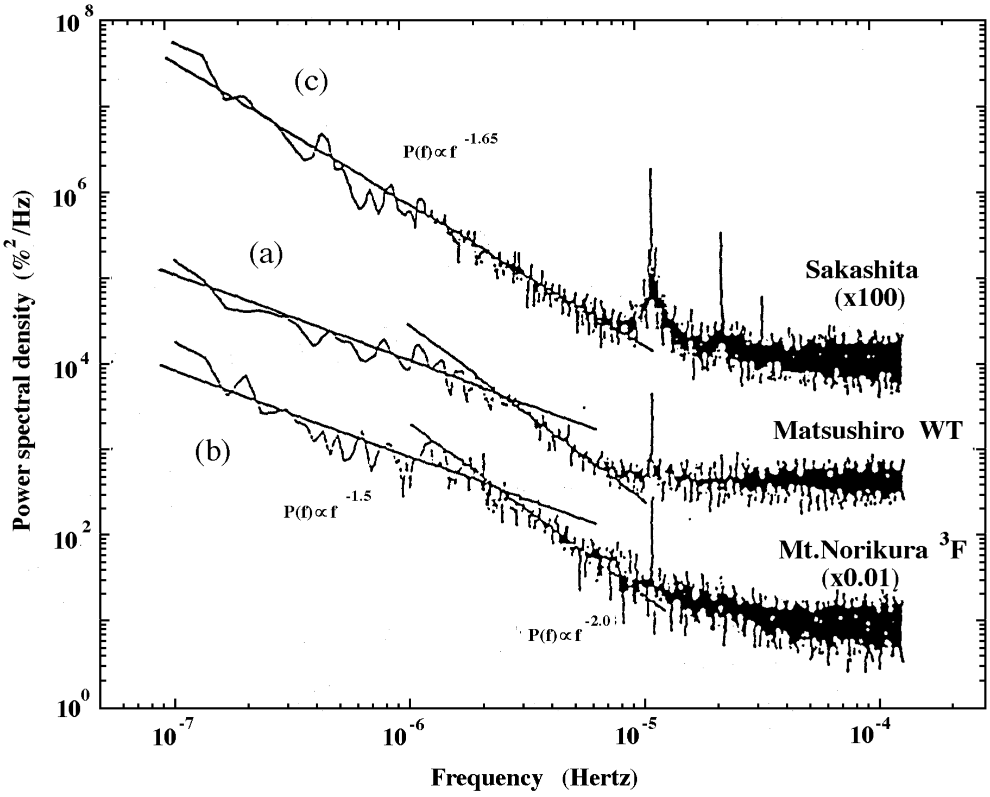

Figure 1.26: The power spectra of time series from (a) the Matsushiro wide angle telescope, (b) the Mt. Norikura air shower experiment and (c) the Sakashita vertical telescope

magnetic field fluctuations in the interstellar medium may be larger than those in the interplanetary space.

Chapter 2

THE EXPERIMENTAL SETUP AND ITS PERFORMANCES

ARGO consists basically of a single layer of RPC's covering $\sim 120 \times 120 m^2$ area, ($\sim 60 \times 60 m^2$ for ARGO-3600) possibly surrounded by a ring of RPC sampling stations to recover edge effects and to increase the effective sensitive area. The whole set-up will be installed in a building which allows to keep the temperature variation at the carpet below a few degrees. In this chapter we present the ARGO performances as obtained by a detailed MonteCarlo simulation of the detector response to atmospheric showers.

2.1 THE RPC SYSTEM

The whole floor of the experimental hall is covered by a mosaic of RPC chambers ($280 \times 112\, cm^2$ each) with 90% sensitive area. Each chamber is equipped with read-out strips of $3.2\, cm$ wide, $56\, cm$ long. The signals of 16 strips are shaped and OR-ed in order to define a 'logic pad' $56 \times 56\, cm^2$. The information from each logic pad consists of

a) a fast-OR signal, to be used for triggering purpose;

b) the number of fired strips in every pad to be used to recover the shower size;

c) the time of the earliest particle hitting the pad, to be used for the reconstruction of the shower direction.

The total number of pads is 48400 (10710 for ARGO–3600). These numbers times 16 provide

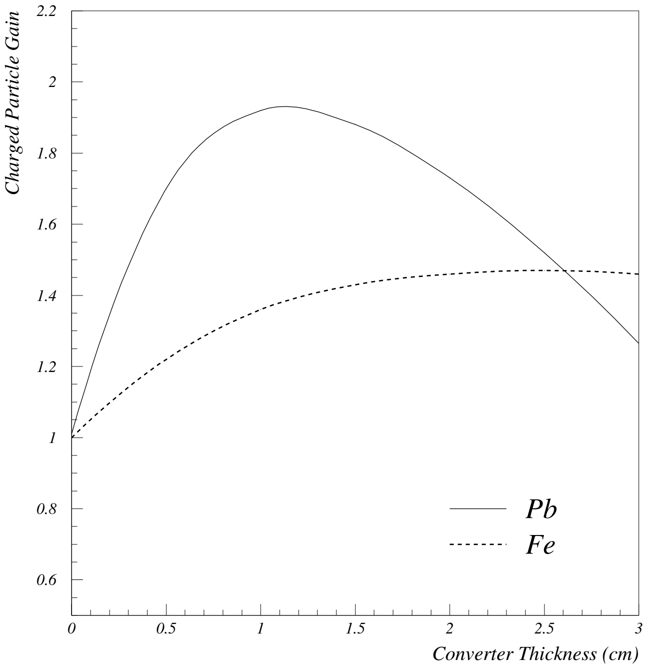

Figure 2.1: The increase of the number of charged particles after lead and iron converters as a function of their thickness ($E_\gamma = 500\,GeV$)

also the number of total strips. The strip information becomes to be important at energies greater than a few TeV, due to the increasing particle density. A schematic view of the experimental layout as well all details of the front-end electronics and read-out system are given in the next Chapter.

A lead converter $0.5\,cm$ thick covers uniformly the RPC plane to convert shower photons. Since in photon induced showers the γ-component is about 7 times more abundant than electrons at 1 MeV threshold energy (~ 3.5 times for distances $< 50\ m$ from the core), the conversion of low energy photons is exploited to increase the number of charged particles and to reduce the time spread of the shower front. The lead layer is put on the strip system by means of a low density foam slab 30 cm thick. A comparison of the effects of using iron or lead converter of different thicknesses is shown in fig.2.1. We have chosen $0.5\,cm$ of lead as a compromise between efficiency and cost. The increase of the effective thickness with zenith angle allows to partially compensate the increase of the atmospheric depth, so the results on trigger efficiency obtained at 0^o and 35^o zenith angles do not scatter more than 20% from that relative at a zenith angle of 20^0.

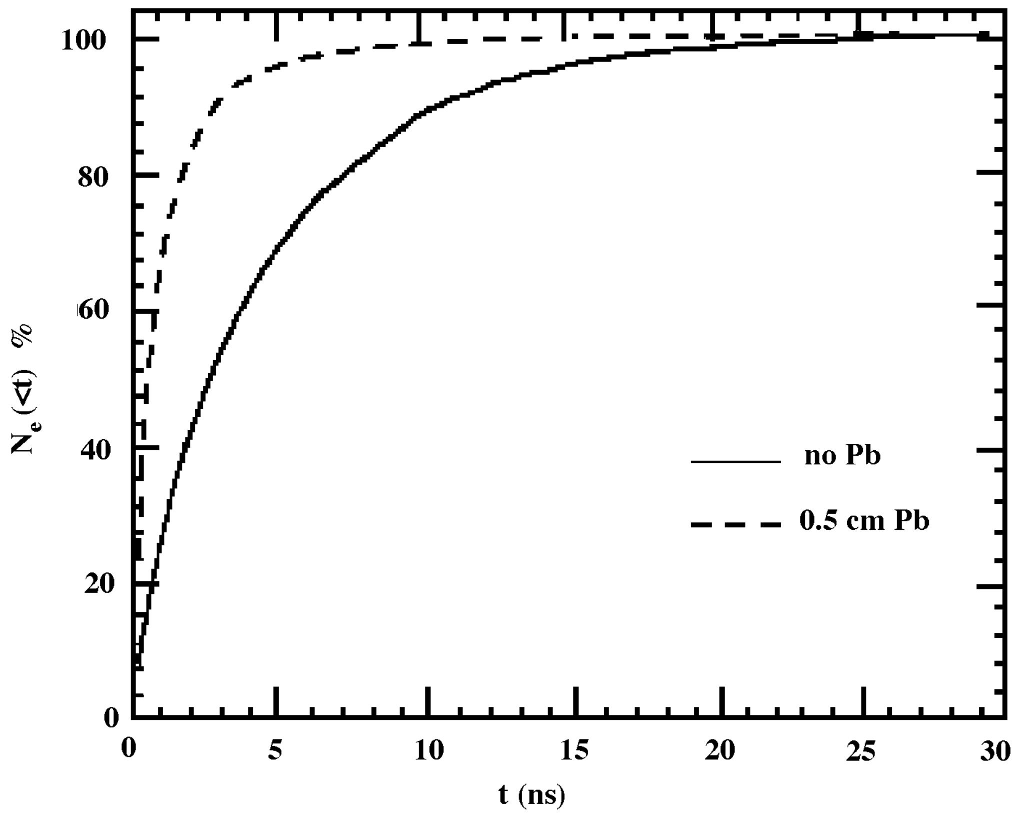

Figure 2.2: Integral time distributions of electrons at distances 20-30 m from the shower core with and without 0.5 cm of Pb converter ($E_\gamma = 500\ GeV$).

The effect of the converter on the time fluctuation of the shower electrons is well evidenced in fig.2.2 where the integral time distributions of electrons at distances $20 \div 30\ m$ from the shower core with and without $0.5\, cm$ of Pb converter are compared: the spread in the arrival time delay is clearly reduced.

2.2 DETECTOR PERFORMANCES

The main parameters which characterize the response of the detector to incident showers are the trigger efficiency vs. primary energy for both gamma and proton induced showers, the angular resolution, the γ/h separation and the energy resolution. These features have been studied by means of a MonteCarlo simulation. Three different shower propagation codes have been used: the EPAS code [59] to develop the electromagnetic cascade in atmosphere, the HADRAS code [60] to describe the cascade induced by primary hadrons and the GEANT code [61] to propagate electrons and photons at the sampling level through the converter.

Primary particles (photons and protons) are injected at 10^0 to 35^0 zenith angles from the top of the atmosphere, and secondaries (electrons, photons, muons and hadrons) propagated up to a vertical depth of $606\, g/cm^2$. Secondaries with energy $> 1\, MeV$ are recorded at the sampling level before and after the converter. A total of about 10^6 showers with energy of 5 to $4 \times 10^5\, GeV$ have been followed and used to simulate 5×10^6 events with core distributed around the detector. The detailed structure of the RPCs carpet (see chapter 3) has been taken into account. An average RPCs efficiency of 95% has been assumed. The arrival times have been smeared out by taking into account the transit time in the strip (delay=4 ns/m), the time resolution of the detector ($\sigma_\tau = 1ns$) and the time resolution of the digitizing electronics ($\sigma_{e1} = 1ns$).

2.2.1 Photon primaries

The pseudo-experimental data relative to γ-induced showers have been processed throughout different steps to determine the effective area and the accuracy in reconstructing the shower direction.

1) Effective area

The effective area is determined by the number of charged particles > 1 MeV (the mean energy required to an electron to penetrate in the active volume of the RPC) needed to trigger the array. It has been calculated by a standard procedure, that is simulating N showers uniformly distributed over a large sampling area A_s including the detector, and selecting those which satisfy the trigger conditions. Two types of events have been considered:
- internal events, with the core reconstructed inside an internal area A_g enclosed in the active surface of the RPC carpet ($A_g = 10^4\, m^2$ for ARGO, $A_g = 2500\, m^2$ for ARGO-3600);
- external events with core outside A_g.

For internal events the effective area is defined as

$$A_{eff} = \frac{n_g}{N_g} \cdot A_g \tag{2.1}$$

where N_g is the total number of events with core hitting the internal area A_g and n_g is the number of the events satisfying the trigger conditions.

These events allow for an accurate reconstruction of the shower direction with an angular resolution depending on the number of fired pads (see point 3). Thus, these events are essentially addressed to the physics sector including the γ-astronomy and the detection of the shadow of the Moon and Sun in charged cosmic rays.

For external events the effective area is defined as

$$A_{eff} = \frac{n}{N} A_s \tag{2.2}$$

where n is the number of events satisfying the trigger conditions independently of the position of the shower core. This figure is appropriate to the events for which the reconstruction of the impact point of the shower core inside the fiducial area A_g is not possible. This category includes all the events with core outside A_g or low multiplicity events with a number of fired pads (typically less than 20) insufficient to permit the identification of the shower core.

Due to the low rate of each pad – about 150 Hz/pad – a first level trigger requiring only a few fired pads can be realized. Two different trigger conditions have been considered according to the dimension of the RPCs carpet:

ARGO-3600: the first level trigger is realized by requiring at least 6 pads in a time window of $250\,ns$. This permits to accept showers up to 50^0 zenith angle corresponding to an angular acceptance of about $2.2\,sr$. The expected trigger rate is $\approx 5\,KHz$ with an average number of ≈ 20 fired pads. Spurious triggers due to time coincidence of hits not correlated to the same shower are expected to be less than 10%.

ARGO: a first level trigger equivalent to the previous one should require a time window of 450 ns. However, in this case, a spurious trigger rate of $\approx 10\,kHz$ (a substantial fraction of the total trigger rate) is expected. These data could be processed to reject spurious triggers by requiring that the space–time pattern of the detected hits is consistent with the expected time profile of the shower front - for instance a plan "disk" 10 ns thick -. Alternatively, the spurious trigger rate can be substantially reduced by imposing some constraint to the topology of these events. A possible solution we have simulated is the following one:

a) the whole active area is subdivided in $10 \times 10 m^2$ logic subunits. In such a way a grid of 144 units is obtained.

b) the trigger condition requires at least a threefold coincidence of these logic subunits in a time window of 450 ns, each logic subunit being set on by at least two fired pads in a time window of 60 ns.

c) this scheme is repeated for three other independent grids obtained by shifting the previous one of 5 meters in the x direction, 5 meters in the y direction and 5 meters in both directions. In such a way 4 similar and independent overlapping grids are defined and put in OR to realize the final trigger.

The technical realization of the trigger system is presented in chapter 3.

2) Shower core reconstruction

The reconstruction of the shower core for internal events, namely the events with core hitting a fiducial area of $100 \times 100\ m^2$ ($50 \times 50\ m^2$ for ARGO-3600) included in the whole carpet surface is performed in different ways according to the number of fired pads. A standard procedure by fitting the lateral distribution has been followed for events with > 50 pads, whose core location is obtained with a precision $\sigma_x = \sigma_y \leq 2\,m$. Events with a number 20 to 50 pads have been analyzed by imposing that the time profile of the shower front could be approximated within 40 m from the core by a conical shape surface with a conic angle of 22 $mrad$ see fig.2.3. In this case the core location for internal events is obtained with an indetermination of about 7 meters or less according to the number of pads.

3) Angular resolution

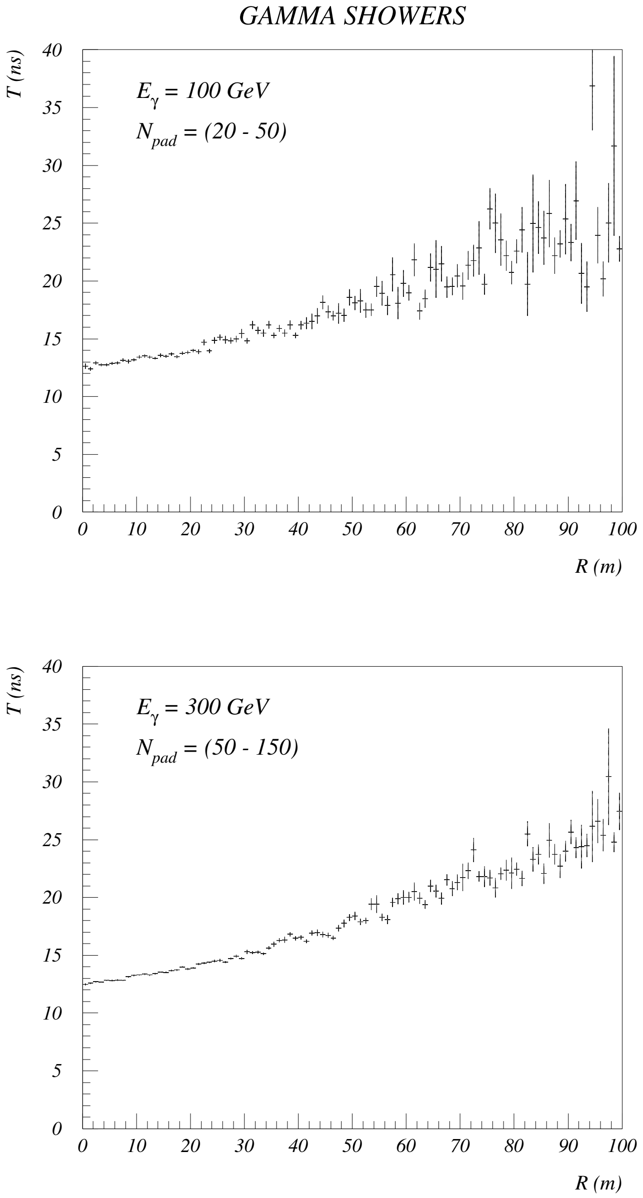

Figure 2.3: Time profile of the shower front as a function of the core distance in photon showers of 100 and 300 GeV energy, for two different number of pad selections.

To get the pointing accuracy two different procedures have been implemented for internal or external events separately:

a) internal events, in which the core is clearly reconstructed inside the detector, are analyzed following an iterative procedure which allows for the rejection of spurious times due either to accidental hits (on average 4 for ARGO, 1 for ARGO-3600) or to extreme time fluctuations of shower particles. This procedure consists of the following steps:

i): determination of the core position and plane fit to hits at core distance $< 40\ m$

ii): rejection of out-lying times by means of a 4σ cut ($\sim 10\ ns$) to the distribution of time residuals $(t_{fit} - t_{exp})$ and cone-like fit by fitting a conical shape to the survived times

iii): the last step is repeated applying a 3σ cut

iv): the distribution of residuals is symmetrized by rejecting negative residuals greater than the largest positive residual,and a weighted cone-like fit is applied with $w(r) = 1/\sigma^2(\Delta r)$,being $\sigma^2(\Delta r)$ the r.m.s. of the residuals at the distance interval Δr ($\Delta r = 0-10, 10-20, \ldots m$)

This procedure is quite fast because it makes use only of analytic formulae. The distribution of residuals for a large sample of events with $N_{pad} > 20$ is shown in fig. 2.4. The angular resolution $\psi(70)$ as a function of the number of pads is shown in fig.2.5 It is practically independent of the primary energy. Here $\psi(70)$ represents the opening angle around the source direction containing 70% of signal showers. No systematic inaccuracy has been taken into account.

b) the space-time pattern of external events has been fitted to a plane and the same iterative procedure has been adopted. The pointing accuracy for events with more than 10 fired pads is shown in fig.2.6 as a function of the energy. ARGO and ARGO–3600 differ because no cut on the distance from the shower core is applied. The mean angular resolution $\psi(70)$ for events with a number of fired pads ≤ 10 — averaged over a $E^{-2.5}$ spectrum — is found to be $\sim 4^o$ for ARGO and $\sim 5^o$ for ARGO–3600.

Summarizing, all events can be classified according to the number of fired pads and whether the core has been reconstructed inside the detector area, see Table 2.1, where LMT, HMT = low, high multiplicity events and LR = low angular resolution. The HMT/LR events are high multiplicity events with core located outside the fiducial area A_g.

The effective areas for both cases LMT and HMT as a function of the energy and number of fired pads are given in figs.2.7 to 2.10. These curves represent only a few cases, however enough to show that selecting events with an appropriate number of pads is possible to investigate different energy regions. In evaluating the ARGO sensitivity to face physics items requiring good angular resolution as gamma astronomy and the measurement of the Moon or Sun shadow, only HMT(> 20) events have been considered. The physics items for which even a poor angular resolution is sufficient (GRBs and heliosphere physics) have been studied by using all the recorded events with ≥ 6 fired pads.

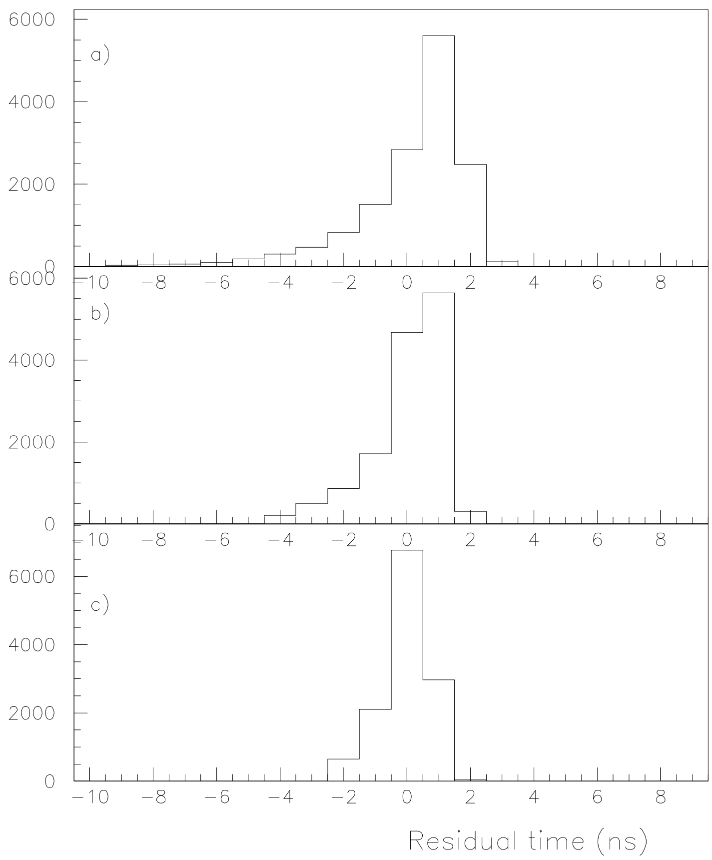

Figure 2.4: Distribution of time residuals ($t_{fit} - t_{exp}$) after the step i) – top, the step ii) – middle, and after the step iv) – bottom (see text).

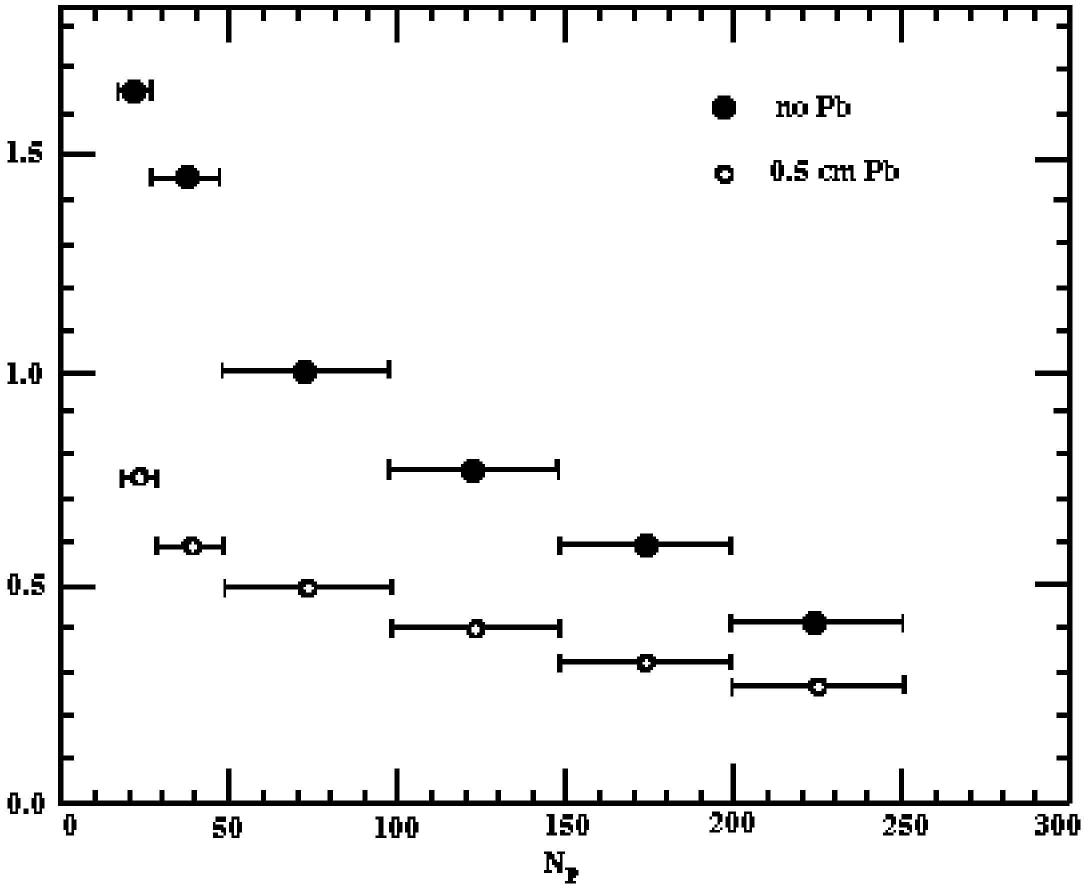

Figure 2.5: The opening angle $\psi(70)$ (see text) as a function of the number of pads for *internal events*.

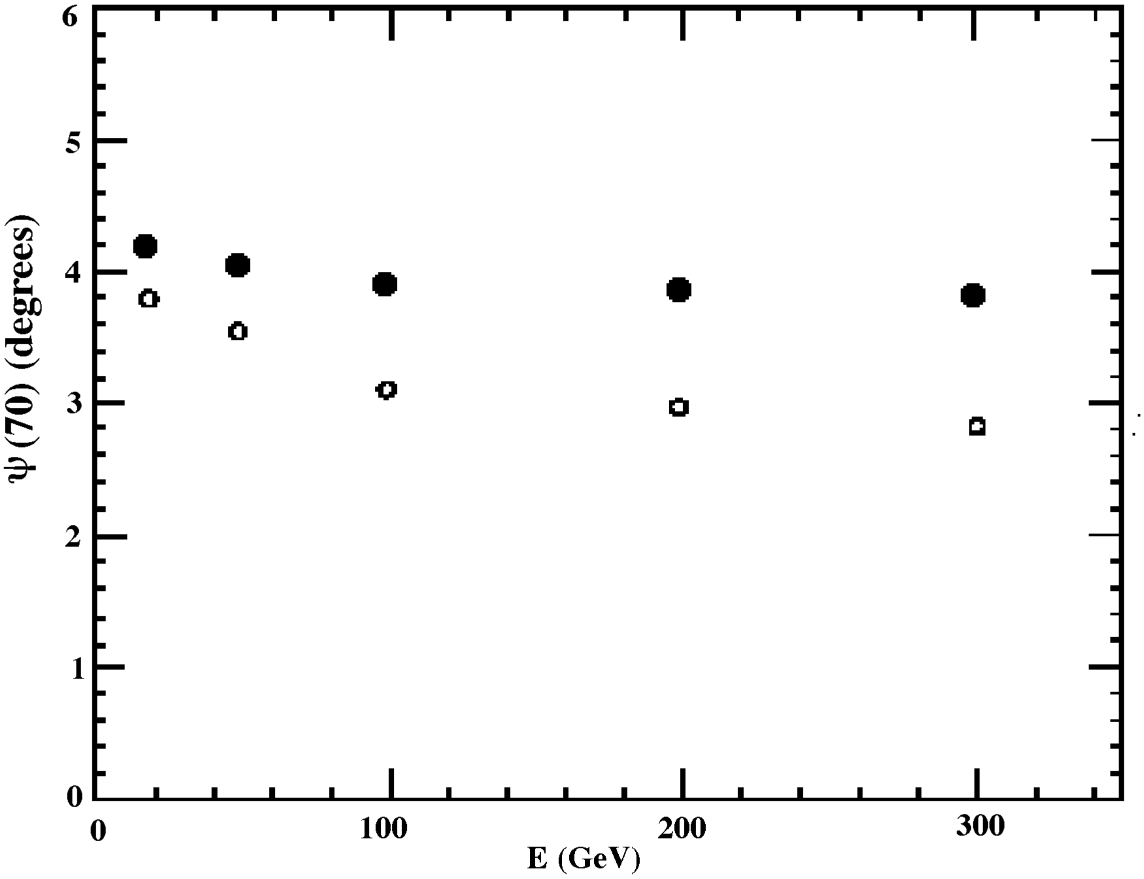

Figure 2.6: The opening angle $\psi(70)$ (see text) as a function of the energy for *external events*. Diamonds : ARGO–3600; circles : ARGO.

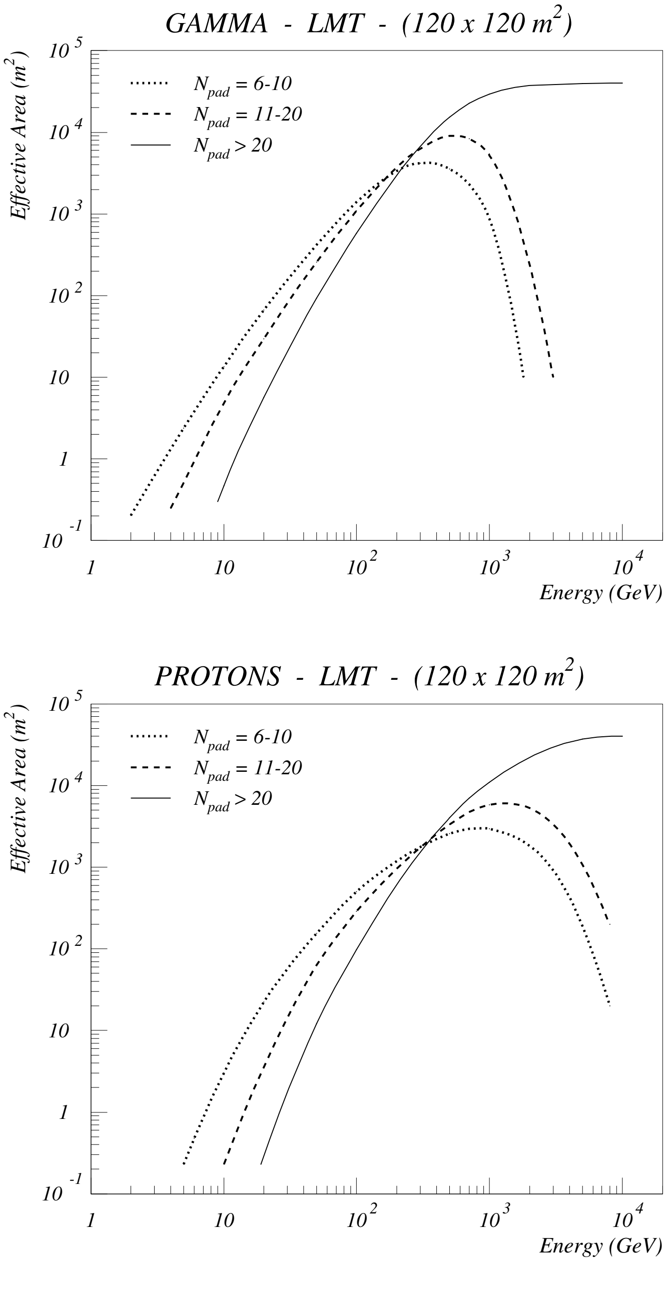

Figure 2.7: Effective area of ARGO for some LMT trigger selections for gamma and proton primaries

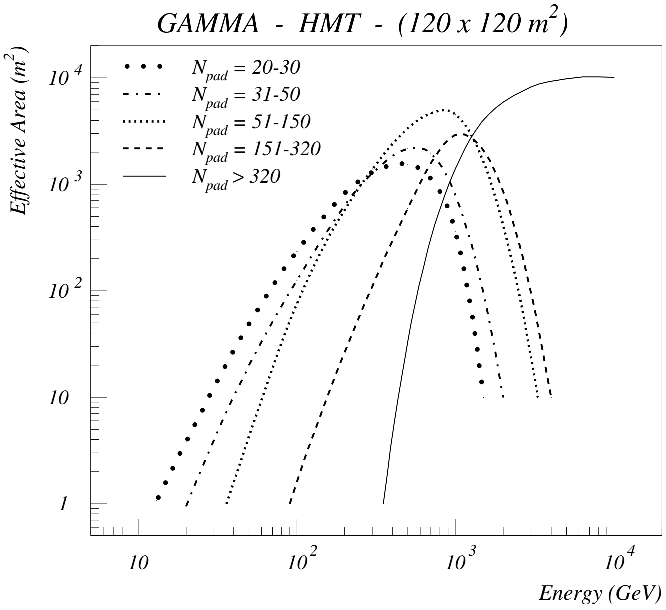

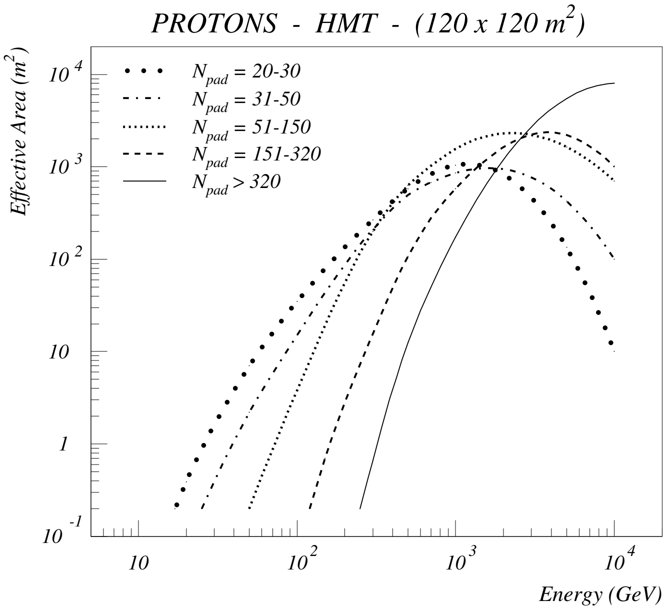

Figure 2.8: Effective area of ARGO for some HMT trigger selections for gamma and proton primaries

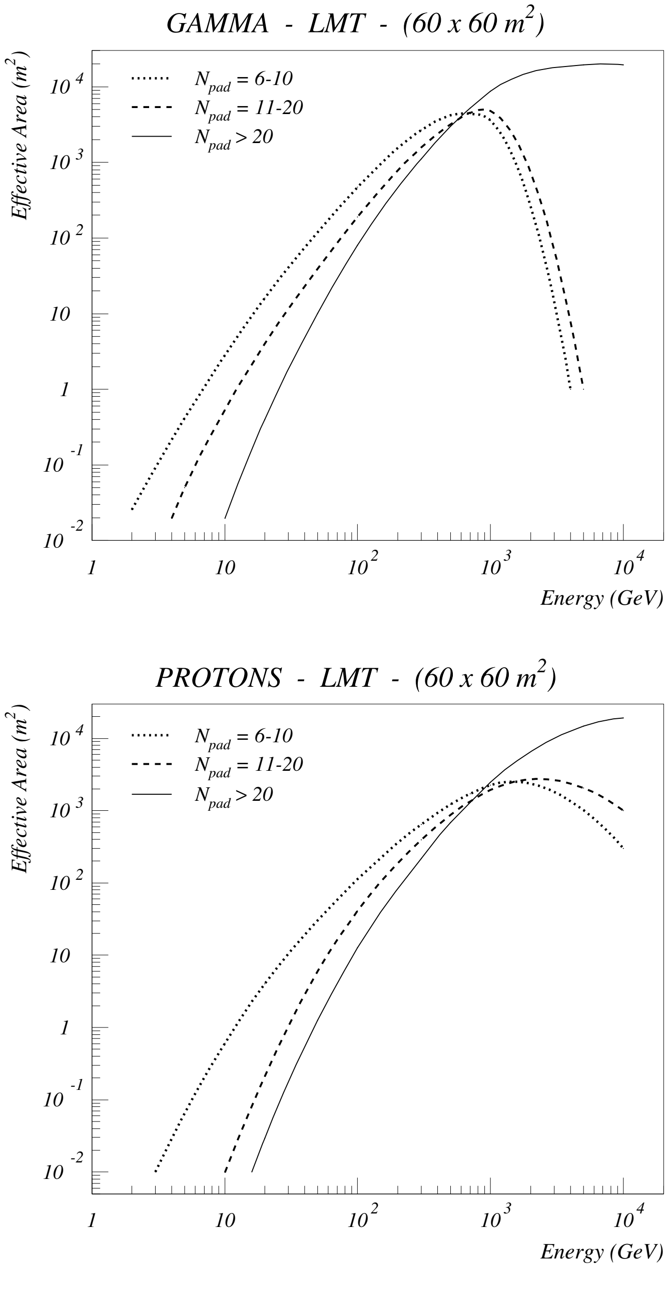

Figure 2.9: Effective area of ARGO–3600 for some LMT trigger selections for gamma and proton primaries

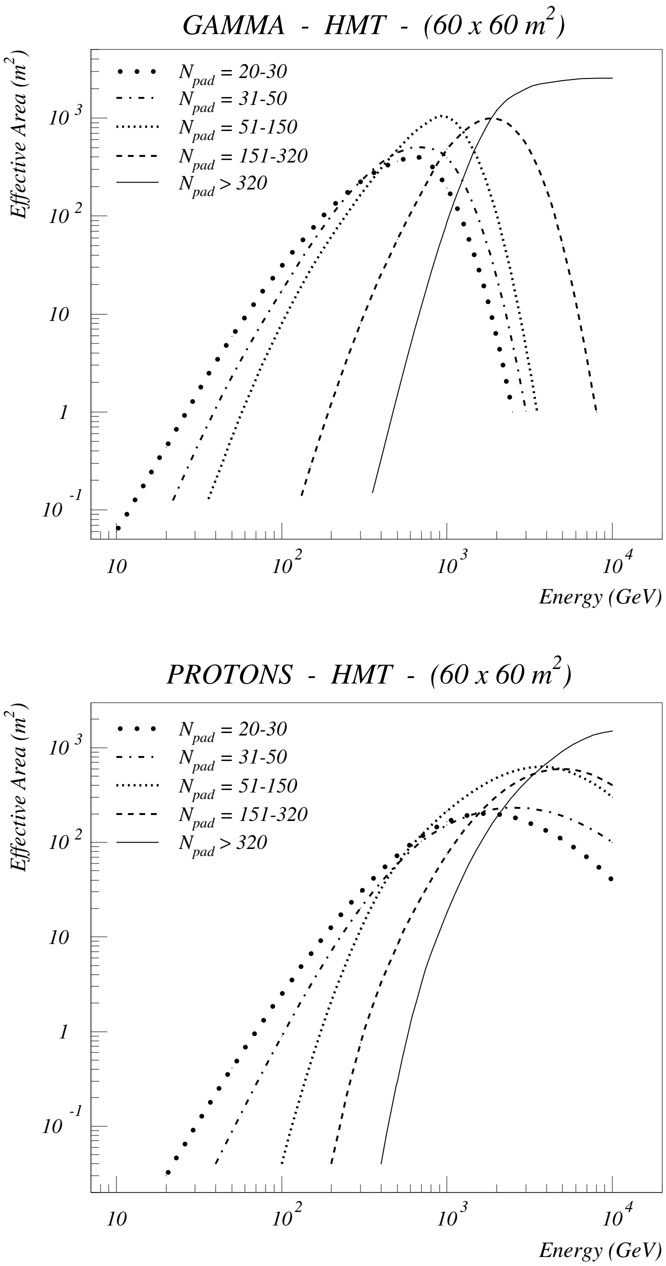

Figure 2.10: Effective area of ARGO–3600 for some HMT trigger selections for gamma and proton primaries

2.2.2 Proton primaries

A similar study to determine the trigger efficiency for proton induced air showers has been carried out. Results are shown in figs. 2.7 to 2.10. Under the same trigger conditions the angular resolution is found quite similar to the one obtained for the photon induced showers.

2.2.3 γ/p Discrimination

An effective suppression of the background events induced by the proton-nuclear component of the primary cosmic-ray radiation is of crucial importance for gamma-astronomy and GRB physics. A first γ/p discrimination is obtained by the hardware trigger requirements; further discrimination may be achieved by an off-line analysis looking at differences in the event pattern.

Hardware Discrimination
A comparison of the effective areas for both LMT and HMT selections (see fig. 2.7 to 2.10) shows that the trigger efficiency for low energy protons is much lower than that for gamma rays at energies below 500 GeV. This allows to achieve an essential rejection of background events already at the hardware level,increasing the sensitivity S in detecting a gamma ray signal above the background. In fact S depends on the effective areas as $S \sim \sqrt{A^{\gamma}_{eff}} \cdot \sqrt{A^{\gamma}_{eff}/A^{p}_{eff}} = \sqrt{A^{\gamma}_{eff}} \cdot R_{\gamma}$. As an example, we report in Table 2.2 the figure-of-merit R_{γ} for HMT(> 20), both for ARGO (first column) and ARGO-3600 (second column), at different energies As obtained by our simulations — and pointed out in [7] — R_{γ} is grater then the unity because of a reduced electron/photon density in proton induced showers as compared to the density in photon induced showers of the same energy.Thus the requirement of having 20 pads in a 2500 m^2 area is more effective than the same requirement applied to an area as large as 10^4 m^2. On the other hand, this effect is compensated because ARGO samples showers on larger effective areas respect to ARGO-3600, so that we obtain for HMT(> 20)

$$\frac{(\sqrt{A^{\gamma}_{eff}} \cdot R_{\gamma})_{ARGO}}{(\sqrt{A^{\gamma}_{eff}} \cdot R_{\gamma})_{ARGO-3600}} = 2 \tag{2.3}$$

independently of the energy. Thus, ARGO-3600 loses a factor of 2 in sensitivity as compared to ARGO at a median energy of about 150 GeV. A similar calculation for HMT(> 150)-median energy about 900 GeV- provides a factor of about 2.3. We conclude this discussion pointing out that the large value of R_{γ} at low energies balances the small value of the effective area A^{γ}_{eff}, so that also with selective triggers as HMT($20-50$), addressed to the detection of low energy photons,a large sensitivity is achieved. Detailed calculations shown in the next section confirm this point.

Software Discrimination.
The difference in density of the electromagnetic component could be further used to improve the selection between air showers induced by photons and those induced by protons. In fact the trigger selection is an 'integral constraint' and details of the topology are not exploited.

Some results of preliminary calculations are presented in the following. Fig.2.11 shows the lateral distribution of charged particles after the lead converter. The spread in proton showers is larger than that in photon showers, as expected because of π^o production by low energy protons. This effect could be exploited once the core location has been identified. As a preliminary investigation, we have started a study to identify potential distinguishing features mainly related to topological differences irrespective of the core position. So we have studied a weighted sample of photon and proton events with 50-100 pads, distributed between 100 and 500 GeV. After projecting the hit position on the tangential plane to the shower front (uncertainties in the direction reconstruction as well as the curvature of the shower front are not relevant), the distribution of the distances d_{ij} between every pair of hits for each event has been obtained. The scatter plot of fig.2.12 shows the correlation between the average d and the width σ_d of these distributions for photon and proton induced showers. A selection $3000 < d < 5000,\ 1100 < \sigma_d < 1600$ provides a Q-factor $F\gamma/\sqrt{F_p} = 1.06$, being F_γ and F_p the fraction of events survived to the cuts. This factor determines the improvement to the signal-to-noise ratio after the software analysis. We are extending this study to the other event selections. Moreover, other parameters as the azimuthal and radial distributions around the reconstructed core position will be included in this analysis. As a consequence of these preliminary results a conservative factor $Q = 1.05$ has been applied in evaluating the sensitivity to a point source by means of the HMT(> 50) selection. An other possible method to distinguish between gamma-initiated and hadronic showers can be given by the difference of their arrival time profile. Detailed calculations on this point are in progress.

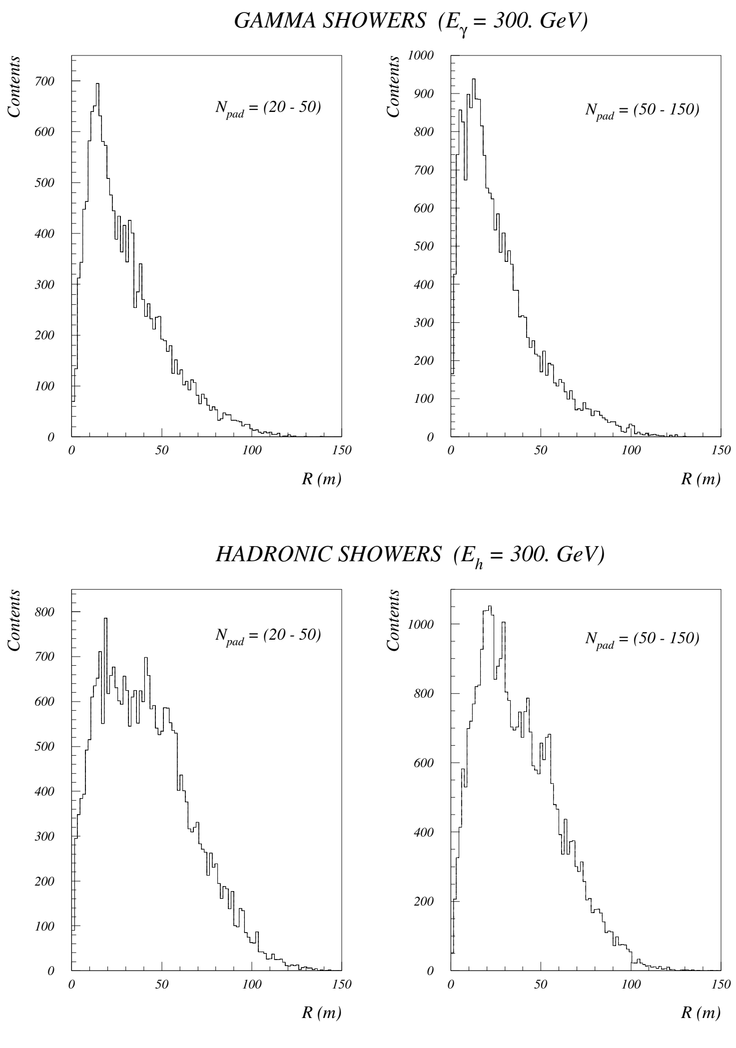

Figure 2.11: The lateral distribution of charged particles after the converter for photon and proton induced air showers of 300 GeV energy.

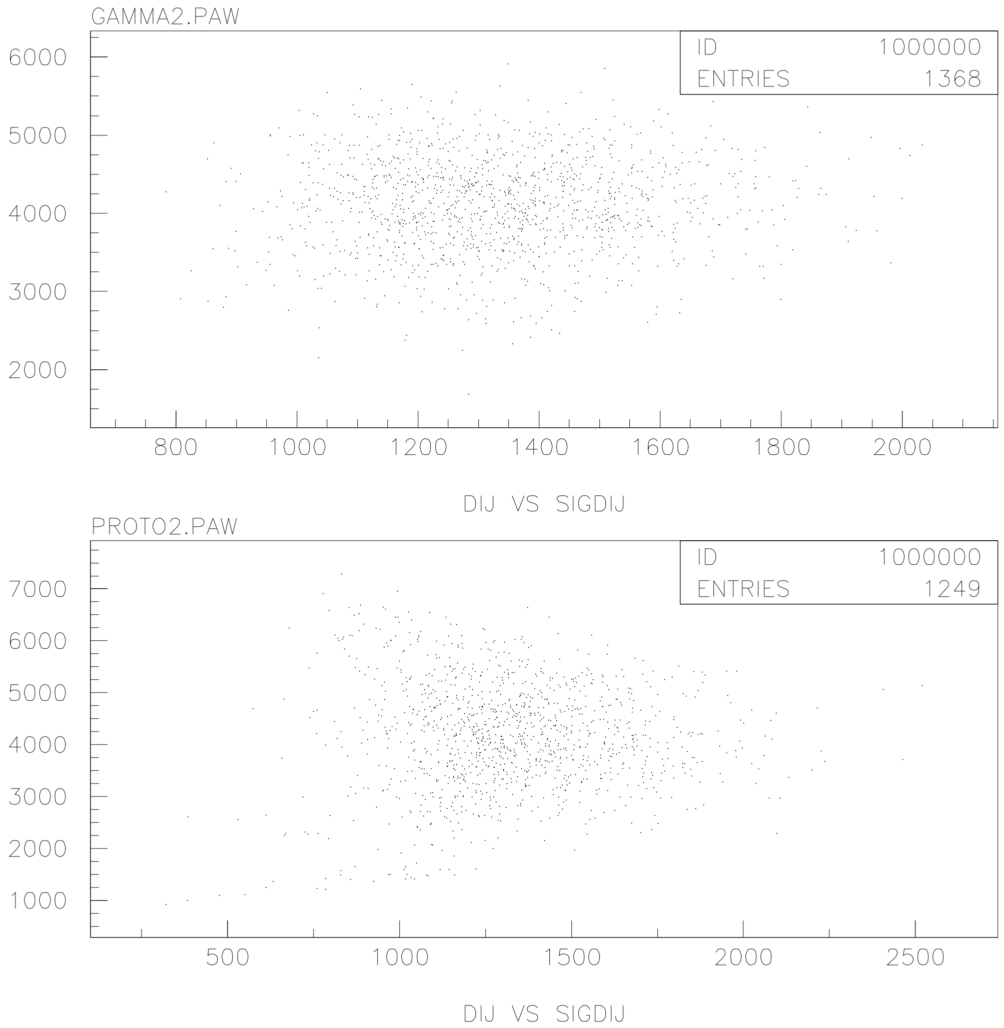

Figure 2.12: Correlation between d and σ_d for photon and proton induced air showers in the energy range $100 \div 500\,GeV$ (see text). Here $DIJ = 2 \cdot d$ and $SIGDIJ = 2 \cdot \sigma_d$. Events with $50 \div 100$ pads sampled by ARGO–3600 have been considered.

2.3 ARGO SENSITIVITY AND PHYSICS PERFORMANCES

GAMMA RAY ASTRONOMY

The ability of ARGO to detect photons from candidate sources depends on the intensity, spectrum and angular extension of the source itself. The sensitivity S is obtained by comparing the total number of photons N_γ expected from the source within the solid angle $\Delta\Omega$ centered on the source itself and the expected number of cosmic-ray background events N_B in the same angular bin. The significance S of the signal as a function of the selected number of pads ΔN_p can be calculated according to the following formula

$$S(\Delta N_p) = \frac{N_\gamma(\Delta N_p)}{\sqrt{N_B(\Delta N_p)}} = \frac{\int_{E_1} A^\gamma_{eff}(E) J_\gamma(E) dE \cdot \epsilon_\gamma(\Delta\Omega) \cdot T(d) \cdot f(\delta)}{\sqrt{\int_{E_1'} A^p_{eff}(E) J_B(E) dE \cdot \Delta\Omega(\Delta N_p) \cdot T(d) \cdot f(\delta)}} \cdot Q$$

where $A^\gamma_{eff}(E), A^p_{eff}(E)$ = the effective areas corresponding to the selected number of pads, $J_\gamma(E), J_B(E)$ = the photon and background energy spectrum, $\epsilon_\gamma(\Delta\Omega) = 0.70$ = the fraction of γ-showers falling within the optimal solid angle bin $\Delta\Omega$, $\Delta\Omega = 2\pi(1 - cos\theta)$ = the solid angle centered on the source with an angular radius θ chosen in order to maximize the sensitivity S. The choice of θ depends on the number of selected pads and on the angular extension of the source, $T(d)$ = the effective time of data taking in days, $f(\delta)$ = the time of source observation per day at angles less than 40^o, depending on the source declination, Q = the Q-factor for software γ/h discrimination.

The following considerations and assumptions have been of guidance in calculating S

a) the choice of ΔN_p allows to select the energy region more appropriate to the observation of a given candidate source. For instance, $\Delta N = 20 \div 50$ pads correspond to an energy region with a median energy in the range $\simeq 100 - 200\,GeV$ (slightly depending on the source spectrum);

b) the background spectrum is essentially determined by proton and helium primaries, the helium nuclei contributing less than 15% up to at least $10\,TeV$. Proton and helium fluxes have been calculated according to spectra quoted in ref. [62]

c) the angular bin θ around the source is given by $\psi(70)$ for point sources and by $\sqrt{(\psi(70))^2 + (\Delta\theta)^2}$ for sources with an angular extension $\Delta\theta$, as some SNRs and molecular clouds;

d) $f(\delta)$ has been calculated for every source in the declination band $60 < \delta < 0$. It varies from $6 \div 7$ hours for 'vertical' sources ($|\delta - \lambda| \leq 10^0$) to $2 \div 3$ hours for sources observed at angle $> 30^o$. Here $\lambda = 30^0$ is the latitude of Yanbajing. Sources with $|\delta - \lambda| > 30^0$ are not included in the present analysis and appropriate calculations will be presented in a separate document;

e) according to the results of Sect. 2.2.3 a conservative estimate of $Q = 1.05$ has been taken.

Results obtained applying these criteria can be summarized as follows

GALACTIC SOURCES

a) CRAB NEBULA. The unpulsed flux is observed by means of the HMT(ΔN_p) selection. In Table 2.3 and 2.4 are reported the time of observation needed to get a 5σ signal with ARGO and ARGO-3600 respectively. In doing these calculations the new Whipple spectrum $J_\gamma(E) = 1.47 \cdot 10^{-11}(E/TeV)^{-2.69}\ cm^{-2}s^{-1}TeV^{-1}$ has been used. The old Whipple spectrum should require a time a factor ~ 4 shorter.

In these tables E_m is the median energy corresponding to the number of selected pads, E_{th} the threshold energy (the energy corresponding to the detection of 15% of the signal) for the integral measurements. The number of photons N_γ is quoted before any software cut applied to improve the signal/background ratio. Systematics pointing errors have not been taken into account.

The energy spectrum of photons detected from Crab by ARGO is shown in fig.2.13. The energy spectrum sampled by ARGO-3600 is quite similar to the one detected by ARGO. It results from table 2.4 that ARGO is able to detect the Crab flux in quite short times. For instance, a 3.5σ signal would be detected every two weeks by ARGO-3600, every four days by ARGO. Therefore, the Crab will represent the monitor beam suited to develop the experimental technique appropriate to the detection of small size showers.

The ARGO sensitivity for a 5σ detection in one yr data taking corresponds to a differential flux at $100\,GeV$ of $\sim 7 \cdot 10^{-13} photons/cm^2\ s\,GeV$. This figure, obviously, depends on the energy spectrum but can be used as a guide to define the discovery potential of ARGO. The corresponding flux for ARGO-3600 is $\sim 1.7 \cdot 10^{-12} photons/cm^2\ s\,GeV$.

The Crab could be observed at $100\,GeV$ median energy by using the selection LMT(11-20). In this case we get $S = 15/\psi(70)(degrees) \simeq 4.5\sigma$ in 1 yr of data taking. The spectrum of detected photons is shown in fig.2.14. ARGO would be the first air shower detector to meet the satellite energy region below $100\,GeV$.

b) PSR B1951+32. The pulsed spectrum of this source detected by EGRET does not exhibit cut-off up to $20\,GeV$. Assuming that it extends at least up to $100\,GeV$ the source should marginally detectable at a level of 4.3σ in 1 yr of data taking. In doing this measurement the appropriate selection is HMT(20-50). A time of observation of 6 hours per day has been assumed, being the declination of the source close to the latitude of Yanbajing. Due to the flat spectrum, a large contribution is expected if the spectrum extends beyond $100\,GeV$. The application of a phase analysis could increase the strength of the signal up to 10σ or more. To the extent that these assumptions are correct, even ARGO-3600 should be able to detect the pulsed spectrum by means a combined dc-ac analysis.

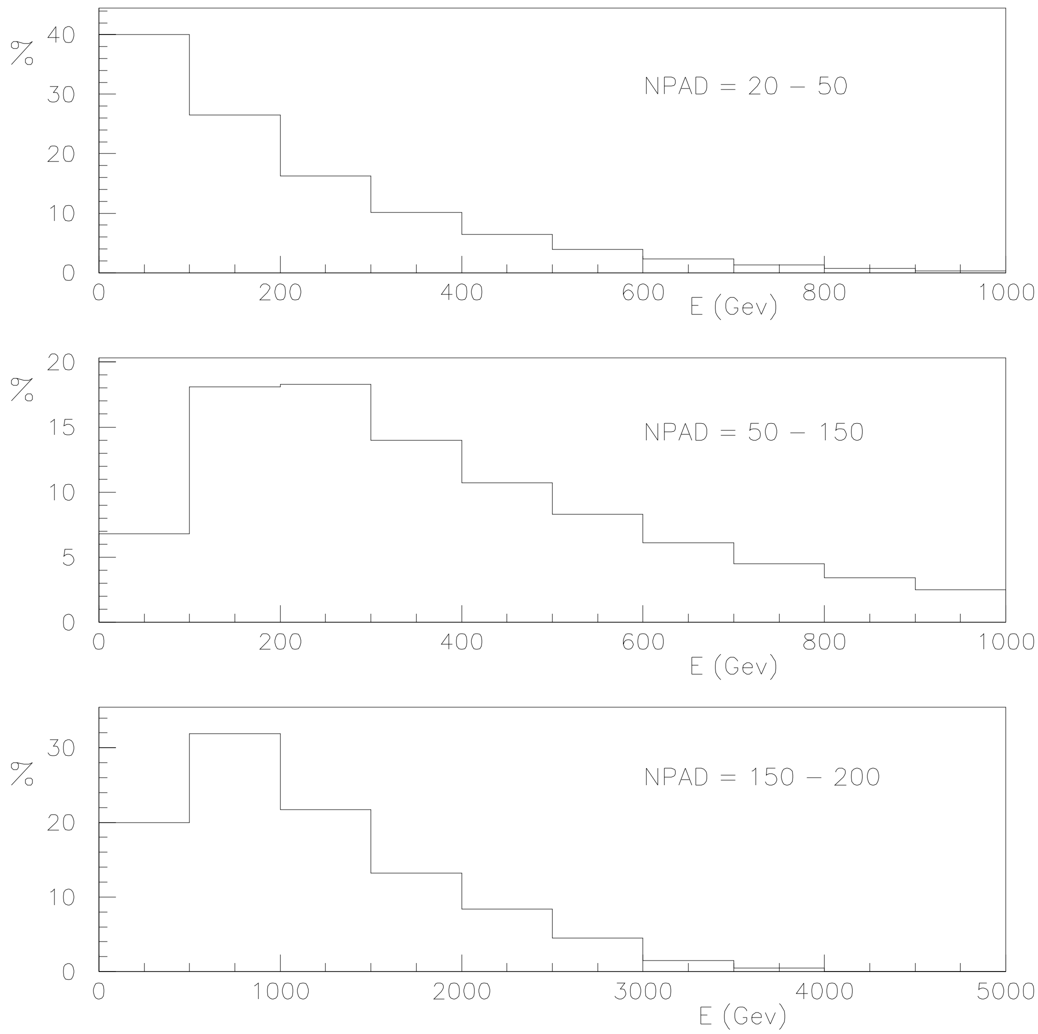

Figure 2.13: The energy spectrum of photons from the Crab detected by ARGO with HMT selections.

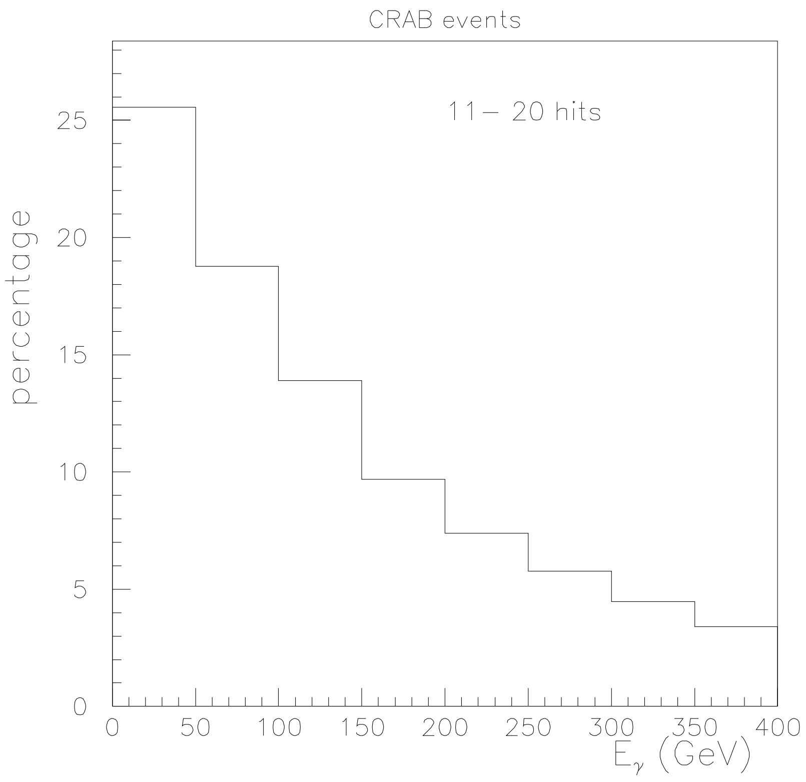

Figure 2.14: Fractional energy distribution of photons from the Crab direction detected by ARGO with using LMT (11–20) selection.

c) SUPERNOVA REMNANTS. The technique employed to search for high energy gamma-rays from SNRs is identical to the standard point-source search method except for the sizes of the source bins. In fact the SNRs are extended object whose size spans from $\sim 0.4^0$ to $\sim 3.2^0$ in diameter, comparable to or larger than the angular resolution of ARGO. According to the catalogues quoted by G. Allen et al. see ref.[15] about 30 SNRs could be observed at the Yanbajing latitude.

Six γ-ray sources observed by EGRET have been associated to SNRs. Two of them (IC433 and γ-Cygni) show a possible association with a molecular cloud. In Table2.5 the size and the integral flux ($E_\gamma > 100 MeV$) as measured by EGRET are reported for these SNRs. Starting from the fluxes measured by EGRET at $100\,MeV$ threshold energy it is possible to calculate the photon flux expected in the $GeV - TeV$ region according to the DAV's predictions of fig. 1.7. By using these fluxes an estimate of the ARGO sensitivity to detect $100 \div 700\,GeV$ photons is easily obtained. In doing this calculation a selection HMT (20-50) + HMT (50-150) has been applied and an angular bin $\theta = [\psi(70) + \Delta\theta]^{1/2}$ has been assumed, with $\psi(70)$ chosen according to the pad selection.

Results are shown in fig. 2.15 where the curves represent the minimum flux at $100\,MeV$, $\phi_\gamma(> 100\,MeV)$, needed for a $5\,\sigma$ detection as a function of the angular bin θ around the source. Four different curves are displayed, to give the sensitivity of ARGO (1 yr of data taking) and ARGO-3600 (2 yr of data taking) to photon fluxes with spectra $\sim E^{-1.3}$ and $\sim E^{-1.4}$. In this plot the SNRs observed by EGRET are represented by squares. According to these results, W44 and γ-Cygni should visible by ARGO-3600 even if the spectrum is steep as $E^{-1.4}$ or more. IC433 is marginally observable provided that the spectrum is flatter ($\gamma \sim 1.3$). The ARGO sensitivity should allow to detect IC433 even if the spectrum falls like $\sim E^{-1.4}$ and, W51 for a spectrum $\sim E^{-1.3}$. We note that assuming a power law as $E^{-1.4}$ the corresponding fluxes at $350 GeV$ are about a factor of 2 lower than the upper limits given by Whipple [15].

Apart from the uncertainties of the model extrapolation, both for what concerns the spectral index or a spectral cut-off, the curves of fig.2.15 provides a clear prevision about the detectability of photons from SNRs once the low energy flux has been determined. Since more than 70% of the signal is due to photons with energies $< 500\,GeV$, ARGO could be sensible also to gamma-ray spectra with an effective cut-off around this energy.

d) MOLECULAR CLOUDS. The projected distribution on the Galactic plane of molecular clouds within $1\,kpc$ of the Sun is shown in fig.2.16 The figure provides also information about the cloud mass and the distance from the Galactic plane. Individual local clouds or cloud complexes are listed in Table 1.3 with their limits in l and b and other data. A large fraction of them is visible at the Yanbajing latitude. This fraction includes as well molecular clouds lying on the Galactic plane - for instance Vul Rift, Cygn Rift - as other outside the Galactic plane - for instance Taurus, Per OB2. Therefore $100\,GeV$ photons can be used as tracers of TeV proton densities also outside the Galactic plane.

EGRET observations of γ-ray emission from Orion and Ophiucus extend up to $10\,GeV$. No data are available at higher energies and from other molecular clouds. On the other hand the diffuse nature of the emission makes very difficult the observation of these sources even

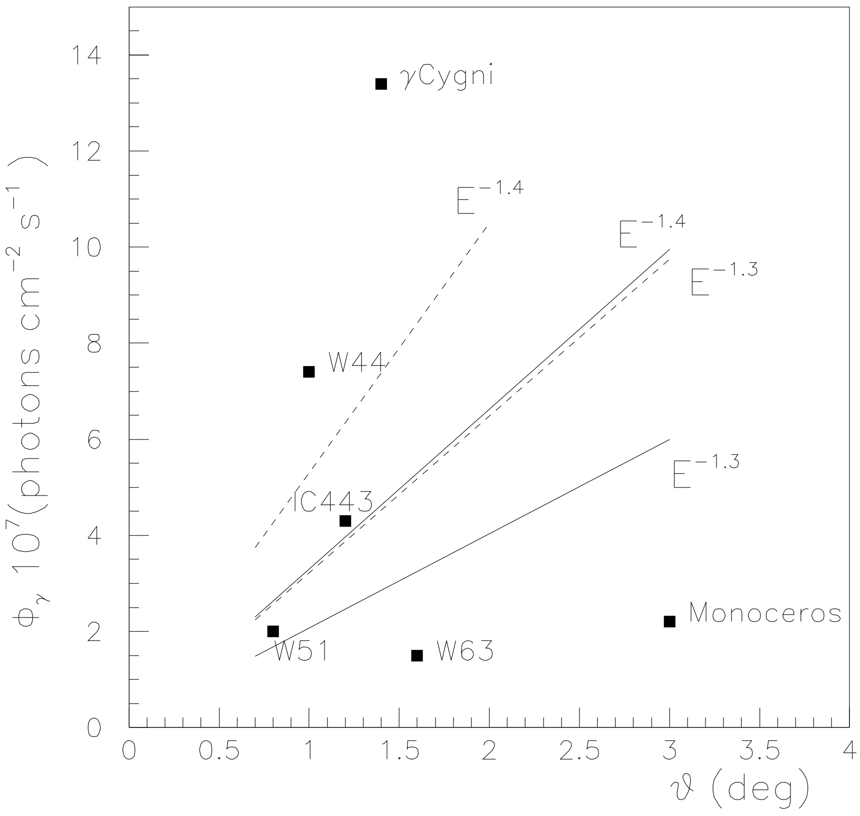

Figure 2.15: The minimum flux $\phi_\gamma(> 100\,MeV)$ as a function of the angular aperture around the source direction needed for a 5σ detection. The four different curves give the sensitivity of ARGO (1 year of data taking) and ARGO–3600 (2 year of data taking) to photon fluxes with spectra $\sim E^{-1.3}$ and $\sim E^{-1.4}$ extending up to 700 Gev. The squares represent EGRET observations of some SNRs

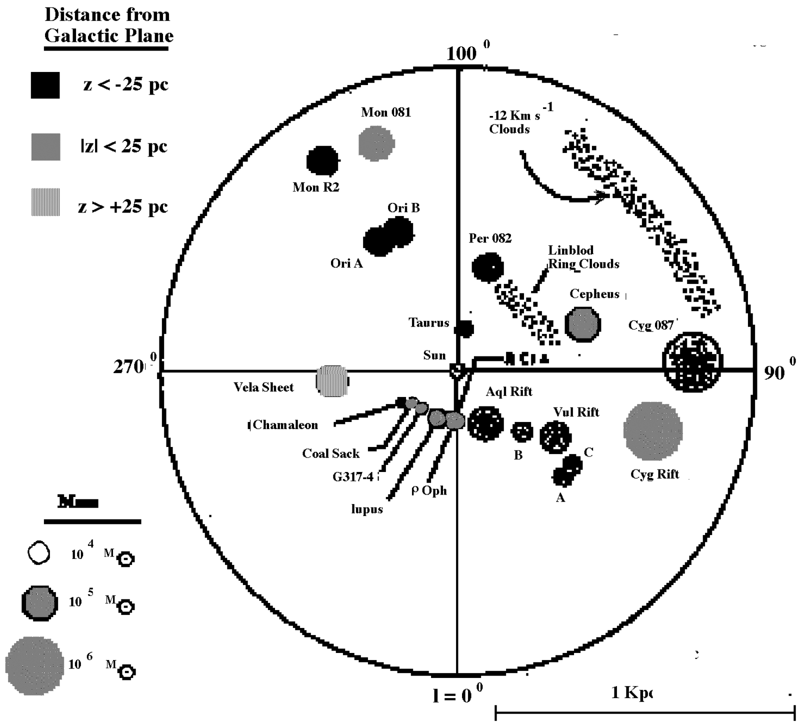

Figure 2.16: The distribution of molecular clouds within 1 kpc from the Sun. The circle radii are proportional to the cube roots of the clouds masses and in most cases are close to the clouds actual radii. The shading indicates distances from the galactic plane.

with the most sensitive Cerenkov telescopes. ARGO represents an unique opportunity to investigate the γ-ray emission at energies not far from the EGRET range and extending up to many hundreds GeV.

Photon spectra detected by EGRET follows a power law $\sim E^{-2.1}$. A direct extrapolation up to the $100\,GeV$ range provides a noticeable flux well above the ARGO sensitivity. However, being the diffuse emission related to the spectrum of protons of higher energies, some steepening of the photon spectrum can be expected unless the molecular cloud hosts cosmic ray sources: some evidence of that can be found in EGRET data. Local γ-ray enhancement can be searched following the selections outlined in the previous sections ('Crab' and 'SNRs'). Here we consider the ARGO sensitivity for diffuse emission. In this case the LMT (11-20) selection seems appropriate.In fig. 2.17 the sensitivity of ARGO-3600 ($5\,\sigma/2\,yr$) is given in terms of the integral flux at $100\,MeV$, $\Phi_\gamma(>100\,MeV)$ and of the angular dimension of the source for three spectral indices ($\gamma = 2.1, 2.3, 2.5$) the ARGO sensitivity ($5\,\sigma/1\,yr$) can be obtained scaling these results by a factor of 1.4. The ARGO sensitivity can be compared to the diffused photon flux from Orion and Ophiucus measured by EGRET, $\Phi_\gamma(>100\ MeV) \geq 10^{-4} cm^{-2} s^{-1} sr^{-1}$. Therefore, the ARGO sensitivity corresponds to a spectrum falling like $E^{-2.3}$ or even steeper if the steepening becomes effective at energies by far greater than $100\,MeV$. In this respect, we note that the spectrum observed by EGRET falls like $E^{-2.1}$ up to $10\,GeV$ at least. A diffuse emission with a similar spectrum extending up to a few hundreds GeV should be detectable in about 3 months of data taking by ARGO, in about $1\,yr$ by ARGO-3600.

e) GALACTIC PLANE. As discussed in the previous chapter, the photon spectrum from the Galactic plane appears to depend on Galactic longitude in the GeV energy range. If this is correct, the γ-ray intensity of the outer Galaxy became stronger than that of the inner Galaxy at energies $> 10\,GeV$ (see fig.1.9).

Two branches of the Galactic plane are observable at angles $< 35^0$ from Yanbajing, the sector $30^0 < l < 100^0$, toward the Galactic Center, and the sector $150^0 < l < 220^0$, toward the anticenter. Thus, the region of inner Galaxy can be explored over a range of about 20^o, while the outer Galaxy is visible over a larger interval of about 70^0. However, in order to settle the ARGO sensitivity we have taken into account the intensity expected for inner Galaxy with an extrapolated spectrum falling like $E^{-2.5}$. The selection HMT (20-50) is used, allowing for a spectral decrease above $500\,GeV$. In fact, with this selection about 72% of the expected signal comes from energies below $300\,GeV$. Calculations have been performed by integrating ± 1.5 degrees in latitude - $|b| < 1.5^0$, $\Delta b = 3^0$ - and considering longitude bins of $\Delta l = 10^0$. An average time of observation of $4.5\,hr/day$ has been assumed. The photon flux from these angular regions should be observed at a $5\,\sigma$ level in 1.5 or 8 months by ARGO and ARGO-3600 respectively at a $\sim 150 - 200\,GeV$ median energy.

With a finer scanning of $\Delta l = 5^0$ these times become about 3 and 15 months respectively. It is of interest the determination of upper limits in case of no detection of a photon excess. In this case, by considering the whole Galactic disk ($\sim 150^0$) we obtain an upper limit (90% C.L.) for the integral flux above $100\,GeV$ of $3.8 \cdot 10^{-10}\,ph/cm^2 \cdot s \cdot rad$ corresponding to a ratio $I_\gamma/I_p = 10^{-6}$ for $E > 100\,GeV$ and $|b| < 1.5^0$.

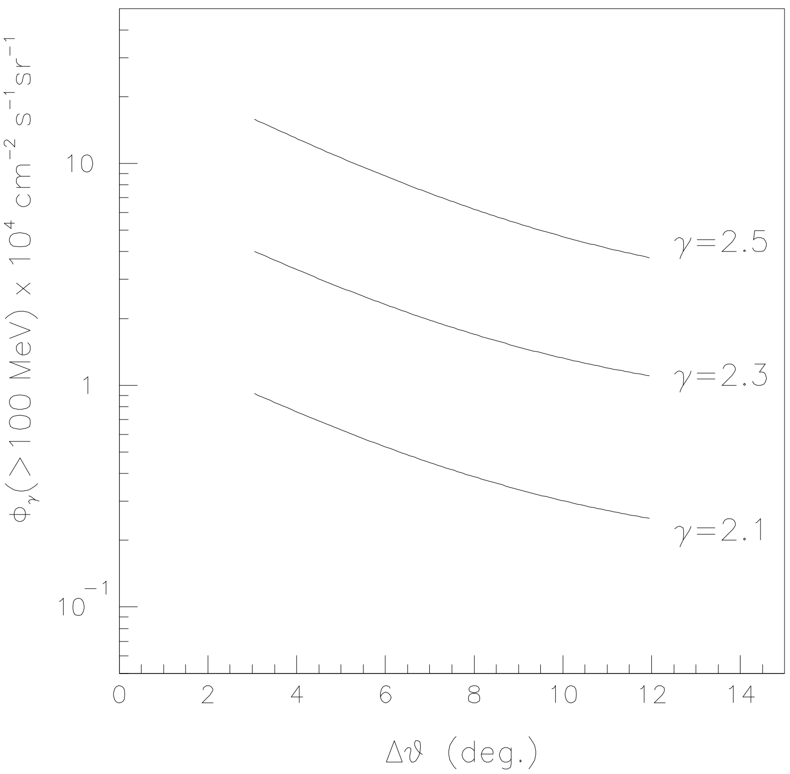

Figure 2.17: The minimum flux at $100\,Mev$, $\Phi_\gamma(>100\,MeV)$ needed for a $5\sigma/2yrs$ detection by ARGO–3600, as a function of the angular dimension of the source. The curves refer to photon emission falling like $E^{-2.1}$, $E^{-2.3}$ and $E^{-2.5}$ up to 700 GeV.

EXTRAGALACTIC SOURCES

The detection of GeV photons from many AGNs (by EGRET) and the observation of 2 of them by the Whipple telescope pose some fundamental questions to be answered by future experiments. Mainly, these can be summarized as follows

a) the level of emission at 100 GeV energy;
b) the spectral evolution up to a few TeV;
c) the time variability both on short and long time scale and correlations at different wavelengths.

Due to the limited energy resolution at hundreds GeV, points a) and b) are in someway correlated. The spectrum shape will depend on the maximum energy attainable by primaries in the source and/or on the interaction with infrared (IR) background photons. As a consequence,we can expect a large variety of spectral evolutions not easy to predict. In order to make some prediction about the ARGO capabilities, we have calculated the minimum average flux for a 5σ detection in one year of data taking for a source spectrum $E^{-\gamma}$ extending without cut–off up to 700 GeV. The HMT($20-150$) selection has been used. The results can be related to the integral flux above 100 MeV and to the spectral index γ observed by EGRET, as shown in fig.2.18. In the same figure the entries represent the 19 sources listed in second EGRET catalog, visible from Yanbajing with $\theta < 30^o$. Circles mark sources with $z < 0.5$, squares sources with $0.5 < z < 1$, and crosses sources with $z > 1.0$. We see that many sources could be detectable provided that the spectrum extends above 500 GeV and no substantial absorbtion is effective. It is important to remark that sources below the EGRET sensitivity ($\Phi_\gamma(> 100\ MeV) < 10^{-7} cm^{-2}s^{-1}$) should be detected by ARGO provided that their spectral index is less than ~ 2. The first EGRET catalog includes 461 sources (radio–loud quasars, BL Lac objects and radio–galaxies) for which only a 2σ $U.L.$ is quoted, 115 of them being visible at the Yanbaijing latitude and satisfying the selection $\theta < 30^o$, $z < 1$. From catalogues of blazars with radioflux (5 GHz) greater than 0.5 Jy (including BL Lacs) we find a total of about 300 sources satisfying the same selection criteria. These sources are, therefore, the natural primary target of the ARGO search. To have information about the ARGO sensitivity to observe a photon spectrum whose shape is essentially determined by the absorption with the IR background, the spectra of Mrk 421 and 3C454, both with the same spectral index have been considered, see fig.2.19.

Mrk 421 (z=0.031) has been detected even by Whipple and the combined fit to data provides a spectrum $1.02 \cdot 10^{-4} \cdot E^{-2.06}\ ph/cm^2\ s\,TeV$ up to about $2\,TeV$. The spectrum of 3C454, at $z = 0.86$, is assumed to be dominated above $100\,GeV$ by absorption effects as determined by a minimal evolution of the IR background with a number density $\propto \epsilon^{-2.55}$ (ϵ=IR photon energy), see ref[63]. Thus, the ratio of integral fluxes $\phi_\gamma^{3C454}(> E)/\phi_\gamma^{Mrk421}(> E)$ is about 4.4 at 10 GeV but only 0.2 at 400 GeV, so that this represents a typical case of a source (3C454) very bright at EGRET energies but very faint at 400 GeV threshold energy (as for Whipple). ARGO sensitivity is obtained by selecting events from source direction with a number of fired pads 20-150. The source 3C454 is detected at a level of $5\,\sigma$ in about

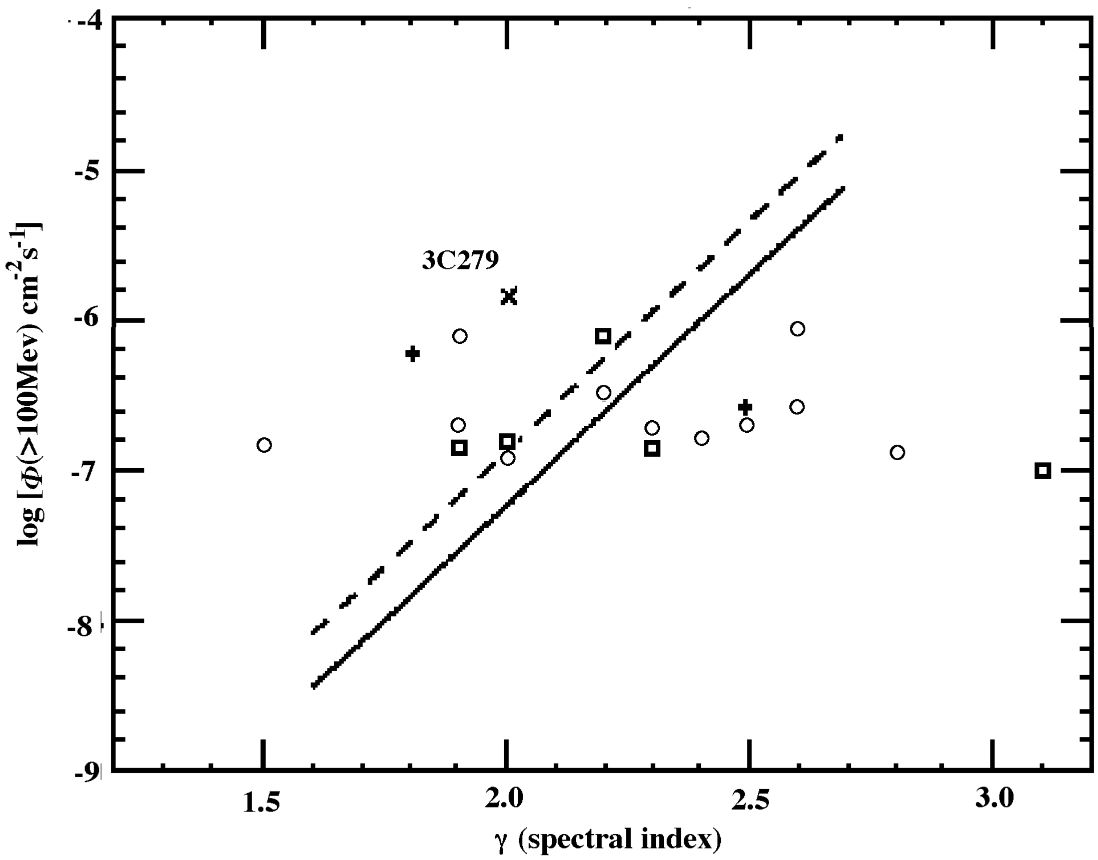

Figure 2.18: The minimum flux at 100 MeV threshold, $\Phi_\gamma(> 100\ MeV)$ needed for a $5\sigma/1yr$ of data taking by ARGO (solid line) and ARGO–3600 (dashed line) as a function of the differential spectral index. The points represent 19 sources observed by EGRET visible from Yanbajing with $\theta < 30^o$; circles $z < 0.5$, squares $0.5 < z < 1$, crosses $z > 1.0$, rhombs z unknown. The brightest AGN detected by EGRET, the quasar 3C279, visible at Yanbajing at angles $\theta > 30^o$, is shown for comparison

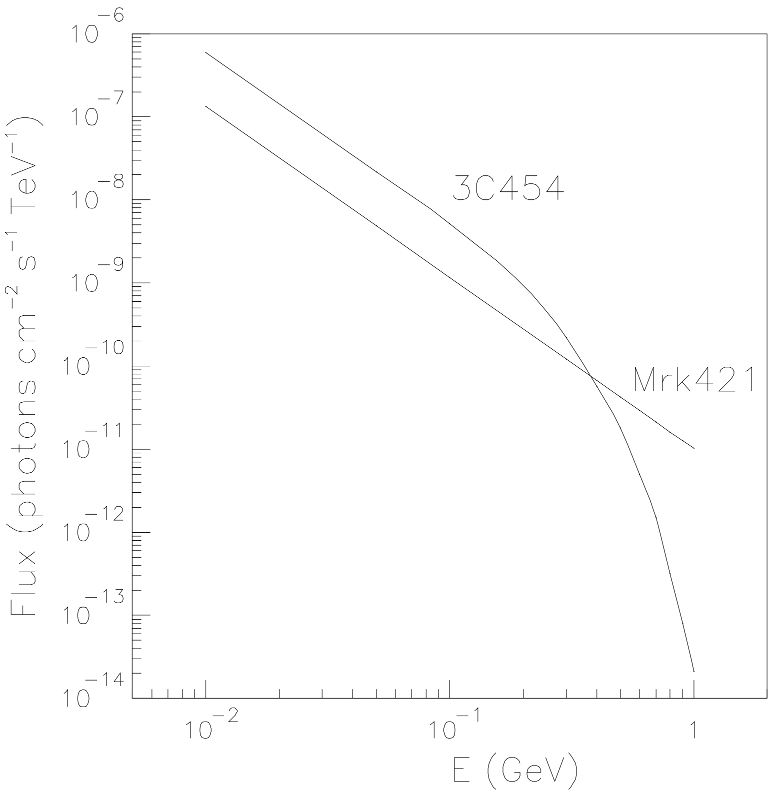

Figure 2.19: Photon differential spectrum of Mrk 421 and 3C454 (see text)

40 days of observation (about seven months by ARGO 3600). On the contrary, the detection of Mrk421 requires 3 and 16 months respectively. The purpose of this calculation is not only to make concrete predictions but rather to show as the ARGO sensitivity largely depends on the spectral shape in the energy range $50 \div 300 GeV$. This is well evident in fig2.20 where the photon spectrum of 3C454 as observed by ARGO is shown: about 60% of the detected events is due to photons with $E < 200GeV$. On the other hand, the spectral shape of distant sources can be heavily conditioned both by density and evolution of the IR background, ref.[63], so that it is not possible to assess firmly the ARGO sensitivity. However, previous calculations indicate that the detection at $5\,\sigma$ level in 1 yr of data taking (or 2 yrs for ARGO-3600) corresponds to a differential flux at $100GeV$ $J_\gamma(100GeV) = 6 \cdot 10^{-13} \div 1.5 \cdot 10^{-12} ph/cm^2 sGeV$, depending on the spectral shape ($J_\gamma(100GeV) = 10^{-12} \div 2.5 \cdot 10^{-12} ph/cm^2 sGeV$ for ARGO-3600). Comparing these findings to the results of the previous analysis concerning the Crab (with a spectrum falling like $E^{-2.69}$) we can conclude that a differential flux $J_\gamma(100\,GeV) = 10^{-12}\,ph/cm^2\,s\,GeV$ is well appropriate to characterize the ARGO sensitivity in 1yr of data taking. The corresponding number for ARGO-3600 on a base of 1 yr (2 yrs) is about a factor of 2.1 (1.7) higher.

The ARGO capability to follows the flux variations of blazars is shown in fig.2.21 where the photon rate as a function of the integration time T is plotted for a $3.5\,\sigma$ detection. It results from the plot that for a 5-day (10–day) observation time a flux increasing up to the Crab flux (2/3 of the Crab flux) is requested. This corresponds, for instance, to an increase of the Mrk421 flux of a factor ~ 3 (or 2), less than the increase detected by Whipple during the outburst of 1994 May 14 and 15. For ARGO-3600 the curves must be reduced of a factor of about 2.3, so that only intense variations can be followed on a time scale as short as 5 days.

An important point to remark is the possibility to monitor the Crab flux with 2.5σ sensitivity to variations of about 30% integrating data for 20 days. Though the ARGO sensitivity, for point sources, cannot compete with the limits expected for the next generation of air Cerenkov telescopes, ARGO will have the crucial advantage over them of a large angular coverage of the sky and a high duty cycle factor. ARGO will be able to provide a systematic and continuous monitoring of the $-10^0 < \delta < 70^0$ declination band observing a large amount of discrete galactic and extragalactic candidate sources and extended regions as the Galactic plane, SNRs and molecular clouds. All the analysis discussed for the search of galactic and extragalactic point sources have been done considering only the events with at least 20 fired pads. The other recorded events having 10 to 20 fired pads with a poor expected angular resolution but with a lower average energy has not been considered. It is obvious that at least part of these events can be used for the point source search. Therefore all the reported result are conservative both with respect to the energy threshold than to the minimum detectable flux. An optimization of the cuts to be applied will be done with the real data using the Crab as monitor photon beam.

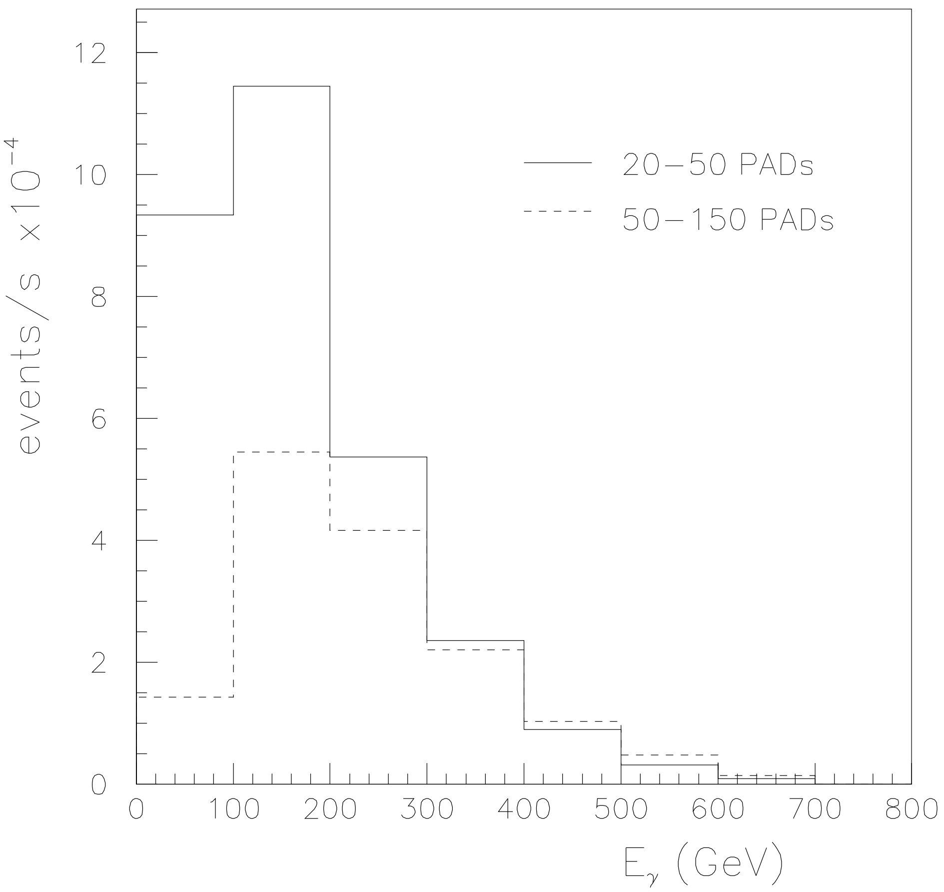

Figure 2.20: The photon spectrum of 3C454 detected by ARGO according to our simulation

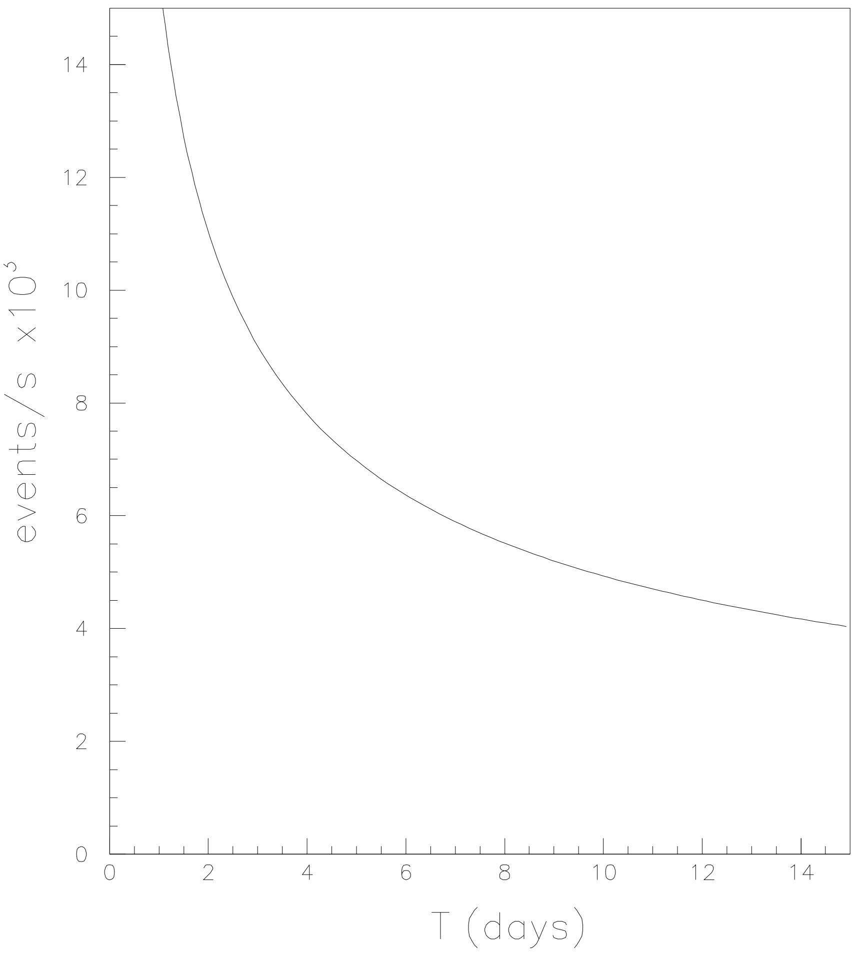

Figure 2.21: The photon rate for a $3.5\,\sigma$ detection as a function of the integration time T.

2.4 GAMMA RAY BURSTS

We discuss the ARGO sensitivity to observe Gamma Ray Bursts in the energy range E > 1 GeV in time coincidence with the events detected in the keV-MeV region by satellites experiments.

Given a Gamma Ray Burst observed by a satellite detector in a sky position inside the ARGO field of view, the search consists in the comparison of the number of showers detected at the burst time whose arrival directions are compatible with the burst location, with the number of showers expected from the cosmic ray background.

The calculations are performed for different burst parameters, as time duration, intensity, spectrum slope and energy cutoff. The suitable trigger for the detection of photons in the GeV range is the previously defined LMT($\geq$ 6). The correspondent effective area of the detector $A^{\gamma}_{eff}(E)$ for primary photons at an average zenith angle $\theta = 20°$ can be obtained by summing the contributions shown in fig. 2.7 and fig.2.9. The effective area of ARGO increases with the gamma energy up to a "plateau" value of $4 \cdot 10^4\, m^2$ at $E = 1\, TeV$. The detector is still sensitive to gamma energy of few GeVs, being $A^{\gamma}_{eff}(E) \sim 1\, m^2$ for $E \sim 4 GeV$. The effective area for ARGO-3600 is $\sim$ 5 times lower at $10\, GeV$, and $\sim$ 2.2 times lower at $1\, TeV$.

We note that the sensitivity obviously decreases by increasing θ and the results given here can be considered as averaged values for the θ range $0° - 35°$.

Given a Gamma Ray Burst with time duration Δt and a photon power-law differential energy spectrum $dS(E)/dE = K\ E^{-\alpha}$ ph cm^{-2} s^{-1} GeV^{-1} in the energy range 1 GeV < E < E_{max}, the total number of detected shower from the burst, with reconstructed arrival directions inside a circular window of radius ψ centered on the source position, is

$$N \ = \ \epsilon\ \Delta t \int_{1\ GeV}^{E_{max}} \frac{dS(E)}{dE}\ A^{\gamma}_{eff}(E)\ dE$$

where ϵ is the fraction of showers from the burst with arrival directions inside the given window and depends on the angular resolution of the detector. In the following calculation $\epsilon = 0.7$, corresponding to $\psi(70) = 4°$ for ARGO and $\psi = 5°$ for ARGO-3600. The number of detected events has to be compared with the background fluctuations. The number of background events recorded during the time Δt from a circular window of radius ψ is given by

$$N_b \ = \ \Delta t\ 2\pi(1 - cos\psi) \int_{E_{p1}}^{E_{p2}} \frac{dS_p(E_p)}{dE_p}\ A^{p}_{eff}(E_p)\ dE_p$$

where $dS_p(E_p)/dE_p$ is the proton differential spectrum, and $A^{p}_{eff}(E_p)$ is the effective area for the detection of protons of energy E_p (see fig.2.7 and fig.2.9) Note that the effective area for protons detection is $\sim$ 5 times lower than the effective area for photons detection at 10 GeV, and $\sim$ 2 times lower at 1 TeV.

In these calculations the proton spectrum given in ref. [62] has been used. The results do not change taking also into account the Helium contribution to the background (< 15% at these energies). In this calculations $E_{p1} = 10\, GeV$ because of the local geomagnetic cutoff, and $E_{p2} \sim 5TeV$ being the contribution at higher energies negligible. The obtained expected rate of background events is 319 s^{-1} and 109 s^{-1}, respectively for ARGO and ARGO-3600.

Assuming a uniform time distribution of the background, a given Gamma Ray Burst is detectable if the number of the signal events N is significantly larger than the background fluctuations. Requiring the significance of the signal at 4 standard deviations, we have evaluate the minimum detectable flux, i.e. the minimum value K_{min} of the spectrum coefficient K for different slope α of the spectrum. If K_0 is the minimum value of K obtained for $\Delta t =$ 1 s, given a generic duration Δt, $K_{min} = K_0/\sqrt{\Delta t}$.

Fig.2.22 shows K_0 as a function of the cutoff energy E_{max} for different slopes of the energy spectrum $\alpha = 1.0, 1.5, 2.0, 2.5, 3.0$. The K_0 values are given for ARGO and ARGO-3600. One can see how the sensitivity depends on the slope of the spectrum and, mainly for "hard" spectra, strongly increases with the cutoff energy . ARGO is more sensitive than ARGO-3600 by a factor ranging from 1.6 (for $\alpha = 1$ and $E_{max} = 1\,TeV$) to 3.3 (for $\alpha = 3$ and $E_{max} = 10\,GeV$).

Considering that the energy spectrum is measured in the MeV region by satellite detectors, these results shows how the ARGO measurements can provide important information about the energy cutoff of the spectrum in the GeV region.

From these results it is possible to evaluate the minimum energy fluence F_0 above 1 GeV for a detectable burst of duration $\Delta t = 1$ s as a function of E_{max}, for different spectrum slopes, fig.2.23. The correspondent value F_{min} for a generic burst of duration Δt, is $F_{min} = F_0 \times \sqrt{\Delta t}$.

Fig.2.24 shows the minimum detectable energy fluence in the 10-100 GeV energy range for a Gamma Ray Burst of duration $\Delta t = 10$ s and spectrum exponent $\alpha = 3$ and $E_{max} = 1.TeV$. As a comparison the upper limits obtained by EAS-TOP in the same energy range using the same spectral parameters in a GRB search in coincidence with 45 BATSE bursts [64] are shown in the same figure, together with the fluences measured at lower energy by BATSE and EGRET during the powerful event GRB940217 [65].

To give an idea of the detector sensitivity and to provide a raw estimation about the rate of observable events, one can calculate the significance of the signals that would have been observed by ARGO during the occurrence of the high energy gamma ray bursts detected up to now by EGRET. In ~4 years of measurement EGRET detected 5 GRBs with photons of energy E > 30 MeV [66] in coincidence with BATSE. Two of them, GRB 910503 and GRB 930131, with reasonable assumptions on the energy spectrum at high energy, would have been fully detectable, obviously if they occurred in the ARGO field of view.

The photon flux measured by EGRET in the 2 s peak during GRB910503 is $dI/dE = 8.7\ E(MeV)^{-2.24}$ ph cm^{-2} s^{-1} MeV^{-1} [67]. No energy cutoff was observed in the shape of the spectrum. The highest photon energy measured during this event was ~233 MeV. The steepness of the spectrum and the small detection area of EGRET can account for the non-observation of more energetic photons. Assuming the photon spectra extending up to E_{max} = 40 GeV with the same slope observed at lower energies, the signal in ARGO would reach 4 standard deviations. With the assumption E_{max} = 100 GeV the burst is also detectable by ARGO-3600 with the same significance. In the 1 s peak during GRB 930131 EGRET measured a flux $dI/dE = 1.9\ E(MeV)^{-1.97}$ ph cm^{-2} s^{-1} MeV^{-1}, with no visible energy

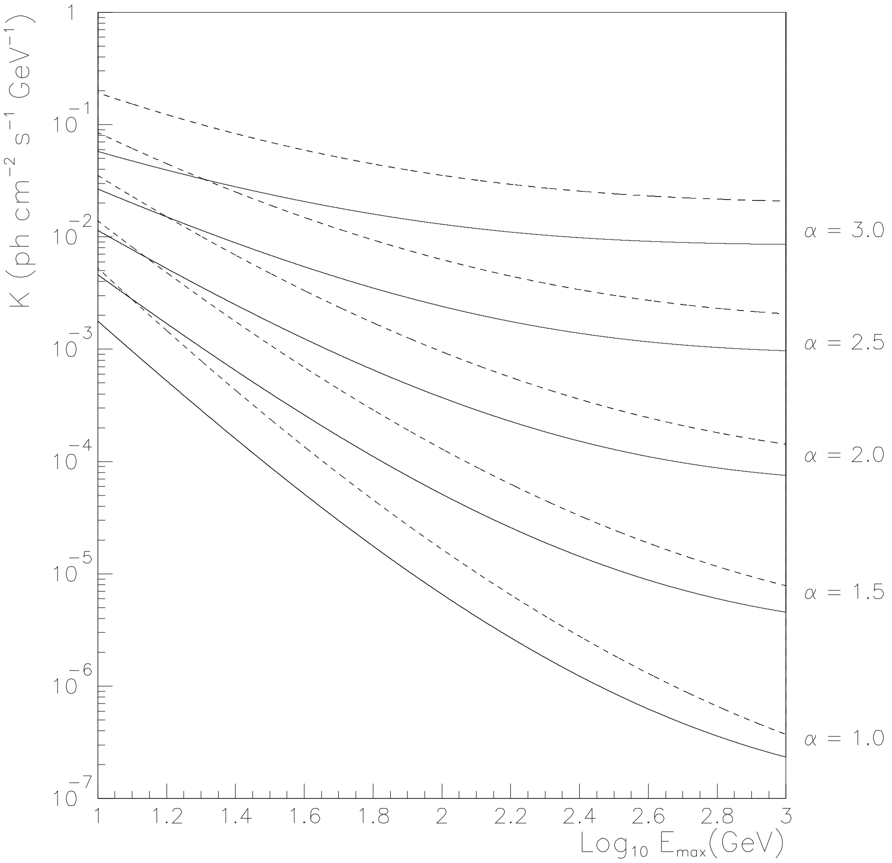

Figure 2.22: The minimum value of K for a detectable burst of time duration $\Delta t = 1$ s as a function of the energy cutoff E_{max}. K is the coefficient of the assumed burst spectrum $S(E) = K \times E^{-\alpha}$ ph cm^{-2} s^{-1} GeV^{-1} valid in the energy range 1 GeV $< E < E_{max}$. K is given for 5 different values of the spectrum slope α and for two detector area ARGO (solid line) and ARGO–3600 (dashed line).

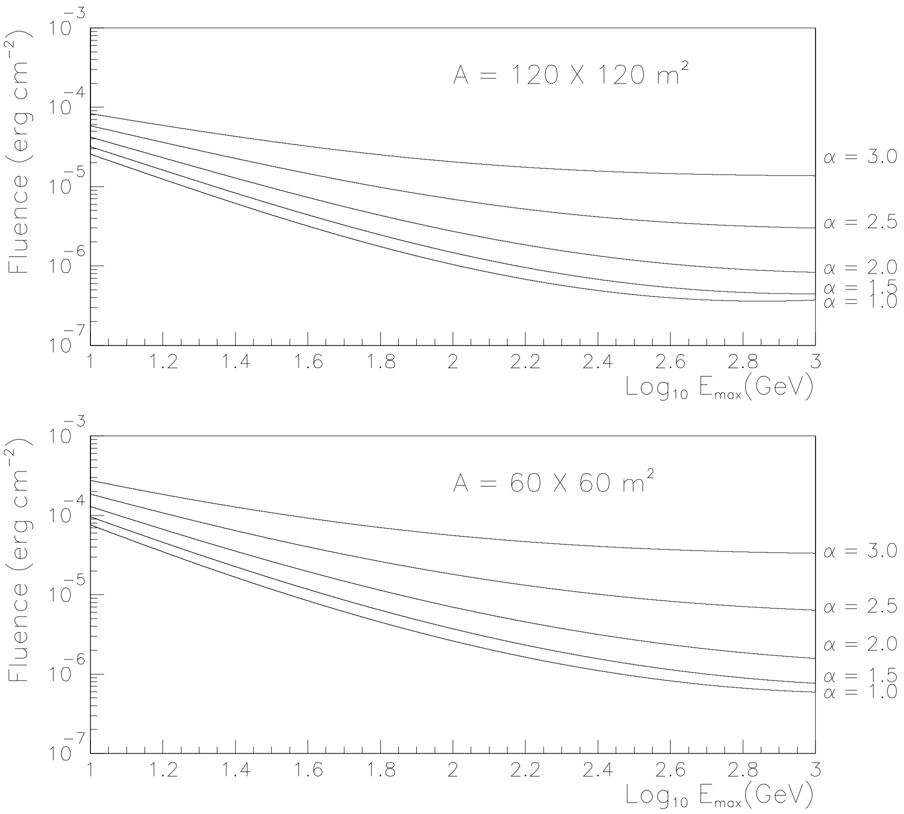

Figure 2.23: The minimum value F of the energy fluence in the range 1 GeV $< \; E \; < \; E_{max}$, for a detectable burst of time duration $\Delta t = 1 \; s$. The burst spectrum is assumed to be a power law one extending in the energy range 1 GeV $< \; E \; < \; E_{max}$. F is given for 5 different values of the spectrum slope α.

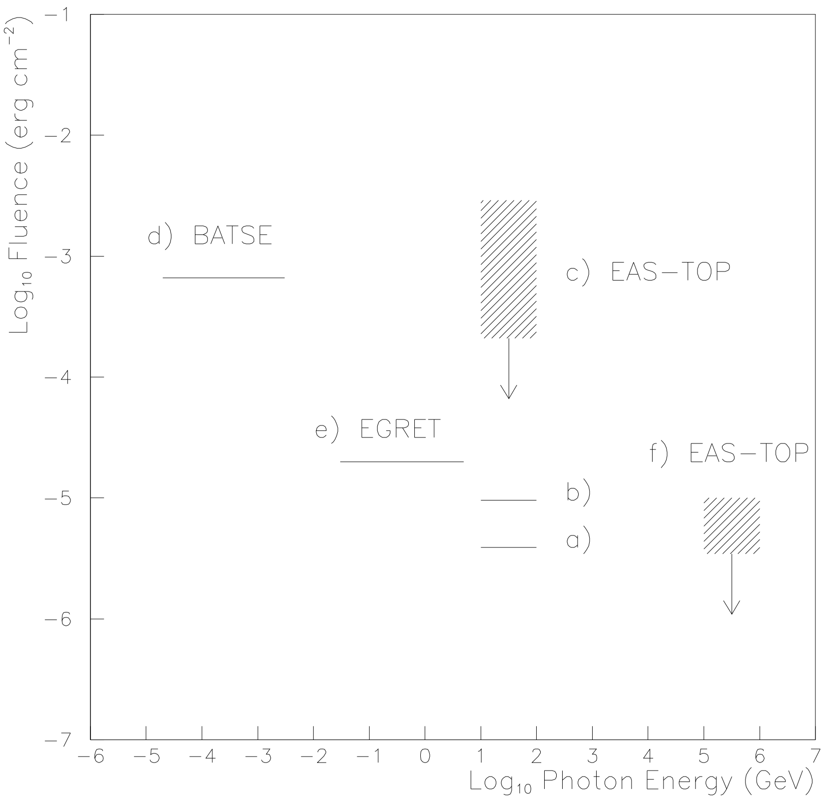

Figure 2.24: The minimum energy fluence detectable by ARGO in the energy range 10 GeV $< E <$ 100 GeV for a gamma ray burst of duration $\Delta t = 10$ s and spectrum slope $\alpha = 3$ and $E_{max} = 1$ TeV for ARGO (line *a*) and ARGO–3600 (line *b*); upper limits obtained by EAS-TOP in the same energy range using the same spectral parameters in a GRB search in coincidence with 45 BATSE bursts (box *c*); fluences measured at lower energy by BATSE (line *d*) and EGRET (line *e*) during the powerful event GRB 940217.

cutoff; the highest photon energy was 1.2 GeV [68]. Assuming E_{max} = 25 GeV, the burst is detectable by ARGO, while for E_{max} = 50 GeV it is detectable also by ARGO-3600. Increasing the energy cutoff up to 100 GeV, the signal reaches 28 s.d. and 11 s.d. in ARGO and ARGO-3600 respectively.

Taking into account the EGRET detection of a 18 GeV photon during GRB 940217 [65], the assumption that the energy spectrum could extend up to a few tens of GeV is quite reasonable. Hence, considering that the EGRET field of view is about 0.5 sr, one can expect about $1 \div 2$ event per year observed by ARGO in the sky region $\theta < 35°$. The expected rate can be increased extending the observations up to $\theta = 50°$; at higher zenith angles the sensitivity is obviously lower but the field of view is a factor 2.7 larger. The calculation of the sensitivity for showers at zenith angle $\theta > 35^o$ will be presented in a separate paper.

2.5 MEASUREMENT OF THE $\overline{p}/p$ RATIO ABOUT 1 TeV

Prior observations of the Moon shadow have been performed by CYGNUS [69], CASA [70], EAS-TOP [71], HEGRA [72] and AS-γ [73] experiments. These studies have been made to provide the angular resolution of the arrays and the overall pointing accuracy. The best determination comes from the AS-γ experiment operating at a $10\,TeV$ threshold, owing to a larger statistics as compared to that of the other experiments operating at $100\,TeV$ energy threshold. The shadow appears displaced toward west - as expected - of the right amount corresponding to an angular displacement $\Delta\theta = \frac{30mrad}{E(TeV)}$ (fig. 1.16).

ARGO will have the crucial advantages of *i)* a lower threshold energy, *ii)* the possibility of selecting the energy range of the primary beam and *iii)* a better angular resolution.

At energies below a few TeV the shadows cast by protons and antiprotons are expected sufficiently resolved to allow an unbiased measurement of the $\overline{p}/p$ ratio. To check this hypothesis a MonteCarlo calculation has been carried out which makes use of the results obtained in the previous Chapter to define the proton beam intercepted by the Moon. Results in the following refer to ARGO-3600 but can easily scaled to ARGO.

In fig.2.25 the energy distribution of the protons intercepted by the Moon and corresponding to events with 30-50, 50-150, 150-350 pads are shown. The angular resolutions pertinent at these categories are 0.38^0, 0.29^0 and 0.14^0 respectively. Adding these contributions we get the proton beam intercepted by the Moon in 3 year of data taking ($\simeq$ 1200 hours/year for Moon observation at angles $< 45^0$). The total number of protons is about 10^5 with the energy distribution shown in the figure. The results of our MonteCarlo simulation accounting for the experimental angular resolution is shown in fig.2.26. This figure concerns the distribution of the arrival direction of air showers produced by the protons intercepted by the Moon. In doing this calculation a magnetic deflection along the East-West axis has been considered neglecting the tilt of the geomagnetic dipole. A random fluctuation up to 5% of the bending power $\int B\,dl$ has been taken into account. The shadow departs strongly from a circular shape and is elongated as compared with the 9 $mrad$ angular dimension of the Moon. Along the North–South direction about 97% of the events is inside $\Theta_y = \pm 0.3^o$.

The distribution displays a marked edge on the low angle side, as well shown in fig. 2.27, where a projection along the right ascension of the distribution of fig.2.26, with $\Theta_y = \pm 0.3^0$, has been performed. This is due to the fast energy dependence of the primary beam and to the high accuracy in reconstructing the direction of high energy showers. The tail at large angles correspond to low energy protons. 'Events' beyond 17^0 correspond to protons with $E < 100\,GeV$, about 2% of the proton flux obscured by the Moon. As a result the overlap of the proton shadow over the negative angles (eastward) is quite small. We find 1051 events ($\sim$ 1%) in the angular interval $\Delta\Theta_x = -0.5^o - 0.^o$, and only 10 events ($\sim 10^{-4}$ beyond -0.5^o). Thus, the separation of the antiprotons from the protons remains quite good. Our simulation suggests an acceptance cut $\pm 0.5^0$ around the Moon center to reduce the proton contamination to the antiproton shadow below 10^{-3} with a loss of the signal of about 10%. In an angular box $\Delta\Theta_x = 0.5^0 \div 4.5^0$, $\Delta\Theta_y = -0.3^0 \div 0.3^0$ about 70% of the signal is contained, corresponding to a number of missing events of about 72×10^3 events.

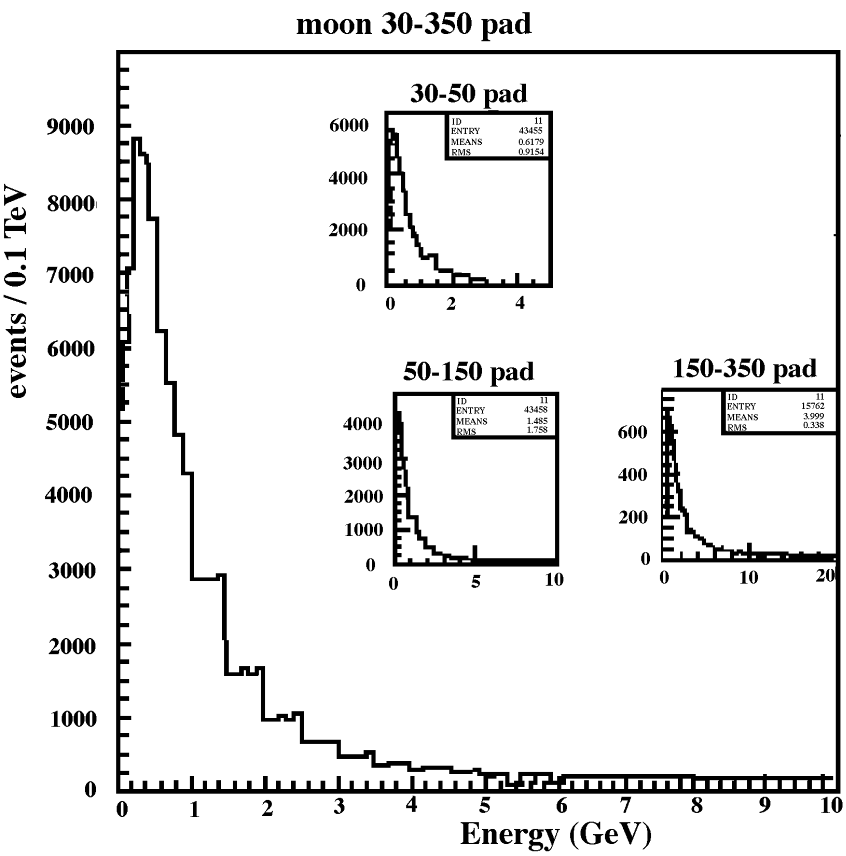

Figure 2.25: The energy spectrum of protons intercepted by the Moon in 3 years of data taking according to the selections HMT(30–50), HMT(50–150) and HMT(150–350). Calculations are for ARGO–3600.

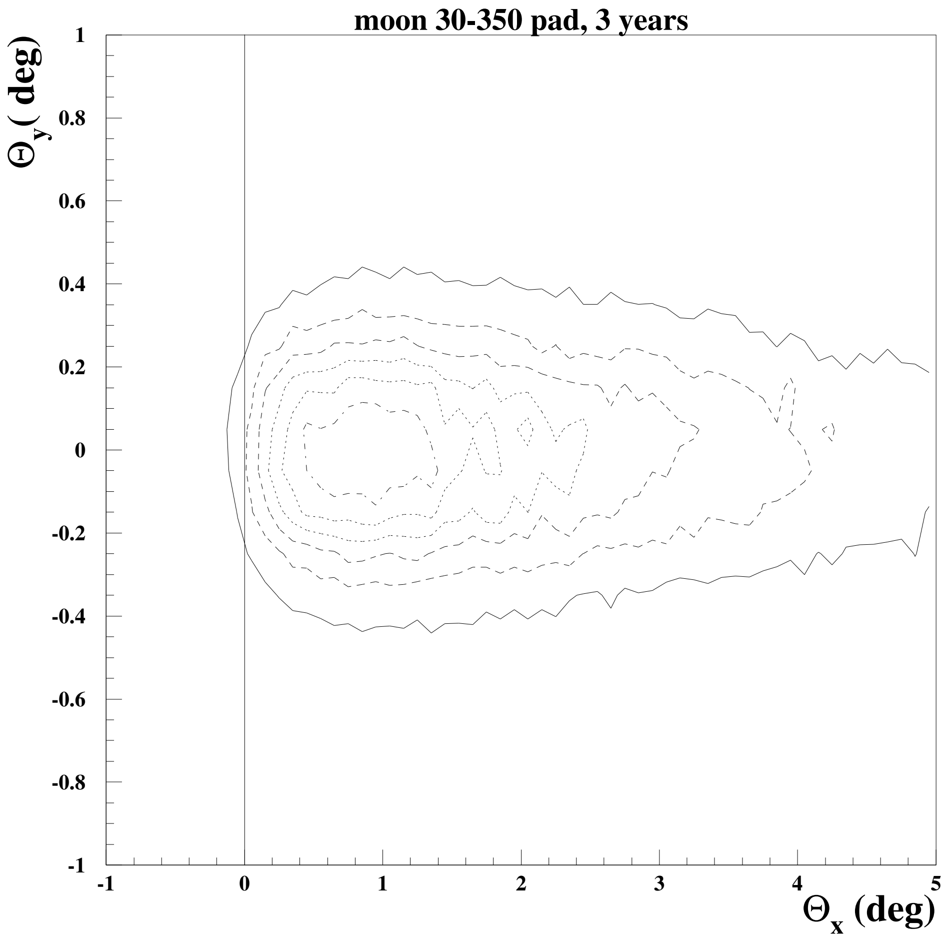

Figure 2.26: Distribution of the arrival direction of air showers produced by the protons intercepted by the Moon. Θ_x and Θ_y measure the angular distance from the Moon center along the right ascension (E–W direction) and the the declination (S–N direction), respectively.

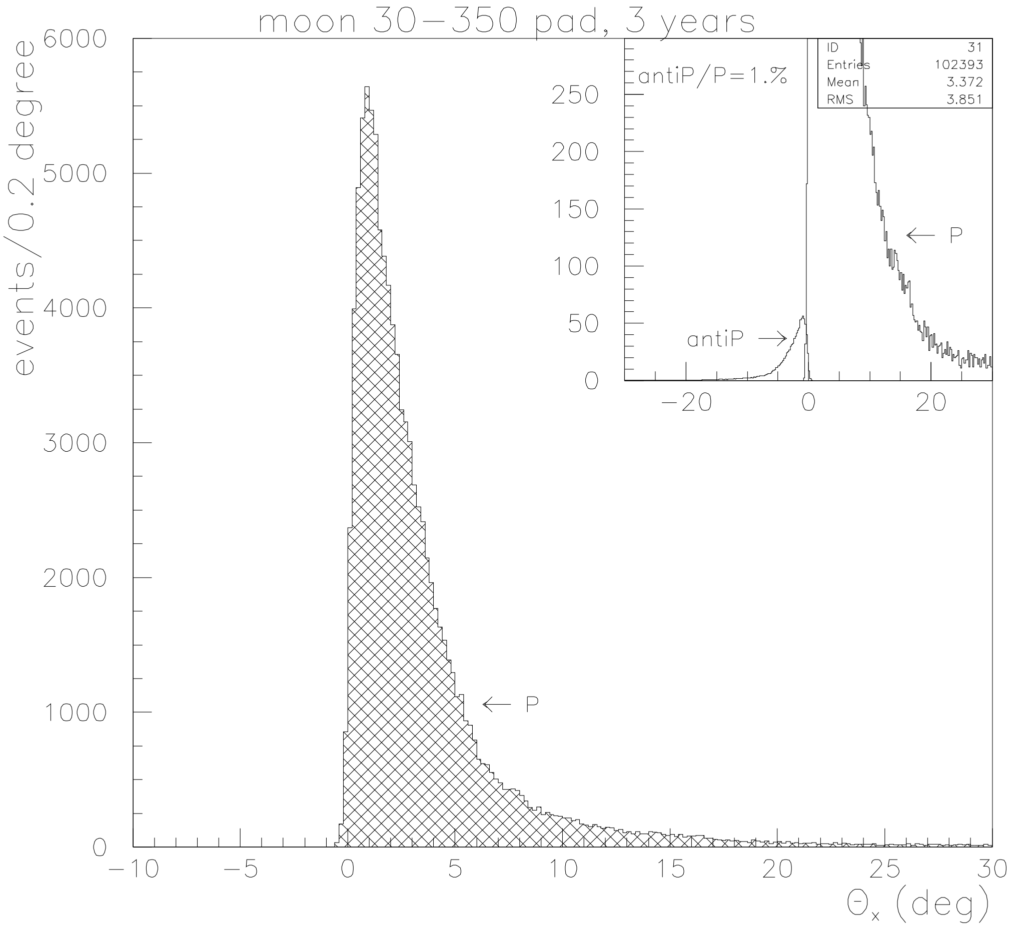

Figure 2.27: Projection along the right ascension of the proton beam intercepted by the Moon. Inset shows the effect of an 1% antiproton component in the beam

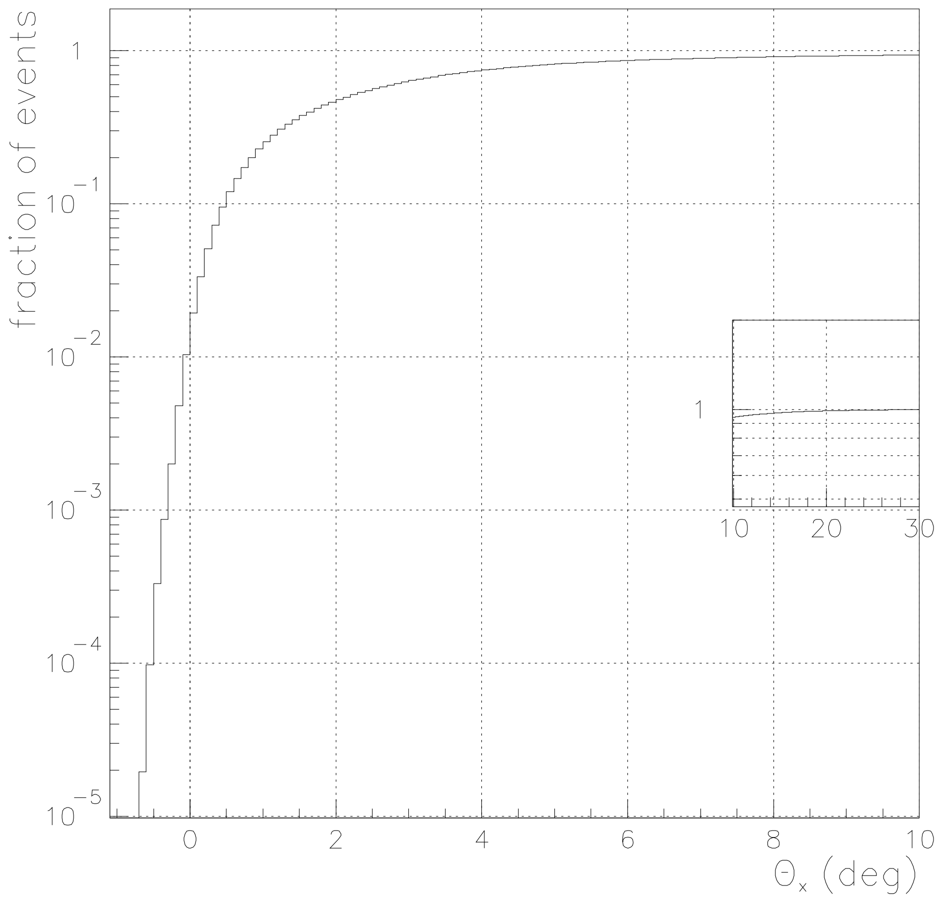

Figure 2.28: Integral distribution of the protons intercepted by the Moon as a function of the right ascension.

The search for antiprotons should be made according to the following steps

a) observation of the proton shadow in different energy ranges even beyond $10\,TeV$. Looking at the angular displacement of the shadow with respect to the position of the Moon should provide a unique energy calibration and information on systematic pointing errors. The angular resolution will be directly measurable by its influence on the edges of the shadow.

b) study of the regions around the Moon shadow displaced of more than 1^0 in the North-South directions in order to obtain with high statistical significance the level of the background density to be subtracted.

c) determination of the 'deficit profile' and estimate of the total number of missing protons. This measurement should provide an absolute calibration of the proton beam intercepted by the Moon.

d) search for the antiproton shadow looking eastward instead of westward.

Since the number of background events can be measured with high accuracy by integrating in regions external to the Moon shadow, $|\Theta_y| > 0.5^o$, the significance of the detected deficit depends on the measured number N_{meas} of events in the optimal acceptance bin. For instance,the expected number of shadowed protons in the selected angular bin ($\sim 72\times10^3$) as to be compared to the statistical error $\sqrt{N_{meas}(\Delta\Theta_x, \Delta\Theta_y)} = 1030$. Thus,the proton shadow is measured with high statistical significance and its profile could be used to evaluate the profile of the antiproton shadow. By considering only the integrated number of events we obtain a conservative estimate of the ARGO sensitivity. We find that an antiproton flux as predicted by Stecker and Wolfendale would be detected by ARGO-3600 with 3.5σ significance in 3 years of data taking at a median energy of about 1 TeV. Since ARGO gains a factor of 9 in effective area as compared to ARGO-3600, it could measure this signal with 6σ accuracy in only 1 year of data taking.In case of no signal detection,the upper limits at 90% C.L. set by ARGO(2 yrs of data taking) and ARGO-3600(3 yrs of data taking) are 6.5×10^{-3} and 1.6×10^{-2} (see fig.2.29). Since the theoretical evaluation of the antiproton/proton ratio for baryon-symmetric Universe models is far above such limits while this ratio for antiprotons originating in the Galaxy is expected to be much below, the operation of ARGO could be support or refuse the hypothesis of an extragalactic origin of the antiprotons. In doing this study ARGO will benefit of the experience gained by the AS-γ experiment operating at the same site and performing the same type of analysis.

Since the ARGO efficiency is quickly increasing with energy and TeV showers should be detected with very high angular accuracy ($\sigma_\theta < 0.15^o$), the study of the antiproton/proton ratio could be made up to about 5 TeV at least. The sensitivity in this energy region will be mainly limited by the weight of systematic pointing errors. Finally, we note that since at a rigidity $\sim 10^3\,GV$ the flux of helium nuclei is about 10% of the proton flux and the effective area of ARGO is less of about a factor of two, a contamination to the proton shadow of 5% is expected. Simulations are in progress and results will be presented in a separate document.

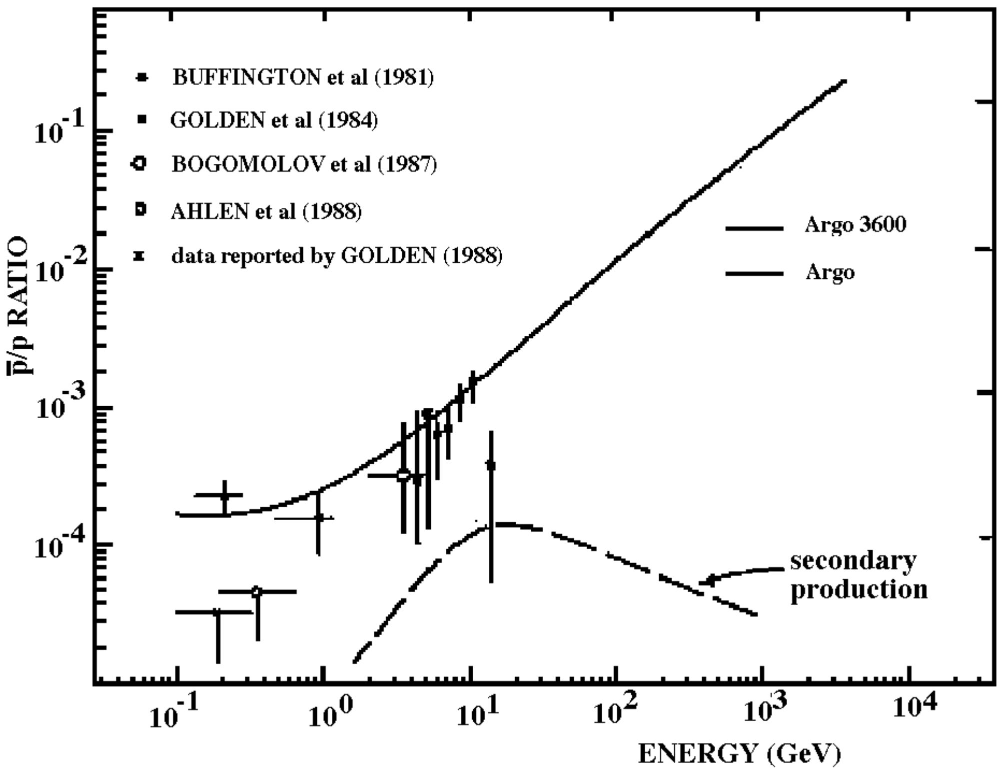

Figure 2.29: Upper limits at 90% c.l. on the $\bar{p}/p$ ratio set by ARGO and ARGO–3600 in case of no signal detection (see text).

2.6 THE PROTON SPECTRUM IN THE ENERGY RANGE $10 \div 200\,TeV$

As shown in the previous chapter, EAS induced by primary protons with energy $E > 5\,TeV$ can be fully detected by ARGO with no bias. Since the width of the size distribution at energies $> 10\,TeV$ is $< 35\%$ a strong correlation is expected between the primary energy and the shower size. On the other hand, by imposing the core position being located inside a small fiducial area - say $10 \times 10\,m^2$ - at the center of the carpet, a large fraction of the shower should be sampled even by ARGO-3600. Therefore, we expect a substantial correlation between the proton energy and the recorded number of hits. The possibility of correlating the hit distribution to the primary spectrum and the sensitivity to identify a change of the spectra index have been investigated as follows.

1. proton showers at angles 0 to 10^o have been simulated, with core hitting a $100m^2$ area centered on the detector. Their energy distribution has been sampled according to curve (1) and curve (2) of fig.1.17 from $E_{min} = 5\,TeV$ to $E_{max} = 400\,TeV$. The total number of events for each simulation corresponds to about 10 days of data taking. In order to reduce the computer time, a cut of 5 MeV has been applied to the electromagnetic component.

2. for each event, the total number N_h of fired strips at distance intervals $\Delta R = 5 \div 25\ m$ and $\Delta R = 5 \div 50\ m$ from the shower core is counted. Core determination for such events is better than 1 meter. The lower cut $R = 5\ m$ to the strip distance from the shower core is applied to avoid saturation effects. The maximum distance is determined by the detector size;the first choice refers to ARGO-3600,the second one to ARGO

3. the integral distributions of fig.2.30 and fig. 2.31 report the number of events with a strip multiplicity $> N_h$ for both cases of an energy distribution as given by the curve (1) or curve (2). A threshold effect is seen below about $N_h = 1000$, due to the fact that at these events also showers with energies $< 5\ TeV$, not sampled in this simulation, can contribute. On the other hand, showers with energies less than about 20 TeV do not contribute to events with $N_h > 1000$. The limited statistics and the energy cut-off $E_{max} = 400\,TeV$ of the sampled energy distributions affect the tail of the distributions. Thus, the frequency distribution in the range $\Delta N_h = 10^3 \div 10^4$ are well appropriate to represent the proton spectrum from a minimum energy of 20 TeV up to about 200 TeV.

4. the frequency distribution of the fired strips corresponding to the extreme cases of curve (1) and curve (2) are clearly distinct concerning either the total number of events as well as the slope. We note that the spectral index γ_h which can be deduced from the frequency distribution is smaller than the spectral index γ_p of the sampled primary spectrum, mainly due to the dependence of the size N_e on energy, $N_e \sim E^{1+\epsilon}$, and since the fraction $N_h(5-25)/N_e$ (or $N_h(5-50)/N_e$ for ARGO) increases with energy. We find from this simulation $\gamma_h \sim \gamma_p/1.12$.

From these results it appears that the measurement of the frequency of events as a function of the strip multiplicity provide a powerful tool to investigate both the absolute flux and the energy distribution of the primary protons from about $10 \div 20\ TeV$ up to $200\ TeV$ at least. In order to assess an absolute relation between the measured frequency distribution of strips and the primary proton spectrum a more refined simulation has to be performed according to the following prescriptions:

a) the energy interval of sampled showers must be increased for a better determination of the overall spectrum

b) electrons and photons must be followed down to 1 MeV threshold energy

c) a multi-hit correction has to be applied for a more accurate simulation of the detector response. This correction is due to the probability – typically 20%, but depending on the working point of the RPCs – of having a two-strips signal for each particle crossing the detector

d) the contribution to the strip multiplicity distribution from helium induced showers has to be taken into account. From preliminary simulations this contribution is estimated less than 20% since at a given energy per nucleus the size of helium induced showers is noticeably smaller than that of proton induced showers and exhibits a flatter lateral distribution. Thus uncertainties in this correction are expected not to spoil the relation between the absolute proton spectrum and the frequency distribution of the hit multiplicity.

2.7 SOLAR AND HELIOSPHERE PHYSICS

2.7.1 Cosmic Ray Modulations

The inclusive trigger LMT($\geq$ 6) provide the opportunity of detecting showers produced by low energy protons down to the geomagnetic cut-off. Despite of the low effective area for proton induced showers of a few tens GeV, more than $10^4\ ev/sec\ sr$ are expected for ARGO and about $4 \times 10^3\ ev/sec\ sr$ for ARGO-3600 at zenith angles less than 35^o. In fact, ARGO (ARGO-3600) has for $10\ GeV$ protons a geometrical factor $\sim 10^5\ cm^2\ sr$ ($1.5 \times 10^4\ cm^2\ sr$), increasing up to $6 \times 10^6\ cm^2\ sr$ ($10^6\ cm^2\ sr$) for protons of $50\ GeV$. In Table 2.6 a comparison with other ground-based detector dedicated to the study of cosmic ray modulations shows the potential of ARGO to investigate spatial and temporal variations in an energy range only marginally explored. The selection LMT(6-10) defines a primary proton beam with a median energy of 100 GeV, see fig.2.32, and with a threshold of about 10 GeV as defined by the local rigidity. The estimated rate of events detected in a cone of 10 degrees half angle is about 720 ev/sec for ARGO and about 250 ev/sec for ARGO-3600.In every selected angular bin ARGO-3600 may integrate about 8×10^4 showers per hour, half of them coming from primary protons with energies $< 100\ GeV$. Thus, it will possible to study cosmic ray modulations in well defined asymptotic directions on time scales of a fraction of day and sensitivity to fluctuations of amplitude less than 1%. Assuming a mean IMF of about 6 nT the gyroradius of a 50 GeV proton is about 0.15 A.U. . For a wind with a radial velocity of 400 km/sec this corresponds to a typical frequency of 20 μHz. Therefore, effects due to

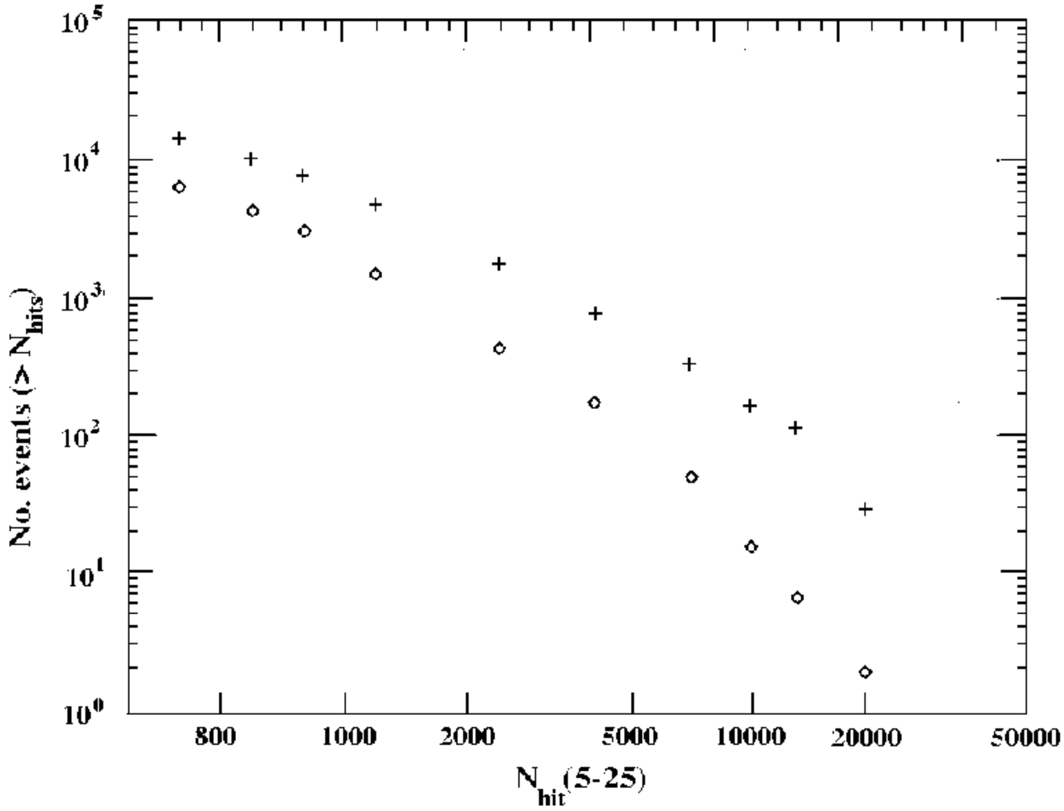

Figure 2.30: The integral frequency distribution of events as a function of the number of fired strips at a distance interval $\Delta R = 5 \div 25\ m$ from shower core. The two distributions upper and lower correspond respectively to the curves (2) and (1) of fig. 1.17

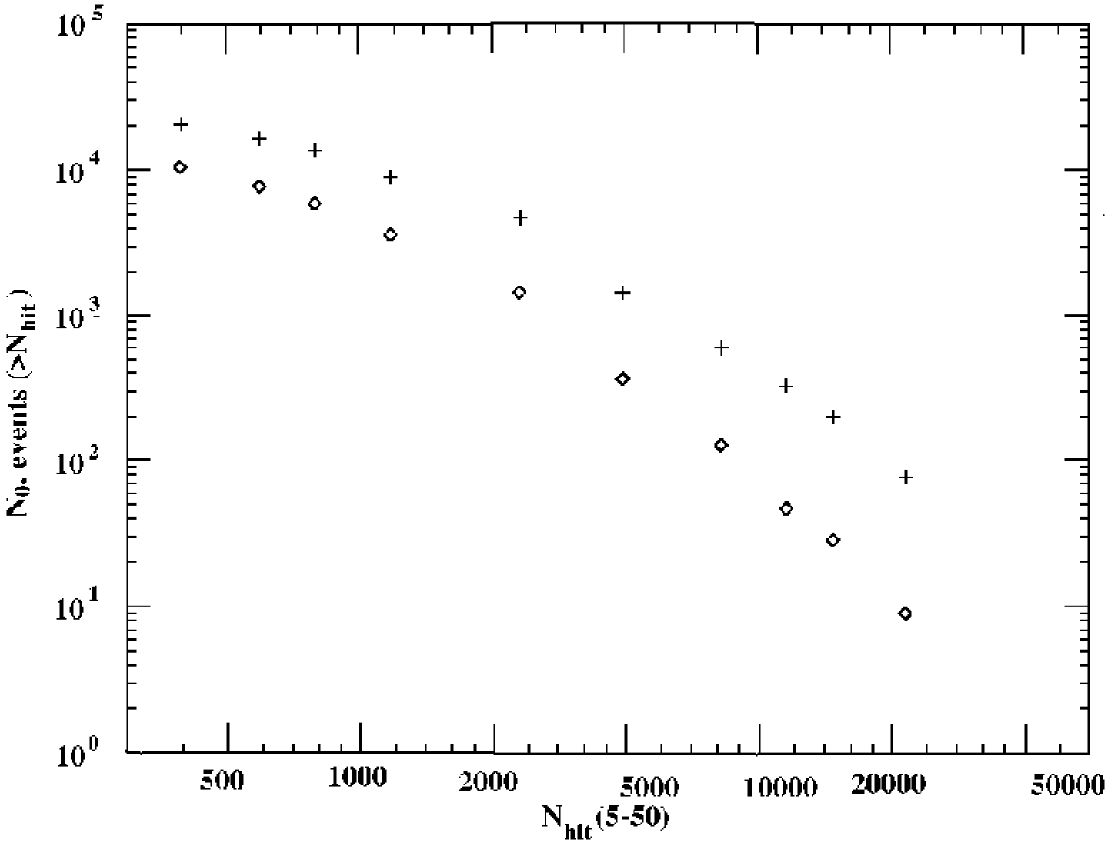

Figure 2.31: The integral frequency distribution of events as a function of the number of fired strips at a distance interval $\Delta R = 5 \div 50\ m$ from shower core. The two distributions upper and lower correspond respectively to the curves (2) and (1) of fig. 1.17

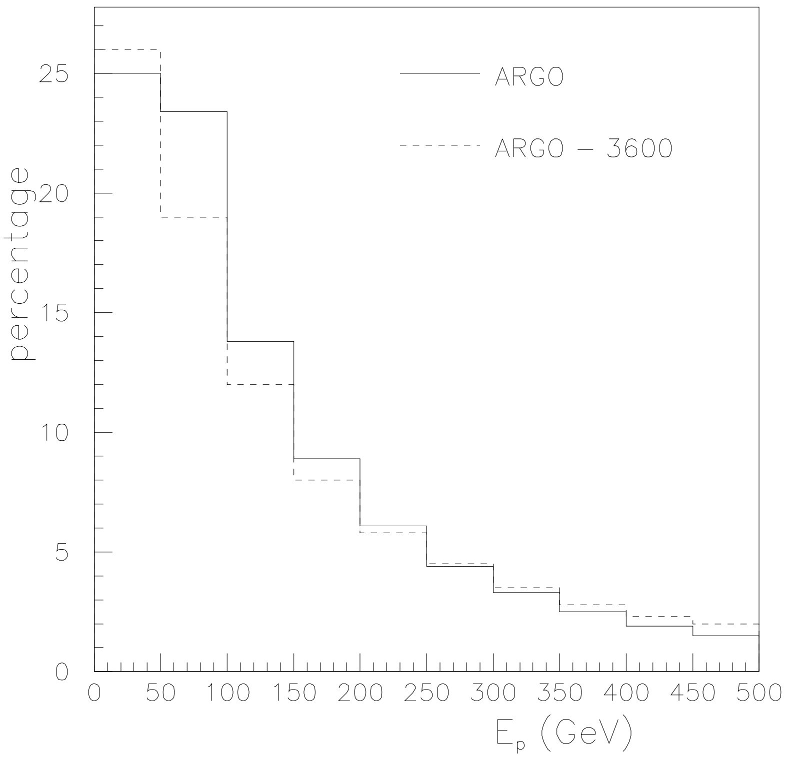

Figure 2.32: The energy distribution of primary protons sampled by means of the LMT(6–10) selection at zenith angles $\theta < 35^o$

modulations at frequencies on the tail of the range expected for solar g-mode oscillations could be explored looking at well defined directions in the heliosphere. Moreover,integrating in a solid angle with 25 degrees aperture a counting rate of 2.4×10^5 ev/hr can be achieved by ARGO-3600, allowing to investigate the presence of spectral components down to 100 μHz. In fig.1.26 the power spectrum of time series from the Mt.Norikura air shower experiment ($E_{min} = 5\ TeV$) and from the underground stations of Matsushiro ($E_{min} = 300\ GeV$) and Sakashita($E_{min} = 100\ GeV$) are shown. The sharp spikes due to the diurnal, semidiurnal and tridurnial variations produced by anisotropies of both interplanetary and galactic origin are visible in the power spectrum of Sakashita. ARGO-3600 will operate to a substantial lower threshold energy with increased sensitivity to high frequency modulations.

2.7.2 Solar Flares

γ–flares

Gamma rays flares are produced in the nuclear interactions between accelerated particles and the ambient solar atmosphere. They can provide information on the accelerated particle spectra, acceleration mechanisms,trapping of parent particles etc. Imaging gamma-ray telescopes, like SAS-2 or COS-B, have never been directed towards the Sun, either due to a lack of solar activity during the mission or due to attitude constraints. The detection for the first time of gamma rays with GeV energies has been accomplished by EGRET and GAMMA-1 satellite born experiments. Both experiments are not dedicated to the Sun observation,neither solar missions are foreseen with detectors sensible to high energy gamma rays. In this respect ARGO could provide a good opportunity of monitoring Sun activity in high energy photons.In order to assess its sensitivity, the fluxes of the three intense gamma flares detected on March 26 and June 15,1991 (GAMMA-1,[74]) and June 11,1991 (EGRET, [75]) have been used extending the photon spectrum up to 30 GeV. The selection LMT(6-20) has been applied.We find that only a short impulsive flare as the March 26 event should have induced a marginal increase of the counting rate in the Sun direction. This low sensitivity is due to the very steep spectrum of these events ($\gamma = 3 \div 4$). A straightforward calculation allows to define the minimum intensity of a flare detection to a 3σ significativity level, provided that the spectrum extends up to 30 GeV at least. Assuming the flare follows a power law E^{-3}, the minimum detectable flux is given by

$$J_\gamma(E) = 2 \times 10^3 \sqrt{\frac{10}{\Delta T(sec.)}} E_{MeV}^{-3} \quad ph \cdot cm^{-2} s^{-1} MeV^{-1}$$

being ΔT the time duration of the signal. A factor 2.5 has to be taken into account in predicting the ARGO-3600 sensitivity. While high energy gamma ray flares of this intensity have never been observed, the possibility that they are produced and not observed with the sensitivity of present satellites cannot be discounted. Therefore it is of great importance the monitoring of the Sun during a period including the phase of the maximum solar activity.

Neutron flares

Observations of interplanetary neutrons from solar flares have been carried out by three methods: direct detection of neutrons in space, detection of their decay protons or electrons in space, and ground-based detection of neutrons. These methods provide complementary information on the spectrum, angular and temporal distributions of escaping neutrons in different energy ranges, which can be compared with theoretical predictions to constrain models of high-energy processes in solar flares.

The ARGO detection capability of low energy hadrons provide an other ground based methods to observe these flares. Assuming a neutron spectrum $\sim E^{-3}$, the minimum detectable flux is given by

$$J_n(E) = 1.8 \cdot 10^4 \sqrt{\frac{10}{\Delta T}} \cdot E_M^{-3} \quad neutrons \quad cm^{-2}s^{-1}MeV^{-1}$$

This flux can be compared to the neutron flux observed on 4 June 1991 by the Akeno Giant Air Shower Array (AGASA), 900 m above sea level. The excess counting rate detected by the scintillation detectors of this array has been attribute to showers induced by neutrons arriving along a straight trajectory from the Sun. The duration of the signal was more than 20 minutes and the estimated flux of solar neutrons above 10 GeV was about $1 \div 2\, m^{-2} \cdot s^{-1}$ at the top of the atmosphere.
We note that

i) ARGO may point to the Sun while no reconstruction of the direction is allowed in the Akeno measurements,

ii) the limiting flux of ARGO for a flares lasting for 20 minutes is about 0.1 $neutrons\ m^{-2} \cdot s^{-1}$, that is a factor of 10 less than the intensity observed by Akeno. Such a flare should have been observed with high statistical significance also by ARGO-3600.

2.7.3 The Monitoring of the IMF

The yearly variation of the position of the Sun shadow has been observed by the AS-γ experiment in Tibet, fig1.19. The observed displacement of the Sun shadow is interpreted as due to the combined effect of the magnetic fields of the Sun, interplanetary space and Earth. The effect of the IMF would be larger than that of the geomagnetic or solar magnetic fields. One can estimates an effective value for the IMF integral about 4-5 times the geomagnetic field integral. The IMF has a sector structure and a 'garden-hose' topology with the field direction reversing across the sector boundary, fig 2.33. A current sheet separates field lines of opposite polarity near the equator. Since the current sheet, which rotates with the Sun, is inclined to the solar equator, a ground based detector observes successive periods of inward and outward pointing magnetic field vectors, depending on whether it is above or below the sheet. As solar activity approaches minimum levels, the current sheet becomes nearly equatorial. However, when the Sun is active, effects of changes in the solar wind velocity and the solar magnetic field polarity will produce a large disordered magnetic field. Local

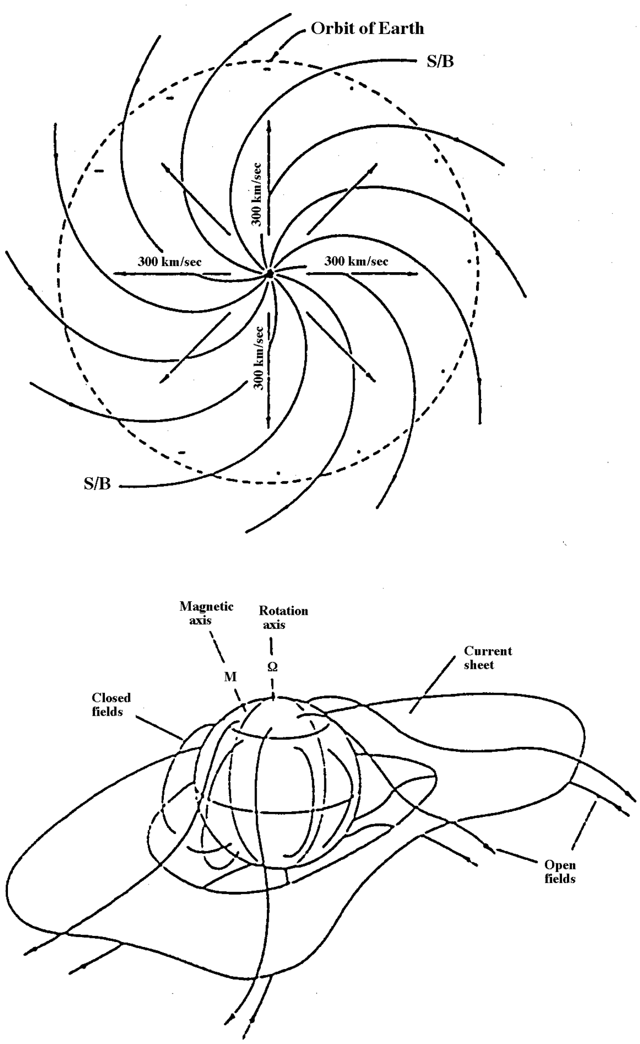

Figure 2.33: The IMF viewed in the solar equatorial plane (top). The current sheet near the sun in three dimensions (bottom).

fluctuations equal in magnitude to the average field strength, $\Delta B/B \simeq 1$, have been found. Thus, it will be of a great value to study these phenomena in periods including the phase of the maximum of the solar activity when the reversing of the Sun magnetic field is expected.

The first direct observation of the magnetic field effects on the cosmic ray shadows by the Sun has been performed by the AS–γ Tibet array. However, due to the high threshold energy, data have been folded over long periods (several month).

ARGO has the advantage of observing the Sun shadow at 1 TeV energies with high angular resolution.So we expect to detect a well displaced shadow in quite short times.Simulations have been carried out for ARGO-3600.The profile of the 'deficit' for 150 hours of data taking (about one solar rotation) is shown in Fig.2.34. Here Θ_x is the displacement along the East-West direction. A primary beam as defined by the HMT(>30) selection has been considered. The effect of the IMF is described by assuming a bending power of 500 Tesla-m.The number of shadowed events in the angular box $\Theta_y = \pm 0.3^o$, $\Theta_x = 0 \div 10^o$ is about 2700. This corresponds to a 7σ effect only from counting the number of missing events. Thus a time observation corresponding to about 10–15 days of summer runs, should be sufficient to detect the shadow with $4 \div 5\sigma$ significance. To define the position of the displacement a detailed analysis of the shape of the shadow is needed. A rough estimate obtained from these preliminary results is that ARGO-3600 could monitor the position of the Sun shadow with sensitivity to 20% variations of the large scale structure of the solar and interplanetary magnetic fields on a time basis as short as two weeks or less. Therefore ARGO–3600 should be able to get information on the time dependence of the large–scale structure of the solar and interplanetary magnetic fields an their relations to the cycle of the solar activity.

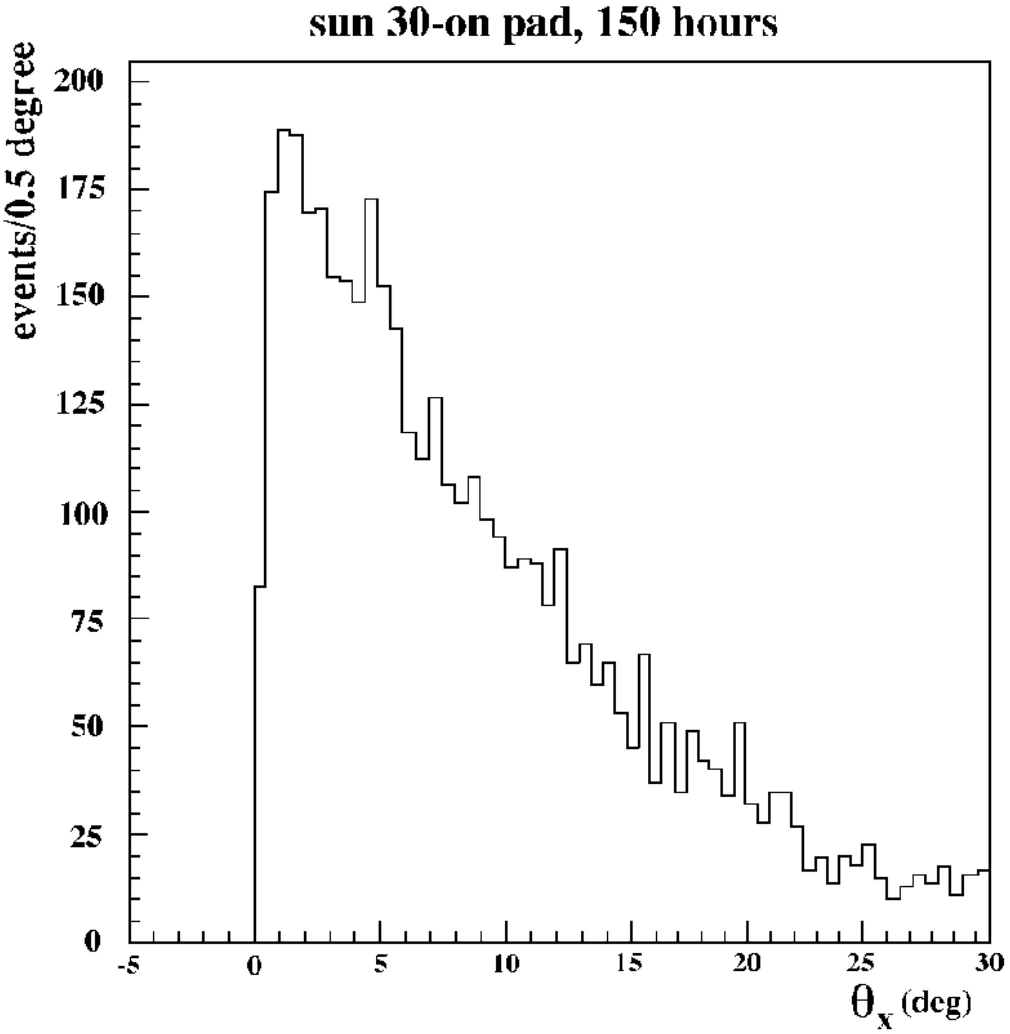

Figure 2.34: The deficit event density along the right ascension as a function of the angle distance from the Sun center.

Table 2.1: Event classification

	CORE RECONSTRUCTION	
NUMBER OF PADS	NO	YES
6-10	LMT	
11-20	LMT	
> 20	HMT/LR	HMT

Table 2.2: Figure of Merit R_γ

$E(GeV)$	ARGO	ARGO–3600
100	3.4	4.6
300	2.4	3.0
500	2.0	2.4
700	1.8	2.4

Table 2.3: Time of observation for a 5σ signal from Crab by different pad selections (ARGO).

ΔN_p(pads)	20-50	50-150	150-250	> 20	> 250
$E_m, E_{th}(GeV)$	150	350	900	100	1000
T(days)	14	13	50	7	15
N_γ(1 yr)	38000	18300	4600	64750	3850

Table 2.4: Time of observation for a 5σ signal from Crab by different pad selections (ARGO–3600).

ΔN_p(pads)	20-50	50-150	150-250	> 20	> 250
$E_m, E_{th}(GeV)$	150	350	900	100	1000
T(days)	60	60	250	30	90
N_γ(1 yr)	5900	2300	700	9350	450

Table 2.5: SNRs detected by EGRET

SNR	$\delta(^o)$	Angular Size (deg)	$\Phi_\gamma(> 100MeV)/10^{-7}$ $(cm^2\ s^{-1})$
W63	+45 20	1.3	1.5
γCygni	+40 14	1.0	13.4
IC443	+22 36	0.8	4.3
W44	+01 18	0.5	7.4
W51	+14 00	0.4	2.0
Monoceros	+06 30	3.0	2.2

Station	Counter type	Location		Detector characteristics			Total count. rate	Minimum primary energy	Spread of asympt. directions for each telescope
		Altitude (m)	m.w.e	Area (m^2)	N. of telescope	Angular resol.	(c/h)	(GeV)	
Mawson	P.C.	s.l.	30	8	>6	30	3.510^5	50	40 -90
Embudo	Sc.	2600	27	4	5	30-45	3.310^5	40	40 -90
Socorro	Sc	1500	74	4	4	30-45	710^4	100	40 -90
Misato	Sc.	s.l.	34	36	10	20-40	1.410^6	50	40 -90
Sakashita	Sc.	300	80	36	10	20-40	$5 \cdot 10^5$	100	40 -90
Matsushiro	Sc.		220	25	16	20-40	10^5	300	40 -90
Nagoya	Sc.	s.l.		36	16	20-40	10^7	10	60 -120
Moscow	μ Hodosc.	s.l.		9	-	1-2	$3.6 \cdot 10^6$	9	20 -60
Milagro	Cerenkov	2500		5000	-				
Argo 3600	RPC	4300		3600	-	<5	10^7	$10^{(*)}$	15 -35
Argo	RPC	4300		$1.5\ 10^4$	-	<4	$3 \cdot 10^7$	$10^{(*)}$	15 -35
($*$) with the estimate of the individual energies									

Table 2.6: Large experiments for studies on the cosmic ray modulation.

Chapter 3

THE DETECTOR

In this chapter we describe the ARGO detector. Technical details will be given with special emphasis for ARGO–3600. The Gas distribution System with an eventual closed circuit option, High Voltage System, and the Data Acquisition System will be exposed. Finally we describe the tests performed on a small array of RPC's and on the performances of the RPC as a function of temperature and atmospheric pressure.

3.1 INTRODUCTION

The ARGO detector is conceived to take the maximum advantage from the RPCs (fig.3.1)performance. It fulfills the following basic requirements.

1. Highest space-time resolution for the EAS pattern detection
2. Adequate granularity to fulfill point 1 at an acceptable cost
3. Detection capability for very high hits densities as expected at the shower core position
4. Excellent triggering capabilities even for low energy showers and for showers with the core falling outside of the detector
5. Coverage near to 100% i.e. minimum uncovered space around each RPC module
6. Very simple and robust assembling and mounting to achieve high long term stability while reducing to the minimum the cost of extra mechanical parts, supports etc, not strictly included in the detector
7. Very simple High Voltage and Gas systems while keeping a reasonable segmentation and control of different parts of the detector
8. Easy access to any part of the detector not only during the mounting but also during the data taking.

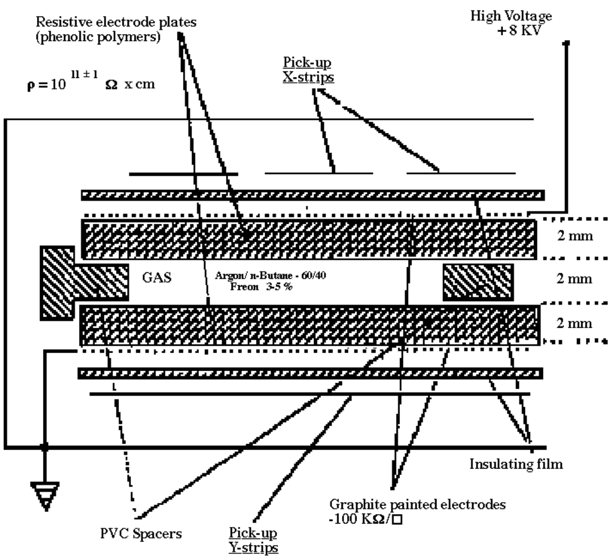

Figure 3.1: Schematic view of a RPC cross section

9. High performance of the front–end electronics giving the maximum emphasis to the detector potentialities of space and time resolution
10. Minimum number of cables connecting different parts of the detector by requiring very fast data transmission channels sending the data to a central trigger and data taking station
11. Minimum data acquisition dead time to look for time correlations between consecutive events down to tenths of nanosecond scale

The detector will to be installed inside a building giving protection against rain, snow, strong wind and extreme temperatures. The temperature effect on the RPCs will be described below.

3.2 DETECTOR LAY–OUT

The detector is a squared array of 4840 RPC modules of size $1.12 \times 2.80 m^2$ disposed as 44 lines of 110 modules each as shown in fig. 3.2. For the first phase of the experiment, ARGO–3600, we plan to use 1071 RPCs in 21 lines each of 51 modules. Around each module there is some uncovered space to allow for the gas, high and low voltage distribution systems as well as for the cable interconnections among different modules. The uncovered space is 12 and 5

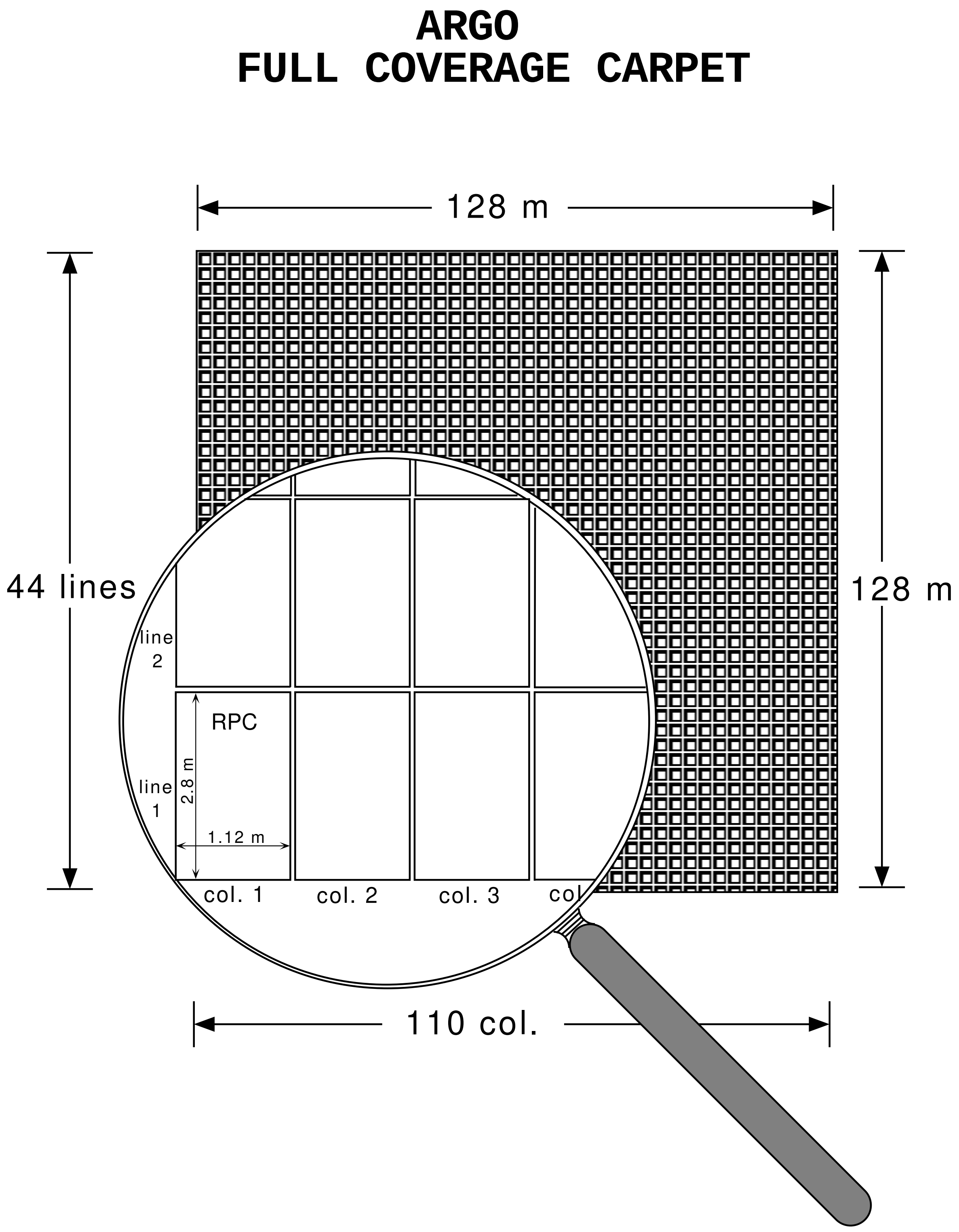

Figure 3.2: ARGO lay–out

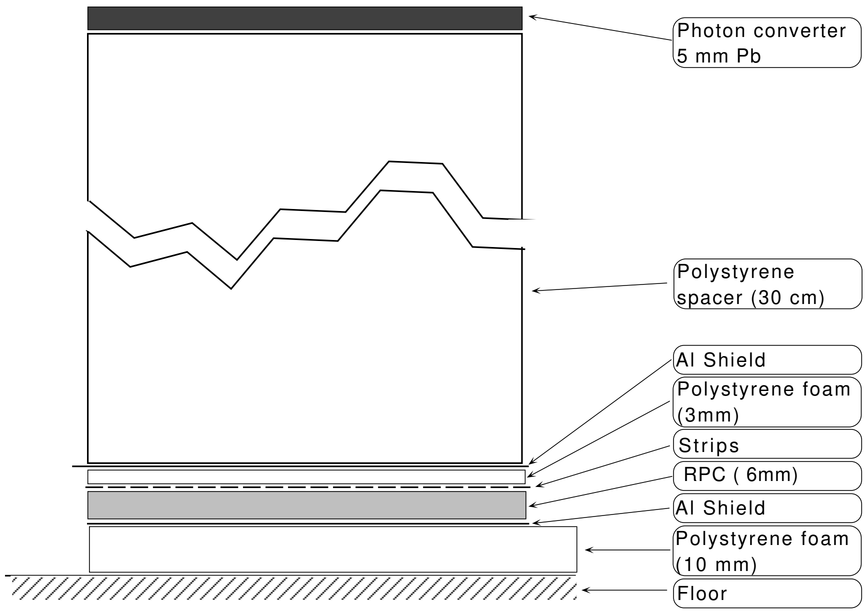

Figure 3.3: Cross Section of the detector set–up

cm along the $2.8m$ and $1.12m$ sides respectively. The carpet covers an area of $128 \times 128m^2$ with an active area of $15,000\ m^2$ corresponding to a coverage ratio of about 90%. It is organised in stations composed of a RPC module, a plane of signal pick up strips, two thin grounded aluminium foils shielding both faces of the detector, an expanded polystyrene plate which avoids the direct contact of the RPC modules with the floor, a lead plate working as a photon converter and a very light polystyrene foam holding the lead converter at 30 cm above the detector which allows an appropriate separation of the e^+ e^- pairs produced by the gamma photon conversion. All these elements are not glued or rigidly connected; they are just superposed to one another and slightly pressed by the weight of the lead plates. This eliminates the need for extra mechanical work or mounting parts. Moreover it guarantees an excellent regularity for the detector geometry if a reasonable flatness floor and good quality polystyrene plates are provided. The cross section of the detector set up is shown in fig. 3.3

The RPC module is placed over a polystyrene rigid foam plate 1 cm thick put on the floor. A 50μ thick aluminium foil inserted between the plate and the RPC and connected to ground shields the lower face of the RPC. The read out strips, glued on a polythene/PVC film, are placed in contact with the upper face of the RPC. A rigid foam polystyrene plate 3 mm thick is sandwiched between the polythene film holding the strips and a second grounded aluminium foil shielding the upper face of the chamber. This quite rigid sandwich structure includes also the front–end boards that are fixed at its edges. It will be called "read out plate" in the following. On top of it a very light polystyrene layer 30 cm thick holds the photon converter which is made of $28 \times 28\ cm^2$ lead plates $5mm$ thick. The polystyrene

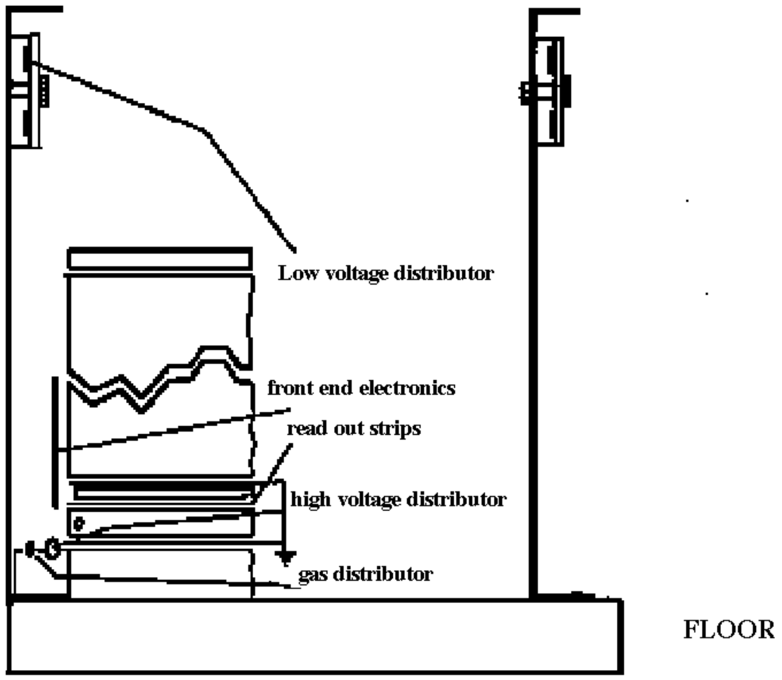

Figure 3.4: Connection of the Front–End electronics to the RPC in the "I" shaped corridors

spacer is essentially a box filled with standard materials normally produced by the packaging industry. Its density is about 15 kg/m^3. Each RPC module is read out by 160 aluminium strips of 56 cm long 33 mm wide with 3.5 mm pitch running parallel to the 1.12 m side of the module which are connected to the front–end electronics at the edge of the RPC as shown in fig. 3.4

Five front–end boards are fixed along each 2.80 m side of the RPC. Each board is connected to 16 strips and gives the "FAST OR" of the signals, which is used for triggering and timing, as well as the serial and parallel read out. The front–end electronics is described below. The maximum signal delay due to the propagation of the pulse along the 56 cm long strip is 2.5 ns. This delay introduces a time jitter of 0.7 ns sigma that has to be added in quadrature to the intrinsic time jitter of the detector. The RPC array is divided in "corridors" by "I" shaped iron bars 123 m long as shown in fig3.4, running parallel to the "columns" of the array. The purpose of the iron bars is twofold. They are used to support the signal cables connecting different RPCs as well as the "services" distribution systems i.e. gas, high and low voltage. Moreover they are also used as rails to allow a few chariots of proper size to scan all the surface of the array for supporting the construction, calibration and initial test of the detector. These chariots moving on rails are the normal way to reach any point of the detector thus avoiding the use of a floating floor. The chariots are equipped with all the instruments needed for mounting the detector. They are used to install the RPC modules, the lead plates, the read out plates already equipped with the front–end boards. Groups of 3 modules are organized in superstations. The purpose of the superstations is to provide an intermediate granularity structures between the single RPC and the whole detector. Its "local" information is treated before to be sent to the central controller that has the purpose of correlating different superstations. All the chambers of the same superstation are connected via coaxial cable to a local superstation controller that performs:

- " FAST OR" of the superstation
- Multiplicity
- Time to digital conversions
- Control of the front–end
- Transmission of the information to the central station.

The information is transmitted via optical cable (fiber) to the central controller. The superstation controller memorizes and transmits all the information generated in the detector.

3.3 GAS SYSTEM

The gas system is conceived in such a way to balance the simplicity with the need of a high segmentation which allows a detailed control of the system. The minimum "gas channel" is made of four RPC's, serially fluxed as shown in fig.3.5

The gas distribution system consists of 13 gas distributors and 13 gas collectors 100 m long and of adequately large internal section running through the full length of the detector (see fig3.5). Each distributor (collector) serves the RPCs of 8 corridors, four at the right side and four at the left. Each gas channel is connected at opposite ends to a gas distributor and collector respectively. The architecture of the system makes the connections extremely short so as to avoid the need of a large number af long tubes. A gas channel is controlled and monitored by the following elements:

1. A manual valve at the inlet connection that can eventually stop any gas flux through the channel
2. A capillary pipe, also at the gas inlet, of much higher impedance with respect to that of the gas channel i.e. essentially the four chambers serially fluxed. In this way the gas flow through the channel is only determined by the impedance of the capillary pipe so that the flow can be made extremely uniform in all the channels provided that a set of well calibrated and identical pipes are used.

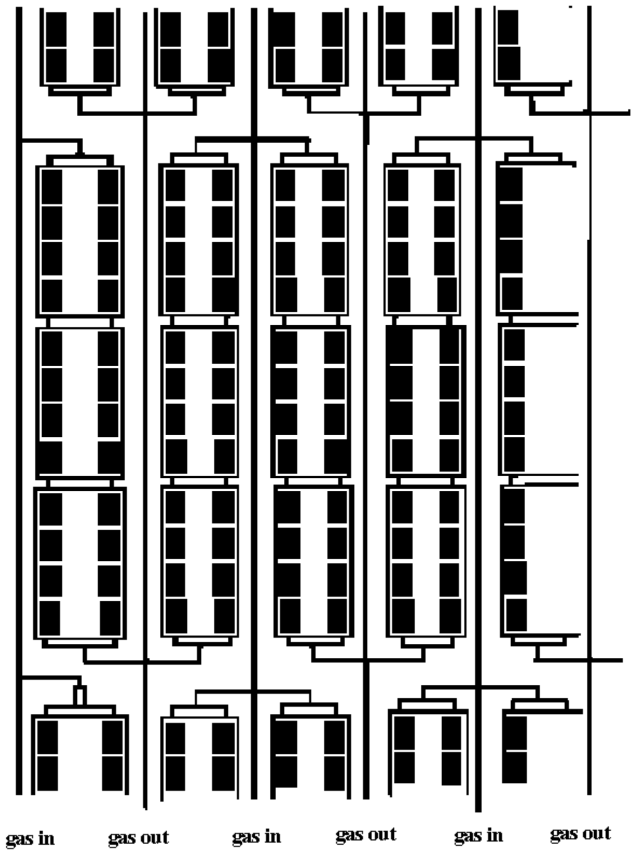

Figure 3.5: Gas distribution in ARGO

3. A remote controlled bubbler at the outlet connection is used to monitor the gas flow and to detect eventual leaks. Plexiglass bubblers are used to avoid fragility. An acoustical or optical sensor is used for the remote control which is connected with standard twisted pairs cables to a central gas control system located in the counting room.

One possibility that we are investigating is that the gas already used is not dispersed in the atmosphere but is circulated inside a closed circuit and purified. The need for such a system is suggested mainly by economical and ecological reasons connected to the use of a very large detector over very long running times. Nevertheless it should be stressed that according to the experience accumulated so far, the gas purity requirements for RPCs are very modest.

The circulation/purification system consists of:

- one (two) gas analyzer to check the concentration of the components for a binary (ternary) gas mixture
- an oxygen analyzer to check possible air contamination
- one or a few filters to remove impurities like oxygen...

The system capacity is about $60m^3/day$ corresponding to three gas recirculations/day. Small amounts of fresh gas are periodically introduced in the circuit by a mixing station consisting of two (three) standard mass flow–meters and the relative control unit. The performance of the gas system is computer monitored via CAMAC interface.

3.4 HIGH VOLTAGE SYSTEM

The need to combine simplicity and high segmentation concerns the high voltage as well as the gas system. The high voltage distribution system is sketched in fig 3.6. A high voltage line feeds two contiguous corridors in parallel. The line, a standard coaxial cable, is divided in segments 2 m long i.e. the same dimension of the chambers. At each row of chambers the line has a three way connection that is used to branch two chambers, one in each corridor as is indicated in fig 3.6 and the following segment, so that the line can be interrupted in correspondence of each of the 50 rows of the array. This makes very fast the search of possible failures of the system . The rails separating the corridors are also used as ground connections for the high voltage and, as for the high voltage line, a rail serves two contiguous corridors so that odd number corridors, starting from the left in fig 3.6, are used to support the high voltage lines and even number corridors as ground connections. Each line is connected to a power supply of maximum voltage 10 KV and maximum current $2mA$, a largely dimensioned value as the current required by 100 chambers served by the line should range around $.5mA$. Low cost high voltage connectors of aluminium or copper coated plastic, specially developed for large scale applications, will be used. A total number of 50 supplies are required for the array. The system is computer monitored via a CAMAC interface that continuously checks the voltage and the current of each supply. If very large

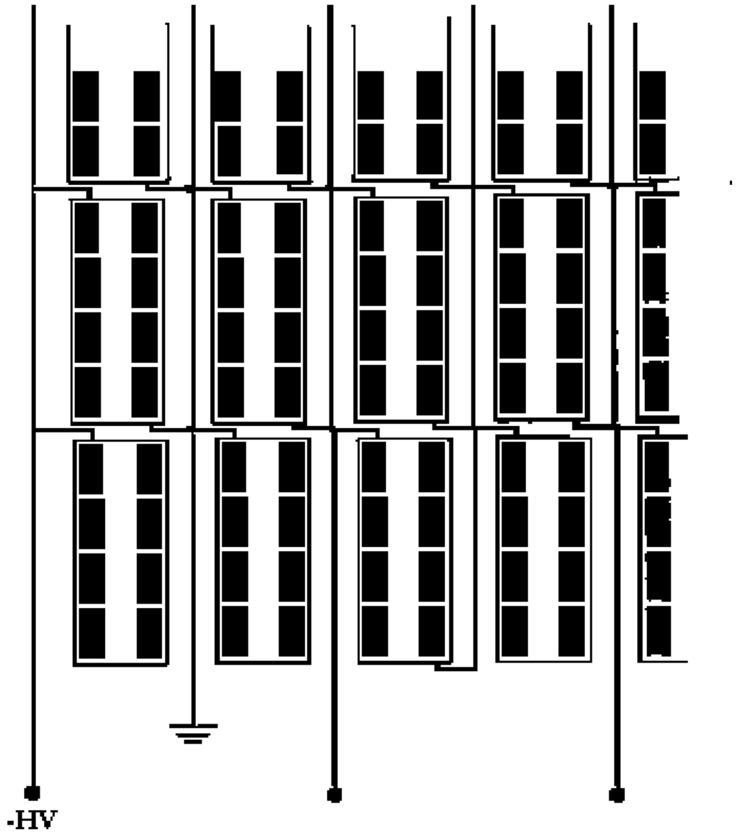

Figure 3.6: The high voltage distribution system for the ARGO detector

temperature and/or atmospheric pressure changes are foreseen, for example $\delta T = \pm 10\ ^{\circ}C$ and $\delta P = \pm 30\ mBar$, the detector working point can be maintained stable by proper continuous corrections of the operating voltage. In this case a temperature and pressure monitor is also needed which can be integrated together with CAMAC voltage control system. It should be stressed that such a control system of the detector working point is not used in current RPC apparata but in this particular case it may be useful to avoid even minor changes of the time resolution.

3.5 THE DAQ SYSTEM

The Data Aquisition system must collect and manage all the information generated in the detector consisting in $10,710$ PAD ($56 \times 56 cm^2$). It can be subdivided in three parts

1. front-end electronics
2. trigger system
3. event buffer and reconstruction

3.5.1 Front End Electronics

The front end electronics is an improved, completely new version of the RPC dedicated circuit which was developed almost 10 years ago. It takes fully into account the enormous experience that has been accumulated so far in the course of all the experiments which used RPC's as a fundamental part of the detector.

The existing front-end card is built on a $50 \times 20\ cm^2$ board and uses fast transistors and TTL/AS integrated circuits. It contains 16 discrimination channels of threshold about $50\ mV$, a "FAST OR" output, serial and parallel read-out. The "FAST OR" output has the same delay, 10 ns, with respect to all the input channels so that it can be used for time of flight measurements. The front-end electronics of the RPC's for ARGO is a surface mounting version of the existing one and will also contain the necessary circuitry for the multiplicity measurements, a specific requirement for the gamma-ray astronomy. The surface mounting technology offers the following advantages with respect to the ordinary one:

1. It is more compact and gives a factor of 4 gain in the number of channels for fixed area of the board.
2. It allows a much less inductive wiring thus improving the quality of the circuit at high frequency.
3. It is more suitable for serial production.

In the following we will describe the electronics that we plan to use for ARGO–3600. Future R/D in the detector electronics can give more effective and economic solutions. The front end electronics consists of 10710 boards 16 channels each. On this board each detector

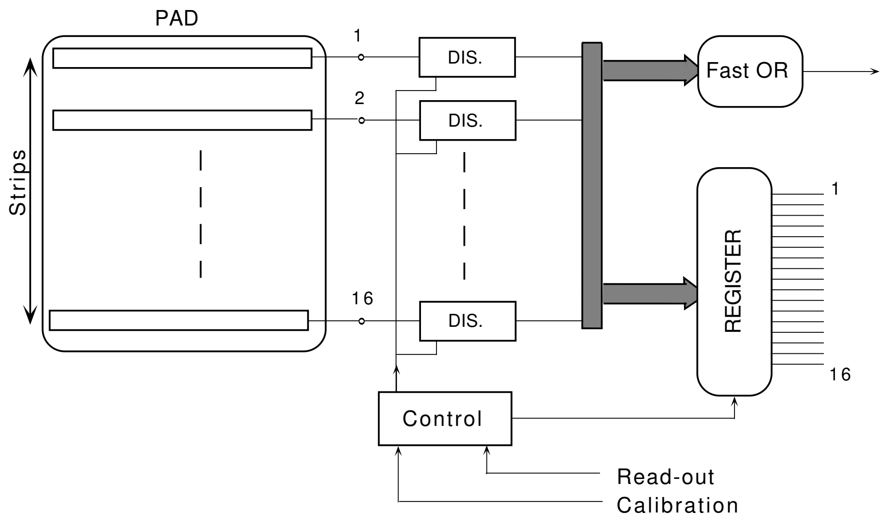

Figure 3.7: Scheme of the Front–End electronics

strip is connected to the discriminator–shaper via connections which have the same length. All the information of the strips is sent to a 16 bit register and to a " FAST OR" (fig. 3.7). The output of this FAST OR is used to perform the trigger.

Each RPC chamber ($112 \times 280 cm^2$) comprises 10 PAD's. In order to optimize the acquisition logic it has been decided to group all the information of 3 chambers (30 PAD's) in a substation (Mother), called PADM, placed nearby the 3 chambers themself. In this substation, see fig3.8, the information coming from the 30 FAST OR's are sent to a 32 channels multi–hit TDC with a time resolution of 1 ns and a 16 bit dynamic range. All the connecting cables will have equal length. In each substation a weighted sum of the signals is produced in order to provide a fast signal for the formation of the *multiplicity trigger*: This signals are sent to the central station. The Control Circuit, when a single or several FAST-OR are present, starts to transfer either the content of the registers associated to each firing PAD end the corresponding time information. All the generated information is transmitted.

The data are transferred with a link working at ~ 1 $Gbit/s$. The characteristic of such transmission line permits to calculate the dead time. In the worst case signals are generated in all the PAD's. In this case the *Busy* time of the line is ~ 2 μs. Since the rate of a PADM is expected to be less than 10 kHz, then the resulting dead time, in this extreme case, does not exceed ~ 2 %.

3.5.2 Trigger System and station interconnections.

All the information of the detector is sent to a central station by the PADM electronics via 400 links. Therefore we can choose the delay time τ for the transfer of the data from a PADM

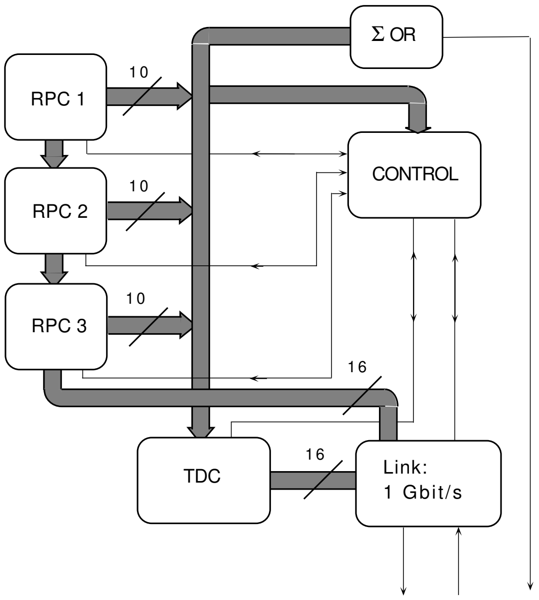

Figure 3.8: Scheme of the PADM electronics

respect to the corresponding FAST OR signals (see fig3.9). With the 400 weighted FAST OR signals we create the trigger signal by requiring a multiplicity $\geq n$ within a time window corresponding to the maximum delay among the particles belonging to the same shower. This time window turns out to be $\sim 400\ ns$ corresponding to the dimensions $(60 \times 60\ m^2)$ of the apparatus and the maximum incident accepted angle of the shower. The time formation of the multiplicity trigger is performed within $\sim 200\ ns$. We fix τ so that the data will arrive to the central station when the trigger decision is ready. The data will be memorized or not according to the trigger status.

The electronics of each sub–station is connected to a central control station through a multimodal optical fiber. All the fibers have the same length, about 100 m to preserve the physical time sequence of the signals at the central station. The same fiber could be used to send control signals from the central station to the sub–station. The signal attenuation for a 100m long fiber is about 1db. The trigger circuitry is contained inside the central controller. The trigger consists in a cascade of modules; each module performs the analog sum of 16 weighted FAST OR signals generated in a 4×4 PADM electronics corresponding to a square part of the detector. Taking into account that the required multiplicity is low, on the output of the sum–modules the voltage step per hit is quite once when a voltage full range is fixed. This fact permits to find–out a design of the analog sum module with variable time shaping to obtain, at minimum cost, the optimization of the trigger from an operative point of view. If the trigger decision is positive, the modules that memorize the information coming from the PADM electronics (fig. 3.9) has to perform the following operations:

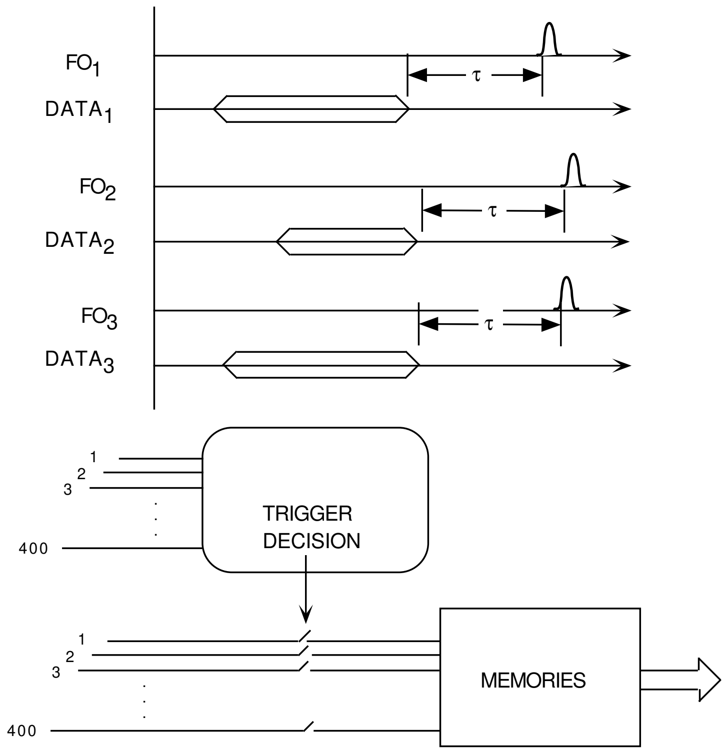

Figure 3.9: The basic Trigger logic

- For each link a Flip–Flop has to be set if data are present and accepted. This information will be read by the event builder together with the absolute time information.
- All the modules have to send to the front–end electronics all the information regarding the channel calibration, tests and time setting for the TDC's.
- Reconstruction of the total multiplicity for monitoring purpose.

3.5.3 Connection between Trigger and Event Builder

All the data selected by the trigger are then sent to the Event Builder which collects them via the DI/O input block using a point to point connection ($\approx$ 400 input channels). The mechanism of this transmission is asynchronous. In fact, after the data selection, the trigger changes the status of flags corresponding to the channels which contain the useful information, enabling the DI/O section to acquire the selected data. This structure is only slightly complicated by the introduction of a memory block before the DI/O section. This memory block is necessary to adapt the acquisition speed of the DI/O and the data flow coming from the apparatus. In fact, it is possible to have a large quantity of data for short times and it is necessary to bufferize this information (see next section).

3.6 EVENT BUILDER AND STORAGE SYSTEM

The Event Builder and Storage System collects and stores all the events detected by the apparatus, acquired by the front/end electronics and selected by the trigger. These data are first formatted within a frame structure with an header which contains information on the data contained in the frame (temporal, length, etc.), then are stored on tapes (off-line analysis) and eventually on disks (buffer disks for data storage, on-line checks of the system and on-line analysis), allowing any eventual full retrieval and reprocessing of the original data. For safety reasons, the system makes two copies of these data.

3.6.1 Specifications

Taking into account that each mother pad is made of 30 pads each consisting of 16 strips, then the number of independent acquisition channels for the Event Builder and Storage System is ≈ 400. The basic structure of the information flowing through each channel consists of two 32-bit words for each pad. The first word contains the pad address (16 bits) and the time information (16 bits), while the second one contains again the pad address (16 bits) and the strip values (on-off) (16 bits). Therefore, assuming a dead time equal to $2\mu s$ (transmission time), the maximum data flow for each channel is $\approx$ 120 Mbyte/sec/channel (peak for short times). On the other hand, we expect an event every $200\mu s$ (mean value) so that the maximum continuous data flow is equal to 1.2 Mbyte/sec/channel which means $\approx$ 0.5 Gbyte/sec for the whole system. And, finally, if we assume that only $0.1 \div 0.2\%$ of all the pads is active at the same time, then the continuous data flow to be stored by the Storage System is equal $0.5 \div 1$ Mbyte/sec.

In synthesis the Event Builder and Storage System must satisfy the following specifications:
1) 400 independent digital input channels.
2) maximum peak input data flow for each channel: 120 Mbyte/sec.
3) maximum continuous input data flow for each channel: 1.2 Mbyte/sec.
4) maximum continuous data flow for storage on tapes: 1 Mbyte/sec.

3.6.2 Architecture

On the basis of the specifications given and taking into account the need of building a system which must be open and expandable as much as possible in order to foresee the future needs of the apparatus, probably the best solution is the modular one. In fact this solution makes it easy to upgrade the system and to change the obsolete components, without changing the architecture of the whole system. The best solution for this system is to use a VME-bus (IEEE 1014, 40 Mbyte/s band for 32 bit data) based system in which commercial or lab-made boards are housed. Therefore the Event Builder and Storage System can be made of dedicated VME crates controlled by a master CPU running the operating system LynxOS and linking this system to the network (Ethernet) for remote control (Fig.3.10). On this system it is also foreseen a GPS board for labeling the data with time.

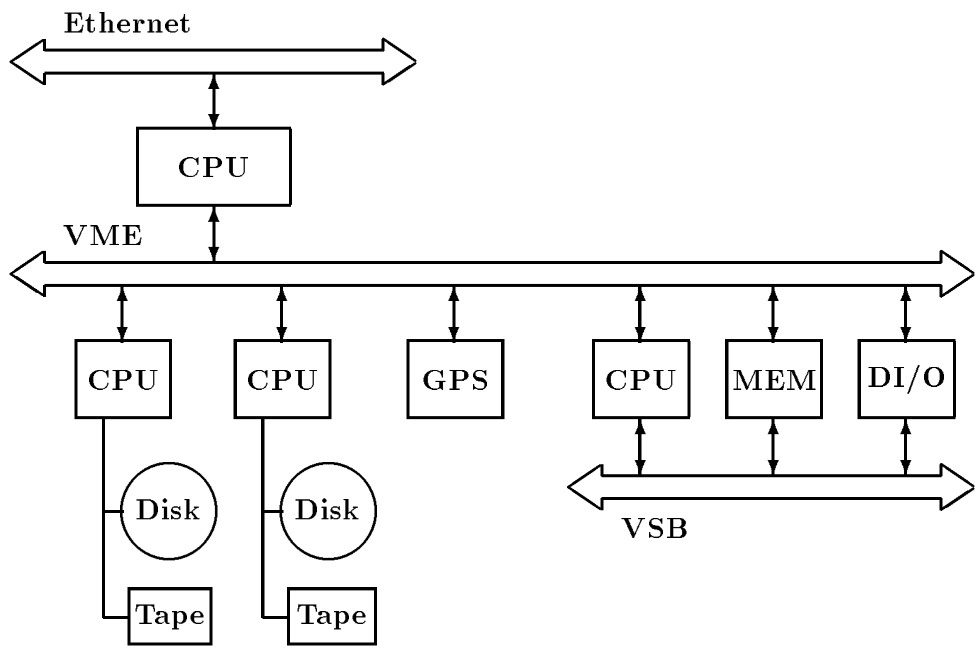

Figure 3.10. Event Builder and Storage System Hardware Structure

The two major specifications for the Event Builder and Storage System are the need of acquiring a maximum continuous input data flow of 1.2 Mbyte/sec/channel and the need of storing data on tapes with a maximum continuous data flow of 1 Mbyte/sec. The first specification can be satisfied using special memory boards or CPUs with a large amount of RAM memory aboard. The second specification is more difficult to be satisfied. In fact, such large amount of data (1 Mbyte/sec) have necessarily to be maintained off-line. Although an off-line archive can use both optical disks and magnetic tapes, actually the only economical affordable solution is that of using magnetic tapes. These devices have a storage capacity of the order of up to hundred Gbyte and their drivers can reach data transfer rates of the order of some Mbyte/sec. Actually, this transfer rate is not sufficient to satisfy the above mentioned specifications. A modular solution to this problem is given by the parallel staging of the data on disks (which can sustain a read/write data flow larger than 10 Mbyte/sec and can have a storage capacity of the order of ten Gbyte) and then copying them on tapes. This solution makes it easy also to reconfigure the system on the basis of the actual data flow.

The architecture of the Event Builder and Storage System is shown in fig.3.11. A user interface running on one of the control room workstations makes it possible to manage this system, to set its configuration, checking and changing its status, checking the errors, etc..

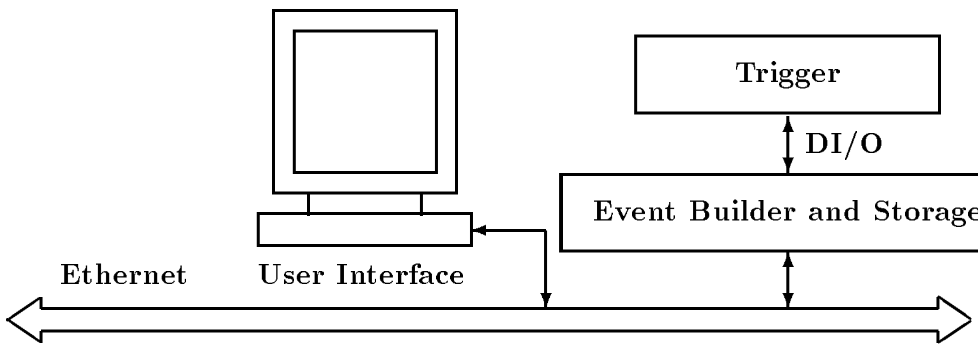

Figure 3.11. Architecture of the Event Builder and Storage System

3.7 THE RPC TEST ARRAY

A 30 m^2 RPC array is under test at the University of Roma 2. The array consists of 15 RPC modules of area $1x2m^2$ grouped in 5 lines or "corridors" of 1x6 m**2 as shown in the photograph of fig.3.12. The lay-out of each station is similar to that proposed for ARGO and already shown in fig . In this case however the photon converter was made with iron plates 15 mm thick, a solution previously proposed instead of the lead, and the size of the strips was 50×3.1 cm^2 so that 16 strips covered an area of 50×50 cm^2. This is intended to be a pilot experiment that except for the much smaller area and lower altitude reproduces the basic features of ARGO. We present here preliminary results concerning single corridors of the array as the electronics to handle all the signals of the 120 boards at the same time has been mounted very recently. A single corridor of 1×6 m^2 is subdivided in 12 regions of size 1×0.5 m^2 by using the OR of pairs of opposite boards. EAS are selected by a trigger condition requiring the coincidence of all the regions. TDCs are used to measure the arrival time of the signals of each region. The plot of the time delay vs position is given in fig.3.13 (a),(b) and (c) for three events. The best linear fit of the experimental points is also shown in fig.3.13. The slope of the strait line fitting the data gives the direction of the shower.

3.7.1 Temperature and Pressure Tests

The experiment ARGO requires to operate the RPCs in a mountain laboratory where the environment conditions, particularly those related to the temperature and the pressure, are different and more severe than in a normal laboratory. Specific tests concerning the response of RPCs in different conditions of temperature and pressure have been carried out on two chambers of area 2×2 m^2. Each chamber consists of two RPC modules 2×1 m^2 coupled along the 2 m side and red-out by 2 m long and 3 cm wide aluminium strips running parallel to the 2 m side. The systematic delay due to the propagation of the signal along the strip is 5 ns/m. At both ends the strips are terminated on 50Ω and connected to the front–end electronics

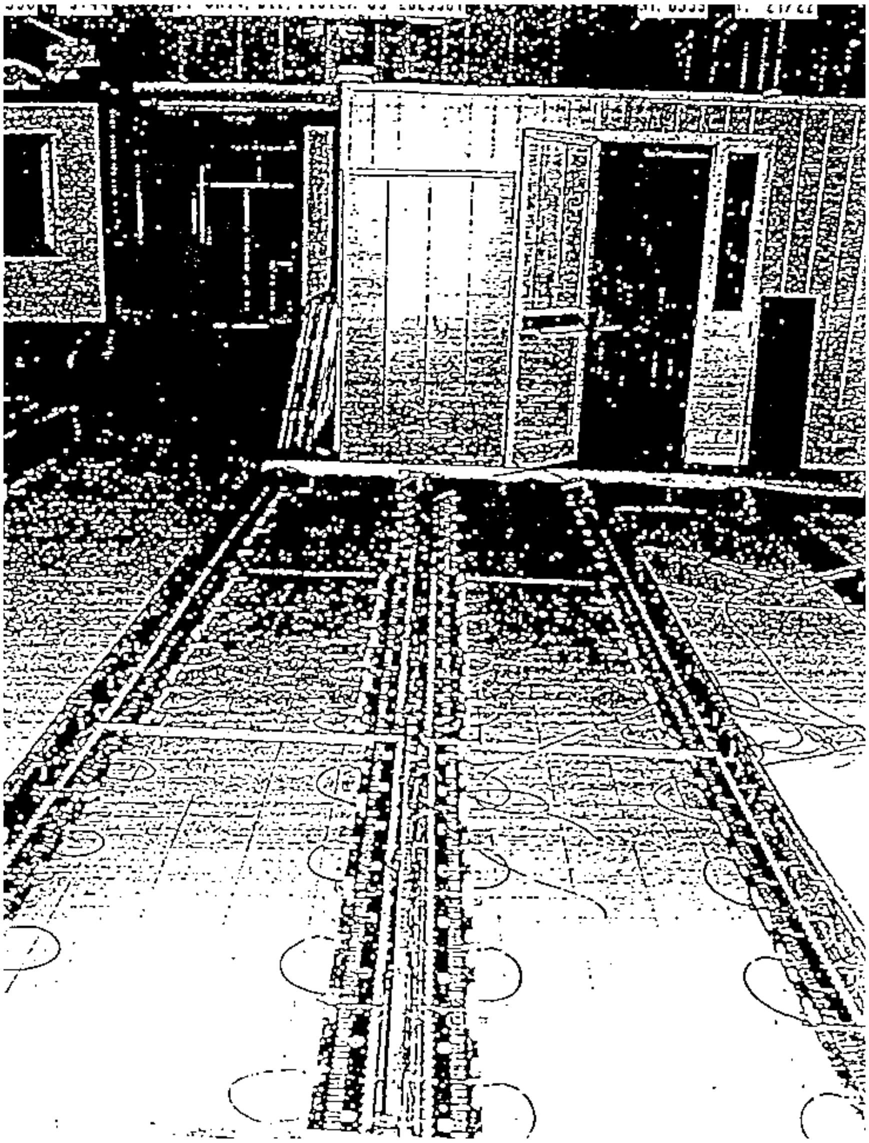

Figure 3.12: The test array built at the university of Roma 2

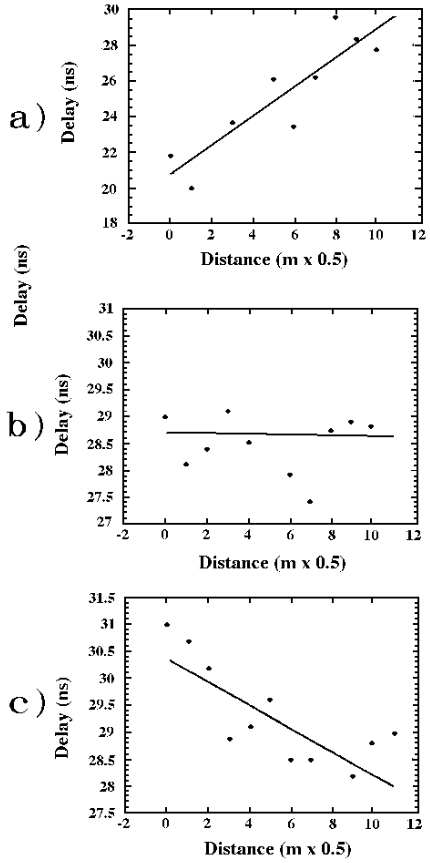

Figure 3.13: The plot of the time delay vs position (a),(b) and (c) for three events. The best linear fit of the experimental points is also shown.

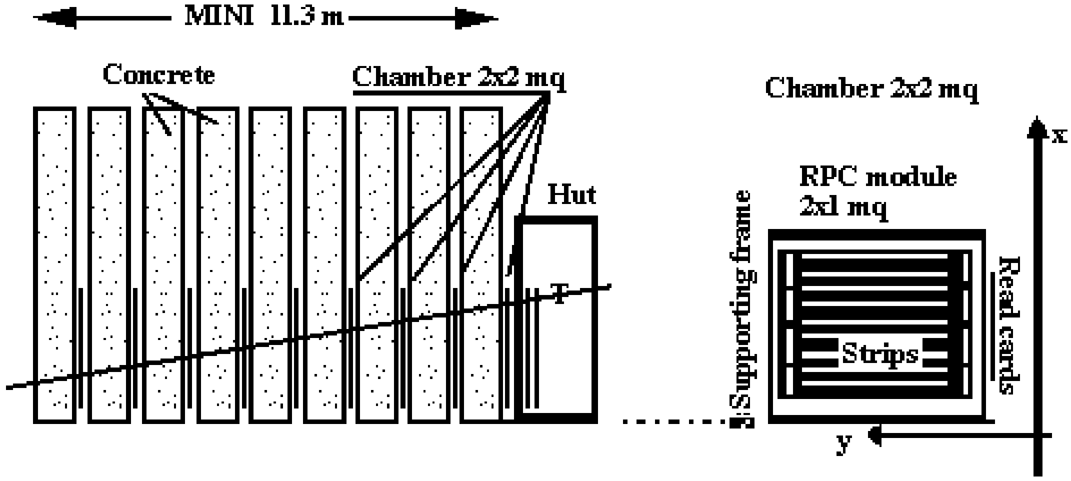

Figure 3.14: Sketch of the test chambers and the MINI telescope

which is mounted on boards situated at both sides of the module. Each board contains 16 front–end channels serially read out and a single FAST OR output which is optimized for time measurements, the input to output delay being the same for all the 16 ORed channels. The two test chambers were mounted vertically, 30 cm apart into a closed hut where the temperature could be controlled in the range $0 \div 30^oC$ with an accuracy of 1 ^oC. The hut was placed aside of the MINI [78] telescope as shown in fig. 3.14. The telescope, which is kept at room temperature, is equipped with fourteen chambers identical to those already described and also mounted vertically so as to select horizontal cosmic muons that can be used to test the performance of the chambers inside the hut. Fig. 3.15 shows the counting rate per unit surface of the test chambers vs the operating voltage for different temperatures. An exponential rise of the rate at high voltages is observed which is more evident at high temperature. This is mostly due to the noise produced by the spacers which are used to keep the plates parallel to one another. The detection efficiency vs operating voltage is shown in fig 3.16a for different temperatures. A plateau is reached at 95% efficiency. Most of the 5% inefficiency is due to the dead areas of the spacers and seals as well as to the uncovered area between the two RPC modules. Comparison among different curves in fig. 3.16a shows that the same efficiency is reached at higher voltage for a lower temperature. This is well explained as an effect of the temperature on the gas density: at lower temperature the density is higher and this is equivalent to a larger gas gap which requires a higher operating voltage. If this effect is accounted for by renormalizing the voltage scale with the factor T/T_o, where T is the actual temperature and $T_o = 293$ ^oK is the standard room temperature, all the points fit on the same curve as is shown in fig. 3.16b. Muons reconstructed in MINI as going in the direction from the test chambers towards the telescope, were used to measure the time of

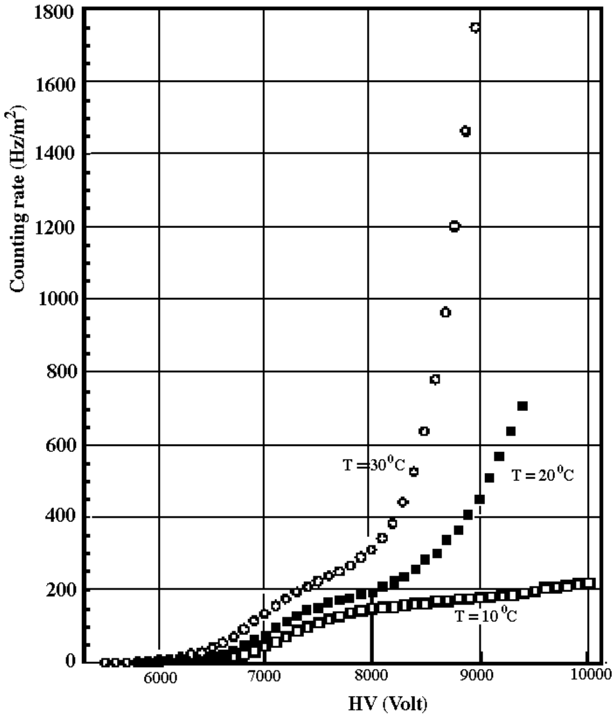

Figure 3.15: Counting rate per unit surface of the test chambers vs operating voltage for different temperatures

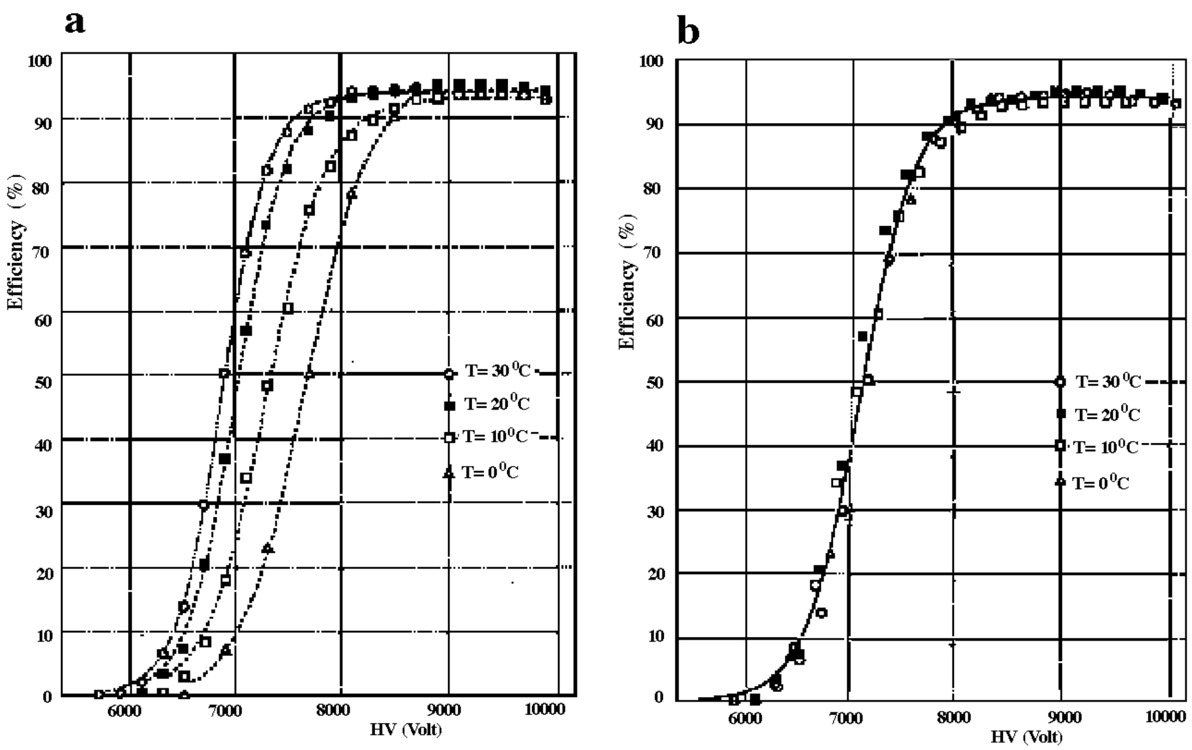

Figure 3.16: (a) - Detection efficiency vs operating voltage for different temperatures. (b)- Same as in (a) but with the voltage scale renormalized by the factor T/T_o where T is the actual temperature and $T_o = 293\ ^oK$.

flight between the test chambers. The mean time $(t_1 + t_2)/2$ between the arrival times of the signal at the opposite ends of the strip was used to correct for the systematic delay due to the propagation time of the signal along the strip. The time of flight distribution at 30 ^oC and 9100 Volt is shown in fig 3.17. It is characterized by a sharp peak of 2.0 ns FWHM and two non gaussian tails that have been demonstrated to be due to trajectories crossing one of the chambers near a spacer. The experimental conditions, with respect to previously published data [3], are different in the following points: higher operating voltage (1.6 kV inside the plateau instead of 1.0kV), higher front–end threshold (100 mV instead of 50 mV) and small differences in the construction procedure concerning the graphite layer which, in this case, was removed at the spacers position. Fig.3.18 shows the delay (a) and the time resolution (b) of the test chambers vs the operating voltage. Pressure tests are in progress. The detection efficiency vs operating voltage is shown in fig. 3.19(a) for two different pressures: 1000 and 500 mbar. The operating voltage scales with respect to the pressure in good agreement with the rule E/p=constant as is shown in fig. 3.19(b).

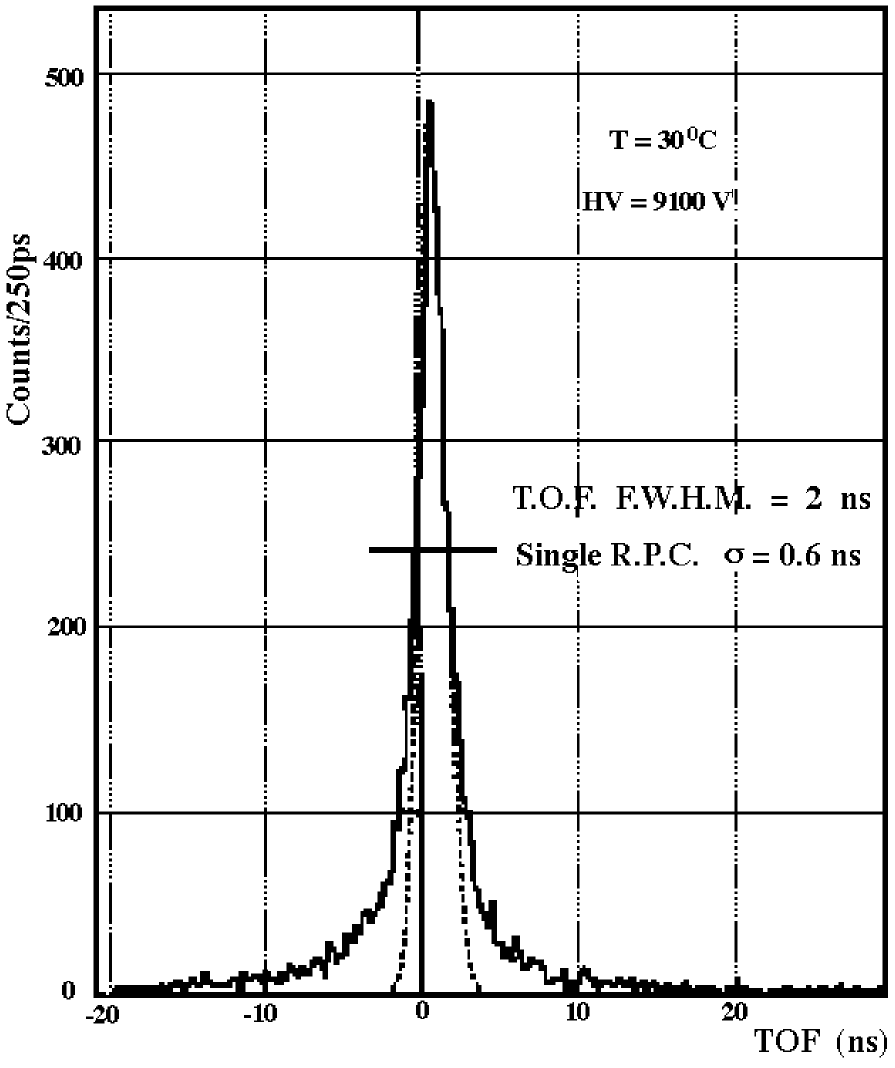

Figure 3.17: Time of flight distribution between the test chambers at 30 $°C$ and 9100 V

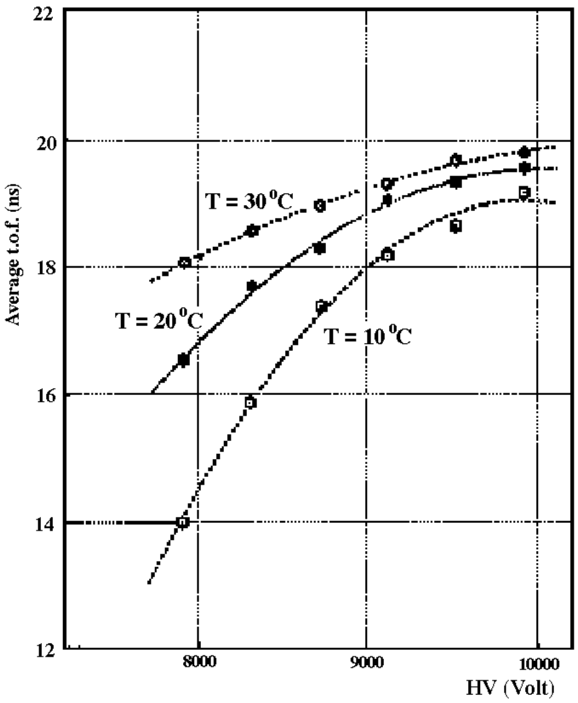

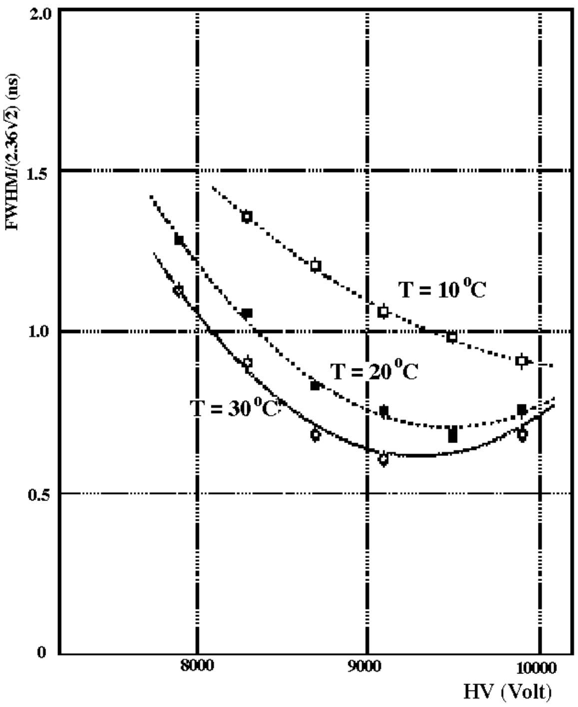

Figure 3.18: (a)- Time delay of the test chambers vs operating voltage for different temperatures. The delay is measured with respect to the MINI telescope kept at room temperature and fixed voltage (b)- Time resolution vs operating voltage for different temperatures

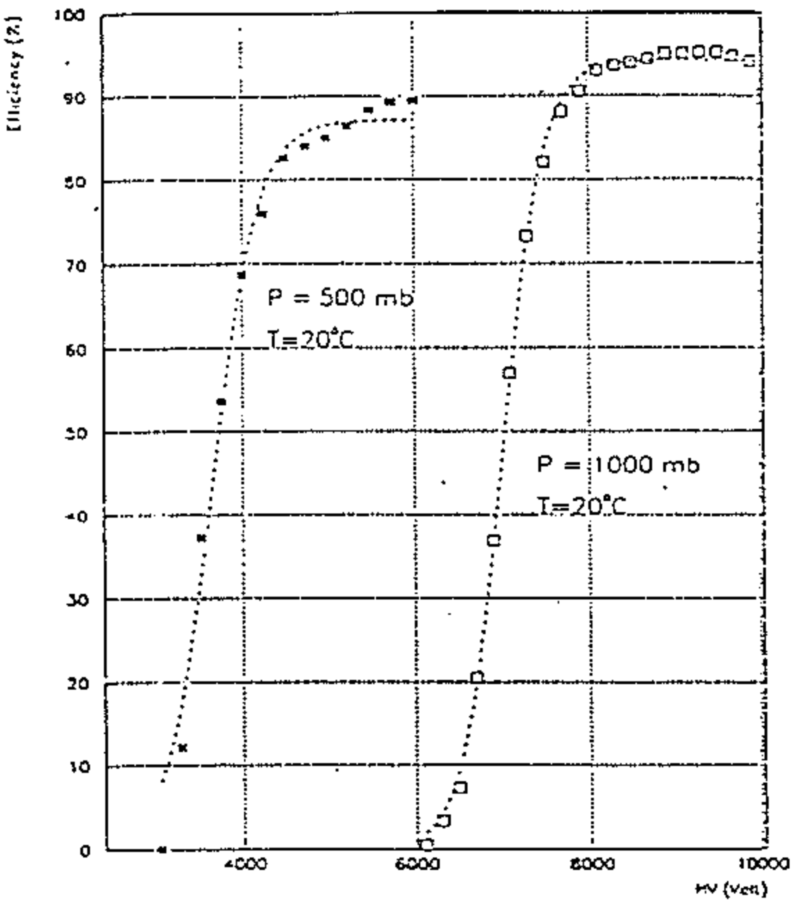

Figure 3.19: (a)- Detection efficiency vs operating voltage for two different pressures at 20 C (b)- Operating voltage for 50% efficiency vs pressure

Table 3.1: Daily variation of the temperature at Yanbajing site in two winter time days

Time (h)	Temperature (^oC) 3, Jan 1992	3, Feb. 1992
0:00	-4.3	-3.3
2:00	-7.9	-8.9
4:00	-10.5	-9.4
6:00	-10.1	-12.0
8:00	-8.1	-11.7
10:00	- 4.9	-5.0
12:00	5.2	3.0
14:00	8.8	6.2
16:00	9.4	10.0
18:00	9.1	7.8
20:00	3.9	2.5
22:00	-0.3	-2.6
24:00	-3.3	-7.4

3.8 THE SITE AND LOGISTIC.

The ARGO detector will be built at the Yanbajing cosmic ray laboratory 4300 $m.\ a.\ s.\ l.$ and $30^o\ N$ latitude. This site it is 90 Km far from Lhasa, connected with an asphalt road. Nearby from the laboratory site (about 2 Km) there is an electrical power plant and a small village. The $AS-\gamma$ air shower experiment performed by a Chinese-Japanese collaboration , is running in this laboratory since five years.

The weather conditions can be summarized in the following parameters:

- average temperature over 1 year : 2.5 ^oC;
- temperature excursion over many years : $-30^oC \div +25^oC$;
- average day– night temperature excursion : 16 ^oC
- maximum day– night temperature excursion over many years : 35 ^oC.

An example of the daily variation of the temperature is shown in the table 3.1

The water fall ranges in $249 \div 430 mm/year$, with an averaghe of 328 $mm/year$. Snowfall days are 26.4 per year on average, with a maximum snow depth of 7 cm. We note that these weather conditions are by far better than that existing in Campo Imperatore (the site hosting the EAS-TOP experiment) where, for istance, a snow depth of one meter or more is usual for several months.

We will present a detailed plan of the construction of the experimental hall in a separate document. The termal insulation of the hall is determined by the requirements of the detector. The results of the test previously discussed show that the apparatus requires that the temperature inside the hall must not exceed the interval between 8 ^{o}C and 30 ^{o}C with a thermal gradient inside the hall less than $10^{o}C$.

Bibliography

[1] C. Fichtel et al., ApJ. S.S. 94 (1994) 551.

[2] T. Haines, Proc. of 23th Intern. Cosmic Ray Conference, Calgary, 1993, 'Invited, Rapporteur and Highlight Papers', p.341 (World Scientific).

[3] M. Bailes and D. Kniffen, ApJ. 391 (1992) 659.

[4] D.J. Thompson et al., 'The second EGRET catalog of high-energy gamma-ray sources', NASA preprint.

[5] B. Dingus, presentation at Snowmass 1994, June 29 - July 14, Snowmass (Colorado).

[6] S. Hunter et al., ApJ. 436 (1994) 216.
S. Dingus et al., ApJ. 441 (1995) 270.

[7] J.W. Cronin Invited talk at the 24-th ICRC Roma 1995
to be published.

[8] M. Merck et al., Proc. of 24th Intern. Cosmic Ray Conference, Roma, 1995, vol.2 p. 195, and ref. therein.

[9] J. Daugherty and A. Harding, ApJ. 429 (1994) 325.
R. Romani and I. Yadigaroglu, ApJ. 438 (1995) 314.
K. Cheng, C. Ho and M. Ruderman, ApJ. 300 (1986) 500 and 522.

[10] P.Nolan et al., ApJ. 409 (1993) 697.

[11] see ref [7] and ref. reported therein.

[12] O. de Jager and A. Harding, ApJ. 396 (1992) 181.

[13] F. Aharonian, L. Drury and H. Volk, A. & A. 285 (1994) 645.

[14] T. Naito and F. Takahara, J. Phys. G 20 (1994) 477.

[15] R. Lessard et al., Proc. of 24th Intern. Cosmic Ray Conference, Roma, 1995, vol.2 p. 475.
A. Borione et al., ibid, p.439.
G. Allen et al., ApJ. 448 (1995), L25.

[16] T. Dame et al. Ap.J. 322 (1987) 706

[17] C. Bhat et al , J. Phys. G. 10 (1986) 1087.

[18] R. Enomoto et al., Phys. Rev. D46 (1992) 3239.
P. Reynolds et al. Proc. of 21 Intern. Cosmic Ray Conference, Adelaide 1990, Vol. 2 , p. 383.
C. Akerlof et al. Proc of 22th Intern. Cosmic Ray Conference, Dublin 1991, Vol. 1, p. 324.

[19] M. Aglietta et al., ApJ. 397 (1992) 148.
J. Matthews et al., ApJ. 375 (1991) 202.

[20] H. Bloemen, Proc. of 23th Intern. Cosmic Ray Conference, Calgary, 1993, 'Invited, Rapporteur and Highlight Papers', p.321 (World Scientific).

[21] see ref. [1] and C. von Montigny et al., ApJ. 440 (1995), 525.

[22] J. Chiang et al., ApJ. 452 (1995) 156.

[23] A. Kerrick et al., ApJ. 452 (1995) 588.

[24] L. Maraschi et al., ApJ. 435 (1994) L91.

[25] K. Mannheim and P. Biermann, A & A 53 (1992) L21.

[26] J.P. Rachen et al., A&A 273 (1993) 377.

[27] T. Stanev et al., Phys. Rev. Lett. 75 (1995) 3056.

[28] A. Salomon et al. Ap.J. 423(1994)L1.

[29] O. de Jager, Astrophys. and Space Science 230 (1995) 279.

[30] H. Murakami et al., ApJ. 428 (1994) 354.

[31] D. Hartmann, Astron. and Astrop. Rev. 6 (1995) 225.

[32] B. Dingus, Astrophys. and Space Science 230 (1995) 187 and references therein.

[33] see ref. [1] for an update summary.

[34] T. Piran, ApJ. 389 (1992) L45.

[35] C. Kochanek and T. Piran, ApJ. 417 (1993) L17.

[36] C. Dermer and T. Weiler, Astrophys. and Space Science 231 (1995) 377.

[37] F. Stecker and O. de Jager, ApJ. 415 (1993) L71.

[38] F. Stecker and A. Wolfendale, Nature 309 (1984) 37.

[39] M. Urban et al., Nucl. Phys. Supp. 14B (1990) 223.

[40] M. Amenomori et al., Phys. Rev. D47 (1993) 2675.

[41] M. Amenomori et al., Proc. of 24th Intern. Cosmic Ray Conference, Roma, 1995, Vol. 3, p.84.

[42] N. Kalneykov and G. Khristiansen J. Phys. G: 21 (1995) 1279.

[43] K. Asakimori et al. , Proc 23th Intern. Cosmic Ray Conference, Calgary 1993, Vol. 2, p.21.

[44] H. Yoshii et al., Proc. of 24th Intern. Cosmic Ray Conference, Roma, 1995, Vol. 2, p.703

[45] M.Amenomori et al. Proc. of 24th Intern. Cosmic Ray Conference, Roma 1995 , Vol 4, p. 840.

[46] K. Nagashima et al., Proc. of 23th Intern. Cosmic Ray Conference, Calgary, 1993 Vol 3 p. 711.

[47] L.I. Dorman, N. Iucci, G. Villoresi Astrophysics and Space Science, 208(1993)55-68.
J.G. Roederer EOS, Transactions, American Geophysical Union, 76(1995)

[48] J. W. Bieber, Proc. of the 24th ICRC, Roma, 1995
M.S. Potgieter, Proc. of the 23th ICRC, Calgary, Invited, Rapporteur and Highlight Papers, 1993, 213.

[49] Y. Munakata et al., Proc. of the 24th ICRC, Roma, 1995, 615

[50] S. Mori, Proc. of 24th Intern. Cosmic Ray Conference, Roma 1995, Invited and Rapporteur Papers.

[51] A.J. Owens and J. Jokipii, J. Geophys. Res., 77(1972)6639
A. J. Owens, J. Geophys. Res., 79(1974)895].

[52] S. Yasue et al.,24th ICRC, Roma, 1995, Vol. 4, p. 968

[53] D.F. Smart, Proc. of 24th Intern. Cosmic Ray Conference, Roma 1995, Invited and Rapporteur Papers.

[54] N. Mandzhavidze and R. Ramaty, Nucl. Phys. B, (Proc. Suppl.) 33A,B(1993)141.

[55] A.V. Belov et al. Proc. of 24th Intern. Cosmic Ray Conference, Roma 1995, Vol 4, p. 888.
L.Dorman et al. Proc. of 24th Intern. Cosmic Ray

[56] Thomson D.J., et al Nature Vol. 376(1995)139.

[57] R. Ladbury Physics Today, September 1995, p.17.

[58] M.Amenomori et al. Proc. of 24th Intern. Cosmic Ray Conference, Roma 1995 , Vol 4, p. 1148.

[59] B. D'Ettorre Piazzoli and G. Di Sciascio Astr. Phys 2(1994)199.

[60] G. Di Sciascio Ph.D. Thesis, University of Napoli (1993).

[61] R.Brun et al., "GEANT - detector description and simulation tool", CERN Program Library Vres. 3.21, W5013 (1993)

[62] M. Honda et al. Phys. Rev. D 52(1995)4985.

[63] S. Biller Astr. Phys. 3(1995)385

[64] M.Aglietta et al. Astr.& Space Science 231(1995)351.

[65] K. Hurley et al. Nature 372(1994)652.

[66] B. Dingus Astr.& Space Science 231(1995)187.

[67] J. Schneid et al. A.&A. 255(1992)L13.

[68] N. Sommer et al Ap.J. 422(1994)L63.

[69] D.Alexandreas et al. Phys. Rev. D43(1991)1735.

[70] A. Borione et al. Phys. Rev. D49(1994)1171.

[71] M.Aglietta et. al. Proc. 22-th Inter. Cosmic Ray Conf Dublin, 1991 Vol. p. 708.

[72] A. Karle et al. Proc. of the 22th Inter. Cosmic Ray Conf Dublin, 1991 Vol. 4, p. 460.

[73] M. Amonomori et al. Phys. Rev D47(1993)2675.

[74] N. Leikov et al. A.&A.SS97 (1993)345.

[75] G. Kanbach et al. A.&A.SS97 (1993)349.

[76] R. Santonico and R. Cardarelli, Nucl. Instr. and Meth. 187 (1991)377
R. Cardarelli et al., Nucl. Intr. and Meth. A263 (1988) 20

[77] R. Cardarelli, A. Di Ciaccio and R. Santonico, Nucl. Instr. and Meth. A 333 (1993) 399

[78] M. Abbrescia et al., Nucl. Instr. and Meth. A336 (1993) 322

[79] M. Bertino et al., Nucl. Instr. and Meth. A283(1989)654
C. Bacci et al., Nucl. Instr. and Meth. A324 (1993) 44
Gy. Bencze et al., Nucl. Instr. and Meth. A340 (1994) 466
T. Moers et al., Nucl. Instr. and Meth. A345 (1994) 474
M.Abbrescia et al. Nucl. Instr. and Meth. A359(1995)603
S.Natali "RPC performance al low pressure" RPC–95, Pavia.